CORROSION FATIGUE OF TUBULAR JOINTS IN SEAWATER FOR OFFSHORE MONOPOD STRUCTURES

DR. D.V. REDDY
DR. M. AROCKIASAMY
MR. S.S. GOWDA

Sponsored by:
Canada Centre for Mineral and Energy Technology
Department of Energy, Mines and Resources, Ottawa
Contract No. 20 SU. 23440-1-9090

Dr. O. Vosikovsky
Scientific Authority

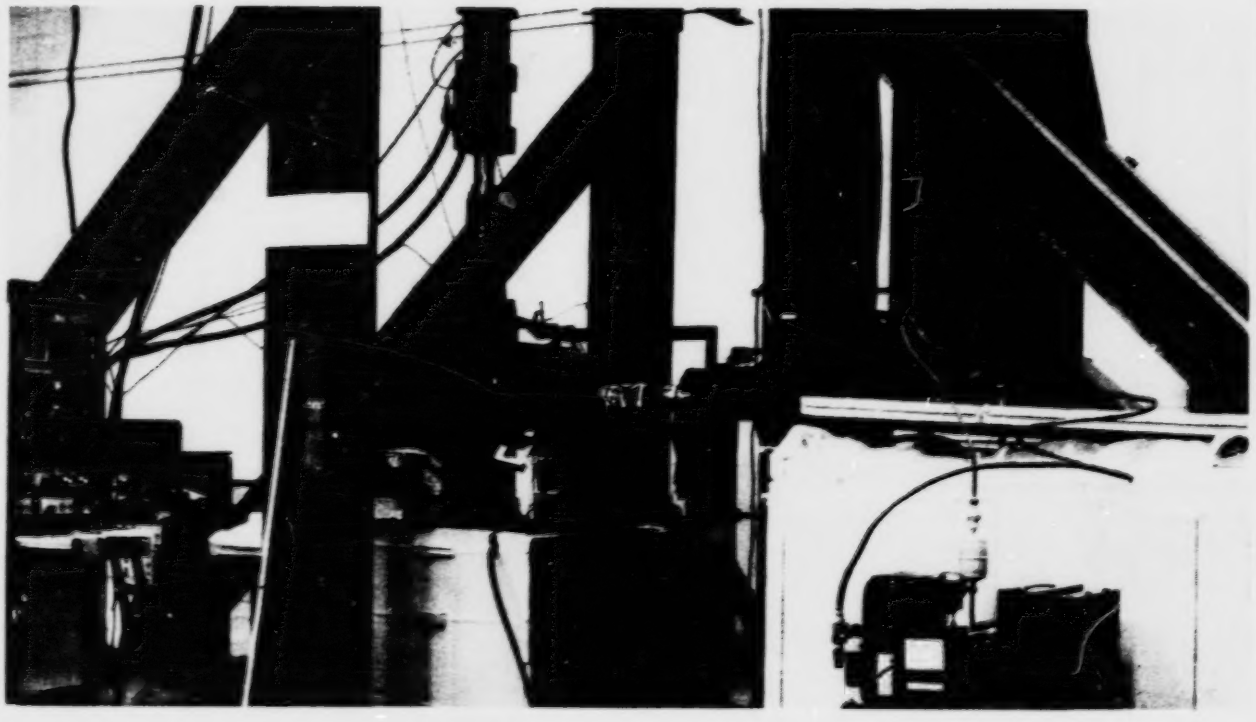

Faculty of Engineering and Applied Science
Memorial University of Newfoundland
St. John's, Newfoundland, Canada A1B 3X5
December, 1982

CORROSION FATIGUE OF TUBULAR JOINTS IN SEAWATER FOR OFFSHORE STRUCTURES

Final Report

by

Dr. D.V. Reddy
Dr. M. Arockiasamy
Mr. S.S. Gowda

Faculty of Engineering and Applied Science
Memorial University of Newfoundland
St. John's, Newfoundland, Canada A1B 3X5

Work on this project was conducted under the auspices of the Canada Centre for Mineral and Energy Technology, Energy, Mines and Resources, Canada

DSS FILE NUMBER	: 20 SU . 23440-1-9090
DSS CONTRACT SERIAL NUMBER	: OSU81 - 00412
CANMET PROJECT NUMBER	: 420604
CANMET SCIENTIFIC AUTHORITY:	Dr. O. Vosikovsky

DATE: December, 1982

This report should be cited as Contract Report No: OSU81-00412

136 pp

MICROMEDIA
AUG 19 1983

Disclaimer

All opinions expressed in this report are those of the authors and should not be considered to represent the position of CANMET or the Department of Energy, Mines and Resources.

SUMMARY

The report describes the experimental investigation of corrosion fatigue behaviour of monopod tubular joints in cold ocean environment. Measured strains under static loading at critical hot spots are compared with the finite element analysis. The fatigue lives for crack initiation, propagation and final failure of the joints are determined and compared with those of T- or Y- joints from the published literature. The effects of seawater, weld toe grinding and the nature of applied load viz. constant and variable amplitude loadings are discussed.

ACKNOWLEDGEMENTS

The financial support received from Canada Centre for Mineral and Energy Technology, Department of Energy, Mines and Resources, Ottawa is gratefully acknowledged. We would like to specially thank Dr. Gilmour and Dr. Vosikovsky for their helpful suggestions, discussions, purposeful coordination, constructive criticism and careful review of the draft. The authors thank Prof. G. Ross Peters, Dean, Faculty of Engineering and Applied Science, Memorial University of Newfoundland for the invaluable support and encouragement in the various phases of the project. The principal investigators (DVR and MA) are specially indebted to Mr. S.S. Gowda, Graduate Student for his untiring efforts and full cooperation throughout the course of this investigation.

Mr. D. Tilley, Mr. A. Bursey, Mr. C. Gries and Mr. C. Ward helped to set up the testing arrangement of the joints. Mr. J. Andrews, Welding Supervisor and his colleagues fabricated the specimens, seawater cooling tank and the test cell. The authors would like to gratefully acknowledge their assistance. We express our sincere appreciation to Mr. T. Duarte, Supervisor of Laboratories for his continued support throughout the project.

Special thanks are due to the Ocean Engineering Group for providing the support for Mr. S. Warren and Mr. L.S. Poh as work term students. Grateful acknowledgements are due to Professor H. Snyder, Director, Centre for Cold Ocean Resources and Engineering (C-CORE) for supporting two work term students, Mr. G. Yeo and Mr. I. McCloy, who assisted in this project. Assistance rendered by Mr. T.N.N. Murthy during night times when the experiments were in progress is gratefully

acknowledged. The finite element and nodal connectivity data for the NASTRAN computer code was prepared by Dr. K. Munaswamy assisted by Mr. S. Bhuyan. Mr. C. Noel and Dr. Egbert G. Verbrugge of the Canada Systems Group, Multiple Access Division, Toronto provided the computing facilities for the finite element analysis in the project. The authors wish to express appreciation for their assistance. Grateful acknowledgement is due to Mrs. M. Warren for the considerable care and patience in typing the manuscript.

TABLE OF CONTENTS

	Page
TITLE	i
DISCLAIMER	ii
SUMMARY	iii
ACKNOWLEDGEMENTS	iv
TABLE OF CONTENTS	vi
LIST OF TABLES	viii
LIST OF ILLUSTRATIONS	x
NOMENCLATURE	xiii
1. INTRODUCTION	1
1.1 Background	1
1.2 Scope	2
2. LITERATURE REVIEW AND ANALYTICAL PROCEDURE	3
2.1 Introduction	3
2.2 Hot Spot Strain or Stress Range	4
2.3 Parametric Equations	6
2.4 Fatigue Failure Criteria	7
2.5 Effects of Free Corrosion in Sea Water, Temperature and Weld Toe Grinding	7
3. FINITE ELEMENT ANALYSIS	10
3.1 QUAD4 Element	11
3.2 Mesh Generation	14
4. EXPERIMENTAL PROGRAMME	13
4.1 Design and Fabrication of Joints	13
4.2 Test Set-up and Instrumentation	14
4.3 Use of Automatic Data Acquisition System	16
4.4 Design and Installation of Cooling System for Circulating Seawater	19
4.5 Weld Surface Profiling	20
4.6 Measurement of Environmental Parameters	20

	Page
5. TESTING PROCEDURE	21
5.1 Static Tests	21
5.2 Fatigue Tests	21
6. RESULTS AND DISCUSSION	23
6.1 Stress and Strain Distributions	23
6.2 Hot Spot Stress and Strain Range	24
6.3 Fatigue Lives	26
6.4 Crack Initiation and Crack Growth Behaviour	27
6.4.1 Effect of Cold Seawater Environment	29
6.4.2 Effect of Weld Toe Grinding	30
6.5 Joint Stiffness Measurements	31
7. CONCLUSIONS	31
8. RECOMMENDATIONS FOR FURTHER RESEARCH	32
9. REFERENCES	33
Appendix-A: Measurement of Environmental Parameters	113
Appendix-B: Generation of Pseudo-Random Load History	117

LIST OF TABLES

Table No.	Title	Page No.
1.	Mechanical Properties of Steel	38
2.	Chemical Composition of Steel	38
3.	Joint Parameters (Dimensions in mm)	39
4.	Mechanical Properties of Electrodes	39
5.	Welding Details	39
6.	Range of Seawater Parameters	40
7.	Static Strain Readings for Corr. 1 Joint	41
8.	Static Strain Readings for Corr. 2 Joint	42
9.	Static Strain Readings for Corr. 3 Joint	43
10.	Static Strain Readings for Corr. 4 Joint	44
11.	Fatigue Test Results	45
12.a)	Hot Spot Strain Range and Strain Concentration Factor - Main Chord	46
12.b)	Hot Spot Strain Range and Strain Concentration Factor (SCF) - Branch Tube	47
13.	Hot Spot Stress Range and Stress Concentration Factor (SCF) - Main Chord	48
14.	Summary of Crack Growth Data: Corr. 1 Joint (Right of Centre Line)	49
15.	Summary of Crack Growth Data: Corr. 2 Joint (Right of Centre Line)	50
16.	Summary of Crack Growth Data: Corr. 3 Joint (Right of Centre Line)	51
17.	Summary of Crack Growth Data: Corr. 4 Joint (Right of Centre Line)	52
18.	Summary of Crack Growth Data: Dry 1 Joint (Right of Centre Line)	53
19.	Summary of Crack Growth Data: Corr. 1 Joint (Left of Centre Line)	54

		Page
20.	Summary of Crack Growth Data: Corr. 2 Joint (Left of Centre Line)	55
21.	Summary of Crack Growth Data: Corr. 3 Joint (Left of Centre Line)	56
22.	Summary of Crack Growth Data: Corr. 4 Joint (Left of Centre Line)	57
23.	Summary of Crack Growth Data: Dry 1 Joint (Left of Centre Line)	58
24.	Comparison of Fatigue Test Results	59

LIST OF ILLUSTRATIONS

Figure No.	Title	Page No.
1.	Jacket-Type Steel Structure	60
2.	Cook Inlet Monopod Platform	61
3.	Tripod Tower Platform	62
4.	Major Platform Loads and Corrosion Zones	63
5.	Diagrammatic Representation Defining Idealized Hot Spot Stress	64
6.	Quadrilateral Element - QUAD4	65
7.	Force and Moment Resultants	66
8.a)	Mesh Generation	67
b)	Finite Element Mesh with First Branch Tube	68
9.	Monopod Tubular Joint	69
10.	Tube Weld Connection Elevation	70
11.	Welding Details	71
12.	Plan of Test Assembly	72
13.	Test Assembly for Fatigue Loading	73
14.	Connection Unit for Vertical Loading	74
15.	Connection Unit for Horizontal Loading	75
16.	Brittle Coating Cracks Around Joint Intersection	76
17.	Strain Gauge Locations for Joint - Corr. 1	77
18.	Strain Gauge Locations for Joint - Corr. 2	78
19.	Strain Gauge Locations for Joint - Corr. 3	79
20.	Strain Gauge Locations for Joint - Corr. 4	80
21.	Cross-Sectional View of Protective Coatings for Strain Gauge Installations in Water	81
22.	Automatic Data Acquisition System	82

Figure No.	Title	Page No.
23.	Block Diagram of Data Acquisition System	83
24.	Schematic Illustration of Seawater Cooling and Circulation Systems	84
25.	Test Set-up with Cooling Unit	85
26.	Weld Toe Grinding Profile	86
27.	Comparison of Strain Distributions: Joint-Corr. 1	87
28.	Comparison of Strain Distributions: Joint-Corr. 2	88
29.	Comparison of Strain Distributions: Joint-Corr. 3	89
30.	Comparison of Strain Distributions: Joint-Corr. 4	90
31.	Strain Distribution near Weld Toe: Joint-Corr. 1	91
32.	Strain Distribution near Weld Toe: Joint-Corr. 2	92
33.	Strain Distribution near Weld Toe: Joint-Corr. 3	93
34.	Strain Distribution near Weld Toe: Joint-Corr. 4	94
35.	Surface Crack Growth Development: Joint-Corr. 1	95
36.	Surface Crack Growth Development: Joint-Corr. 2	96
37.	Surface Crack Growth Development: Joint-Corr. 3	97
38.	Surface Crack Growth Development: Joint-Corr. 4	98
39.	Surface Crack Growth Development: Joint-Dry 1	99
40.	Crack Growth Characteristics of Joints	100
41.	Crack Growth Rate	101
42.a)	Photograph of Joint-Corr. 1 (Harmonic Load)	102
42.b)	Photograph of Joint-Corr. 2 (Pseudo-Random Load)	103
42.c)	Photograph of Joint-Corr. 3 (Harmonic Load)	104
42.d)	Photograph of Joint-Corr. 4 (Harmonic Load)	105
43.	Photograph of Joint-Dry 1 (Pseudo-Random Load)	106

Figure No.	Title	Page No.
44.	Specimen Tip Displacement: Joint-Corr. 1	107
45.	Specimen Tip Displacement: Joint-Corr. 2	108
46.	Specimen Tip Displacement: Joint-Corr. 3	109
47.	Specimen Tip Displacement: Joint-Corr. 4	110
48.	Comparison of Fatigue Test Results	111
49.	Basic S-N Curves for Tubular Joints	112
Fig. B-1	LYREC TAPE RECORDER	120
Fig. B-2	PSEUDO-RANDOM INPUT LOAD-TIME HISTORY (JOINT-CORR.2)	121
Fig. B-3	POWER SPECTRAL DENSITY OF PSEUDO-RANDOM LOAD SIGNAL	122

NOMENCLATURE

D	Mean diameter of chord
d	Mean diameter of brace
E	Young's modulus of elasticity
L	Length of chord
K	Constant
N_i	Number od cycles
R	Radius of chord
r	Radius of brace
T	Wall thickness of chord
t	Wall thickness of brace
u_x, u_y, u_z	Displacements in x,y and z directions
ε_{TR}	Measured strain range perpendicular to and adjacent to weld toe at the worst hot spot
ε_o	Nominal strain in the brace
ε_{HS}	Hot spot strain
σ_o	Nominal stress in the brace
σ_{HS}	Hot-spot stress
SCF	Stress concentration factor
SCNF	Strain concentration factor
$\varepsilon"_{HS}$	Extrapolated strain parallel to weld toe
ν	Poisson's ratio

$$\alpha = \frac{2 \times \text{Length of chord}}{\text{Mean dia. of chord}} = \frac{2L}{D}$$

$$\beta = \frac{\text{Mean radius of brace}}{\text{Mean radius of chord}} = \frac{r}{R}$$

$$\gamma = \frac{\text{Mean radius of chord}}{\text{Wall thickness of chord}} = \frac{R}{T}$$

$$\tau = \frac{\text{Wall thickness of brace}}{\text{Wall thickness of chord}} = \frac{t}{T}$$

1. INTRODUCTION

1.1 Background

Research on fatigue of welded tubular joints has been accelerated by the petroleum industry due to the increasing use of tubular structural elements in the design and fabrication of both onshore and offshore exploration and production platforms. Steel tubes of circular cross section are efficient in resisting axial compression and torsion, and have better hydrodynamic characteristics than those of other shapes [1,2]. The first template-type steel structure, installed in the Gulf of Mexico at a water depth of 7 m, became the forerunner of the welded tubular offshore platform. Fig. 1 illustrates the exploration and production platform structure of the jacket-type supporting a platform deck. Monopod gravity platforms offer alternative concepts for shallow ice-infested waters such as the Beaufort sea. The monopod platform installed in Cook Inlet, Alaska in 30 m deep water, is supported by four branch members, Fig. 2 [3]. Recently Heerema Engineering Company proposed a monopod structure supported by three branch members (Fig. 3), with the platform weight in the range of 25-30,000 tonnes [4]. The monopod structures offer minimum exposed frontal areas to wave and ice actions [5].

Offshore structures are subjected to large gravity loads and environmental forces besides corrosion. Fig. 4 shows the summary of major dead loads, environmental forces and corrosion zones, at different depths in a typical offshore structure. API R2A - Recommended Practice for Planning, Designing and Constructing Fixed Offshore Platforms [6], outlines the design principles and procedures for offshore structure design.

Analytical and experimental investigations of monopod tubular joints subjected to both static and fatigue loads are scarce in the literature, compared to planar joints such as K, T, X and Y joints, on which extensive research has been carried out by several investigators [7,8,9,10,11].

1.2 Scope

The present investigation describes the analytical and experimental studies on corrosion fatigue of monopod tubular joints. The main objectives of the program were:

(i) Measurement of strains under static and fatigue loading at critical hot spots and comparison with the finite element analysis

(ii) Determination of the fatigue lives for crack initiation, propagation and final failure of the joints,

(iii) Study of corrosion effect on the joint fatigue lives in cold water environment,

(iv) Study of the effect of weld toe grinding on fatigue life,

(v) Determination of fatigue crack growth behaviour of the joints under constant amplitude and pseudo-random loading.

The experimental work consisted of testing four joints under simulated cold ocean environments. The natural sea water temperature was maintained around 0°C to simulate the Arctic environment, and salinity and dissolved oxygen contents monitored and measured every day during testing. Three joints were tested under constant amplitude loading at a frequency of 0.20 Hz and one joint under pseudo-random loading. Two joints were tested in as-welded and two with weld toe

ground conditions and the behaviour studied under both static and alternating loads. The crack initiation, propagation and final failure were recorded in wet conditions and compared with those of a companion specimen tested in air, and the relevant published data.

2. LITERATURE REVIEW AND ANALYTICAL PROCEDURE

2.1 Introduction

The present fatigue design of tubular joints is based on tests in air, although it is known, that sea water environment has a detrimental effect on fatigue behaviour. Recently some tests have been conducted in seawater under the sponsorship of European Coal and Steel Community (ECSC) and United Kingdom Offshore Steels Research Project (UKOSRP).

Accurate estimation of peak stresses in tubular joints is necessary for predicting the fatigue life and crack tolerance. When a tubular joint is loaded, the stress distribution includes i) the basic structural response to the applied loads (nominal stresses), ii) geometrical stresses maintaining compatibility between the tubes, and iii) 'notch' stresses resulting from the highly localised deformations in part of the tube wall near to the chord-brace intersection. Nominal stresses arise due to the tubes behaving as beam-columns, whereas geometric stresses result from the differences in deformation between the chord and brace. The differential deformations require the tube walls to bend so that the chord and brace maintain continuity at the weld; they also cause an uneven distribution of the nominal membrane stresses round the brace circumference. 'Notch' stresses arise because of the geometric discontinuity of the tube walls at the weld toes and

do not extend far through the wall thickness. Sharper corner at the weld toe and greater angle of the overall weld profile to the tube wall cause higher 'notch' stress.

Four possible approaches to the stress analysis are based on: i) Local stress analysis, ii) Parametric equations, iii) Finite element analysis, iv) Steel or acrylic models. In this investigation the stress concentrations have been determined using parametric equations and finite element analysis. The fatigue failure criterion used in the experimental work is discussed in section 2.4.

2.2 Hot Spot Strain or Stress Range

The service life of tubular joints is generally calculated from S-N curve, where S is the hot spot stress range [12,13]. According to AWS Structural Welding Code [14], the hot-spot stress or strain range is defined as: "Total range of worst hot-spot stress or strain on the outside surface of intersecting members of the toe of the weld joining them - measured after shakedown in model or prototype connection or calculated with best available theory". The British Code [15], uses the following definition for the hot-spot strain range: "Relationship Q (curve) applies to the main members of T, Y and K connections. The stress range corresponds to the peak range on the outer surface adjacent to the toe of the attachment weld between brace and chord members". The corresponding S-N curves for the above two definitions are AWS-X curve and DD55-Q curve respectively.

In the new fatigue design rules (16), the idealized hot spot-stress is defined by linear extrapolation to the weld toe of the principal stresses.

To obtain the hot spot strain range from extrapolation of the strain gauge measurements to the weld toe, the specimens were instrumented with strain gauges at appropriate locations as defined by the following equations (Fig. 5):

$$a_1 = 0.2 \sqrt{rt} \text{ but } < 4 \text{ mm} \quad (1)$$

$$a_2 = 0.4 \sqrt[4]{(rt)\ (RT)} \quad (2)$$

$$b_1 = 0.2 \sqrt{rt} \text{ but } < 4 \text{ mm} \quad (3)$$

$$b_2 = 0.65 \sqrt{rt} \quad (4)$$

The maximum hot spot strain range is obtained using the linear extrapolation to the weld toe through A and B, thus including the effects of the global geometry of the joint and the weld (17). The magnitude of the hot spot strain range, $\Delta\varepsilon$ for the random loading is given by an equivalent constant amplitude equal to the root mean square value (rms) of

$$\Delta\varepsilon = \frac{2\sigma}{0.707} \quad (5)$$

where σ = rms value of a random signal. In the American literature (18) the hot spot stress, σ_{HS} is defined as

$$\sigma_{HS} = E \cdot \varepsilon_{HS} \quad (6)$$

The strain concentration factor (SNCF) is the ratio of the hot spot strain, ε_{HS} and the nominal strain, ε_o in the brace. The stress concentration factor (SCF) adopted in Europe is the ratio of maximum principal (hot spot) stress, σ_{HS} and the nominal stress σ_o in the brace (19). Thus,

$$SCF = \sigma_{HS}/\sigma_o \quad (7)$$

in which

$$\sigma_{HS} = \frac{E}{1-\nu^2}(\varepsilon_{HS} + \nu\varepsilon''_{HS}) \tag{8}$$

$$SNCF = \varepsilon_{HS}/\varepsilon_o \tag{9}$$

Eqn. (7) can be rewritten as

$$SCF = \frac{1}{(1-\nu^2)} \frac{\{\varepsilon_{HS}+\nu\varepsilon_{HS}''\}}{\varepsilon_o}$$

$$= \frac{\varepsilon_{HS}}{\varepsilon_o} \frac{1}{(1-\nu^2)} \{1+\nu \frac{\varepsilon_{HS}''}{\varepsilon_{HS}}\} \tag{10}$$

With $\nu = 0.3$ and $\frac{\varepsilon''_{HS}}{\varepsilon_{HS}}$ being small, the SCF > 1.1 SNCF.

2.3 Parametric Equations

The semi-empirical parametric formulae for estimating the geometrical stress concentration factor (SCF) at the weld toe have the following general form (20,21):

$$SCF = K\, \alpha^{n_1}\, \beta^{n_2}\, \gamma^{n_3}\, \tau^{n_4}\, (\sin\theta)^{n_5} \tag{11}$$

where

K = constant

n_i = exponents

It has been reported that Kuang's equations give unsatisfactory results when applied to X joints, although Smedley's T joint equation could cover X joints (22). In the present study, Toprac and Beale's and Visser's equations were found to yield reasonable estimates of SCF. Toprac and Beale's (40) approximation for the SCF is given by

$$SCF = 0.1873\ \alpha^{0.56}\ \beta^{-0.022}\ \gamma^{0.746}\ \tau^{0.608} \qquad (12)$$

and Visser's (41) empirical equation by

$$SCF = \frac{t}{T}\left(10 + 0.15\ \frac{D}{T}\right) \sin^2\theta\ \left(1.4 - 0.75\ \frac{d}{D}\right) \qquad (13)$$

The parametric equations are valid for the following ranges:

$6.67 < \alpha(= \frac{2L}{D}) < 40.0$

$0.3 < \beta(= \frac{d}{D}) < 0.8$

$8.33 < \gamma(= \frac{D}{2T}) < 33.33$

$0.2 < \tau(= \frac{t}{T}) < 0.8$

$0° < \theta < 90°$

2.4 Fatigue Failure Criteria

The four stages of the joint fatigue life are the following:

i) N_1: 15% drop in the strain gauge measurement close to the point of crack initiation

ii) N_2: First discernible surface cracking usually detected by visual inspection

iii) N_3: First through thickness cracking

iv) N_4: End of test, when the crack length becomes approximately equal to half the main chord circumference

2.5 Effects of Free Corrosion in Sea Water, Temperature and Weld Toe Grinding

Dijkstra and de Back (17) have presented the fatigue test results on forty tubular T- and X- joints, which have been carried out in the Netherlands. Most joints were tested in air in axial loading. Four

T-joints were tested in artificial sea water, three at free corrosion and one with cathodic protection. During the fatigue test, crack growth was monitored by visual inspection and strain measurements. The sea water tests had only 43% of the life that could be expected in air. The free corrosion and air fatigue tests showed relatively early crack initiation and slow crack growth compared to the cathodically protected joint. Hicks (24) described the UKOSRP fatigue programme designed to acquire information on the fatigue life of welded joints in seawater for compiling design rules for offshore structures. The influence of a simulated seawater environment has been shown to be much less marked than would be expected and differences in stress history show small effects on performance. The characterisation of the stress histories on the basis of root mean square or higher order averaging offers a valuable method of comparing constant amplitude and variable amplitude test results.

Gibstein (25) presented the results obtained from fatigue tests carried out at Det Norske Veritas in the framework of the European Fatigue Research Programme. It was found that both the depth and length of cracks in tubular joints, are approximately linear functions of the number of cycles. Walker (26) has reported the Dutch results, which indicated that the fatigue endurance of T shaped joints in seawater at 20°C is equal to about 1/2 to 1/3 that of a similar test joint in air under constant amplitude loading conditions. On the contrary, the tests performed in Britain at stress ratios of R=0 and R=-1 for joints freely corroding in seawater at 5°C showed that the fatigue strength was not significantly different from that obtained in

air. Based on the measured strain drop in the hot spot, it was inferred that the fatigue crack growth rate in seawater was approximatley three times that obtained in air. The rate of fatigue crack propagation in seawater in typical offshore steels at high stress ratios was considerably greater than that observed from tests in air. The accelerated fatigue crack growth rate, however, occurred over a relatively narrow range of cyclic stress intensities (27). Schutz (28) presented general conclusions from the data accumulated within the frame of the ECSC offshore steels program. The effect of seawater corrosion on fatigue life is not significant (a factor of less than two on life) under realistic stress sequences and tests at constant amplitudes overestimate the effect (a factor of 2.5 on life). Further work has been suggested for i) prediction of crack propagation life of tubular joints in seawater and ii) study of effect of long exposure times to seawater on fatigue life under realistic stress amplitudes. Tests on steels by Vosikovsky [29], over a frequency range of 0.01 and 10 Hz, under cathodic and free corrosion potential in aqueous environments, indicated that they were not susceptible to stress corrosion cracking in the environment used (3.5 percent NaCl solution).

Haagensen (30) presented a survey of research on fatigue strength improvement of welded cruciform and T-joits carried out within ECSC and Norway and compared the results with existing weld design codes. It has been shown that consistently high fatigue strengths in air were obtained for welds treated by grinding. Under free corrosion in sea water the increase in fatigue strength due to weld profile improvement

was less than in air. Mullen and Merwin (31) reported tests on full penetration built welded T-joints and concluded that fatigue life improvement associated with toe grinding was significantly affected with greater beneficial effect at lower load levels. Increasing the toe radius improved the fatigue life by about 10 percent, even when the weld angle was kept constant. Further research has been recommended to quantify the magnitude and interaction of the effects of local geometry parameters such as weld angle, leg length, toe radius and plate thickness on crack propagation near the weld toe surface. Morgan (32) compared a fully ground profile with a 45° as welded profile for T butt welds in 38, 75 and 100 mm thick material. On the basis of experimental evidence, an increase of 30 percent on strength or 2.2 on life was recommended for toe ground welds (33). Zwaans, Jonkers and Overbeeke (34) performed fatigue tests on welded T-shaped plate specimens under random loading in air at a temperature of 17-26°C and sea water as an environment at 20 ± 1°C. It was found that seawater reduced the endurance by a factor of 2.2, which compared well with the German random tests (factor ≈ 2). However, the lower reduction factor of 1.5 obtained from the British random tests was due to the lower temperature used (5°C versus 20°C).

3. FINITE ELEMENT ANALYSIS

The proposed structure is analysed by the MSC/NASTRAN computer code (35) using a flat shell element (QUAD 4). Because of the nonaxisymmetric nature of the problem (structure being rotationally symmetric with the wave load antisymmetric), the nodal and element data

were prepared for the three-dimensional structure and used to evaluate the stress distribution and structure deformation. The following section describes the basic theory related to the analysis using QUAD4 finite element.

3.1 QUAD4 Element

The triangular and quadrilateral flat shell elements used are shown in Fig. 6. The element formulation allows inplane, bending, and transverse shear deformations as well as coupling between inplane and bending behaviour. The grid point numbers associated with the fields G1, G2, G3, and G4 are unique for either element and must be ordered consecutively around the perimeter of the QUAD4 element such that all interior angles are less than 180 degrees. The element has five nodal degrees of freedom consisting of two inplane displacements, (u_x, u_y) and a normal displacement (u_z), and two bending rotations (θ_x, θ_y). No rotational degree of freedom is permitted about the normal for these elements so that there will be a row and a column of zeros in the six by six stiffness matrix associated with each connected grid point. The system stiffness matrix will thus be singular and constraint is imposed by the single point constraint (SPC) capability of NASTRAN computer code.

The constitutive matrix, which defines the stress-strain law for the shell element is as follows:

$$\begin{Bmatrix} \{N\} \\ \{M\} \\ \{Q\} \end{Bmatrix} = \begin{Bmatrix} tG_1 & t^2G_4 & 0 & e^\circ - e_1^\circ \\ t^2G_4 & IG_2 & 0 & \kappa^\circ - \kappa_1^\circ \\ 0 & 0 & t_sG_3 & \gamma^\circ \end{Bmatrix} \tag{14}$$

where the matrices $\{M\}$ and $\{N\}$ are given as

$$\{M\} = \begin{Bmatrix} M_x \\ M_y \\ M_{xy} \end{Bmatrix} = - \int_{-t/2}^{t/2} z \{\sigma\} \, dz \tag{15}$$

$$\{N\} = \begin{Bmatrix} N_x \\ N_y \\ N_{xy} \end{Bmatrix} = - \int_{-t/2}^{t/2} \{\sigma\} \, dz \tag{16}$$

where t = thickness of the element and $\{\sigma\} = \begin{Bmatrix} \sigma_{xx} \\ \sigma_{xx} \\ \sigma_{xy} \end{Bmatrix}$

The terms e° are defined as surface strains and given as

$$\left\{ e^\circ \right\} = \begin{Bmatrix} e^\circ_{xx} \\ e^\circ_{yy} \\ e^\circ_{xy} \end{Bmatrix} = \begin{Bmatrix} \partial u_x / \partial x \\ \partial u_y / \partial y \\ \dfrac{\partial u_x}{\partial y} + \dfrac{\partial u_y}{\partial x} \end{Bmatrix} \tag{17}$$

where u_x and u_y are the displacements of the natural surface in x and y directions. Similarly the reference surface curvatures are

$$\left\{ \kappa^\circ \right\} = \begin{Bmatrix} K^\circ_{xx} \\ K^\circ_{yy} \\ K^\circ_{xy} \end{Bmatrix} = \begin{Bmatrix} \dfrac{\partial^2 u_z}{\partial x^2} \\ \dfrac{\partial^2 u_z}{\partial_y{}^2} \\ 2 \dfrac{\partial^2 u_z}{\partial x \partial y} \end{Bmatrix} \tag{18}$$

where u_z = the displacement in the z direction.

$e_1{}^\circ$ and κ° are the initial strain and curvature and $\{Q\}$ and $\{\gamma^\circ\}$ are defined as

$$\{Q\} = \begin{Bmatrix} Q_x \\ Q_y \end{Bmatrix} \tag{19}$$

$$\{\gamma^\circ\} = \begin{Bmatrix} \gamma_{xy}{}^\circ \\ \gamma_{yz}{}^\circ \end{Bmatrix} \tag{20}$$

Q_x and Q_y are the transverse shear forces in Fig. 7 and $\gamma_{xy}{}^\circ$ and $\gamma_{yz}{}^\circ$ are the corresponding transverse shear strains of the reference surface. The cross sectional properties of t, I and t_s are the membrane thickness, second area moment for the cross section and shear thickness respectively, referred to the reference surface.

The matrices G1, G2, G3 and G4 are elastic constants which are obtained from the continuum formulation. The term containing t^2G_4 in the Eqn. 14 represents the effect of coupling of bending and membrane behaviour.

The stresses are computed at distances z_1 and z_2 from the reference plane along a line perpendicular at the centroid of the element.

The stress state is given as:

$$\begin{Bmatrix} \sigma^1 \end{Bmatrix} = -\frac{z_1}{I}\{M\} + \sigma^\circ + \begin{Bmatrix} \Delta\sigma \end{Bmatrix} \tag{21}$$

where the membrane stress σ° is given by

$$\sigma^\circ = G_1 (e^\circ - e_1{}^\circ) + t\, G_4 (\kappa^\circ - \kappa_1{}^\circ) \tag{22}$$

and $\Delta\sigma$ results from thermal effects. In addition to these stresses, the force resultants are also computed at the node points.

The restraint provided by welds at the ends of the tubes with the base plate is simulated by restraining the translations and rotations of all

the bottom nodes. The solution of the equilibrium equations yields the displacement components of the nodal points of the finite element system.

3.2 Mesh Generation

The developments of the intersections of the three branches with the chord were drawn and the elements marked in the developments. Both triangular and quadrilateral elements were used, with smaller size elements along lines of intersection and larger size elements in the remaining parts of the joint. A smooth transition from smaller to larger elements was used and the bulk of the input consisted of the specification of i) surface coordinates of the points in the developments and ii) elements by three/four nodal points. The generated mesh for the joint is shown in Fig. 8.

Maximum hot spot strains and stresses, SNCFs and SCFs obtained from the finite element analysis are compared with the measured values for both main chord and branch members (Tables 12 and 13).

4 EXPERIMENTAL PROGRAMME

4.1 Design and Fabrication of Joints

The materials selected for the fabrication of specimens for the wet and dry tests were respectively ASTM A36 Grade B steel which was locally available, and ASTM A53 Grade B, donated by Stelco (Steel Company of Canada). The mechanical properties of the steels are given in Table 1, chemical compositions in Table 2 and joint parameters in Table 3.

All the three branch tubes, spaced at 120° to each other, intersect the main chord at one third of its height, with an inclination of 37° with the vertical axis (Fig. 9). To avoid stress concentrations due to proximity, the axial and lateral loadings were applied at distances of more than three times the diameter of the main tube from the joint intersection. The ends of all the branch tubes and the main chord were welded to a base plate 25 mm thick, which was bolted to the heavy duty test floor 760mm thick. All welds were of the fillet type, with electrodes AWS-ASTM E6011 and E7018 specifications to achieve full penetration. The weld sizes between intersecting branch tubes and main chord selected according to design requirements, are shown in Figs. 10 and 11. In addition to normal visual inspection, all welds were subjected to 100% radiographic examination using gamma rays, to ensure that no cracks or major weld defects existed. Faulty weld locations, indicated by radiography, were removed, rewelded and re-examined to avoid possible flaws. The mechanical properties of electrodes and welding details are shown in Tables 4 and 5.

4.2 Test Set-up and Instrumentation

For loading purposes, a reaction frame (Figs. 12 and 13) was suitably adapted for both vertical and horizontal loading conditions, with hydraulic actuators of 222 kN and 667 kN capacities respectively. Special connections were provided for static vertical (Fig. 14), and cyclic horizontal (Fig. 15) loadings. The horizontal loading to the main chord was applied with a 'wrap-around' semi-circular plate assembly to distribute circumferentially the load on the stiffening sleeve in both compression and tension. The semi-circular plates were

connected to the horizontal ram through end plates (Fig. 15). Great care was taken to achieve the verticality of the 'dead weight simulating' hydraulic ram to reduce the load eccentricity to the minimum.

For proper instrumentation of strain gauges to measure strains at critical 'hot spot' locations under static and fatigue loadings, brittle lacquer stress coating was applied to the joint covering a length of about 1 1/2 times the main tube diameter in the chord and a distance equal to the branch tube diameter in the brace. The choice of the coating was based on the temperature and humidity in the laboratory. A Tens-Lac brittle lacquer undercoat, U-10, consisting of a mixture of aluminum powder and a carrier solvent, was first sprayed on to the surface of the joint to obtain uniform reflectivity. Brittle lacquer was then applied over the undercoat at intervals of 2 min. between each coating, except the last one, which was applied after 20 min. The coating was cured at about 75°F for 24 hours, and brought down to the testing temperature of 65°F. A vertical step-wise static loading was first applied and no cracks were found. After releasing the vertical load, a step-wise horizontal load was applied and cracks in the coating marked on the surface at incremental loading levels. The spread of the lacquer cracks around the joint gave a picture of the overall strain distribution and the severity of the strains at critical locations. These observations were used to establish the gauge locations. The coating crack distribution is shown in Fig. 16.

Each specimen was instrumented with electrical resistance strain gauges at critical locations. The gauge length of the uniaxial and

rosette gauges was 3.18 mm and their corresponding overall lengths were 6.35 mm and 6.99 mm. The strain gauge locations for the four specimens tested in seawater are shown in Figs. 17 through 20. Since many gauges were immersed in seawater, special protective coatings were applied on the gauges to protect them against chemical attack and moisture due to seawater and condensation around the joint. After the gauge was installed in position, M-coat G was applied to the terminal of the gauges where they are soldered to the lead wires. A thin coating of M-coat A/D was applied to the full width of the gauge and to all the exterior edges. After allowing to dry for about 24 hours at room temperature, an intermediate layer of metal foil such as M-coat FA or PTFE Teflon film was applied to produce a further vapour barrier. A final layer of M-coat G was applied after an elapse of a few hours (36). Fig. 21 shows the cross sectional view of protective coatings for strain gauge applications. This procedure was adopted for all the joints tested in seawater.

4.3 Use of Automatic Data Acquisition System (Fig. 22)

An automatic data acquisition system was employed for strain measurements using the following Hewlett-Packard units: 9825A Controller, 9862A Plotter, 3455A Digital Voltmeter, 3437A System Voltmeter and 3495A Scanner. The units were connected via a Hewlett-Packard Interface Bus (HP-IB), which provides a link and communication between the components. All the strain gauges from the specimen were connected to BLH strain gauge switch and balancing units which in turn were interconnected to a B & K strain indicator unit. The change in the resistance of any strain gauge caused by the load could be read

from the digital indicator display or through its proportional remote analog output. The B & K strain indicator type 1526 gives instantaneous direct readings of strain levels on a digital display and had a hold function to permit the measurement of largest peak, regardless of sign and time. In cases where both static and dynamic strains are present the two components can be separated by the use of the hold function. The built-in set of low pass filters can also help to achieve this besides noise filtering. Because of the demodulator principle used in the strain indicator, resistive and capacitive unbalance on a strain gauge arrangement can be balanced out together by one potentiometer [37].

All the strain gauges were connected in half-bridge configuration. To eliminate the temperature effects, compensating gauges were used along with the active strain gauges. The BLH switch and balancing units were modified internally by connecting a high and low wire from one of the input channels to the high and low output wires respectively, to facilitate automatic strain measurements and simultaneous data recording. This enables the scanner to pick up individual channels at the computer's command.

The strain gauges from the test specimen were connected to the strain indicator unit via the scanner and balancing units. An excitation voltage was applied across the simulated Wheatstone bridge and the variation in voltage drop recorded. The strain data was displayed in the indicator unit, while the analog signal was transmitted to the A/D converter i.e. the system voltmeter, where the signal was converted from analog to digital binary code and extended

into the computer message storage. Similarly, the digital voltmeter interfaced with the computer received the load signal from the load cell of the hydraulic actuator. The computer was used to record simultaneously both the load and strain signals. The computer was programmed to collect data, store the maximum and minimum strain at any stage of testing, plot the stress-strain hysteresis loops for different gauges and record the data on paper. This automatic strain measuring system helped to measure strains more efficiently and accurately during testing. The computer controlled data acquisition system is shown in Fig. 22, and the block diagram in Fig. 23.

4.4 Design and Installation of Cooling System for Circulating Seawater

Two special tanks, one for cooling the water (dimensions: 1200 mm x 1200 mm x 1200 mm), and the other to house the test specimen (dimensions: 900 mm x 1050 mm x 1050 mm), were fabricated in the laboratory for carrying out tests in a simulated natural seawater environment. Natural seawater from the Atlantic Ocean was transported and cooled in the main tank and then circulated through the test cell containing the specimen. Two pumps, with a flow capacity of 11 litres/min., were used - one to pump the water to the test cell and the other to circulate the water from the test cell back to the main tank. The water returning to the main tank was discharged with a free fall to maintain the oxygen concentration. In addition a small aeration pump was used to pump air into the water. A cooling unit was provided in the main tank with an automatic control system, and the water temperature was maintained between +1°C and -2°C. The seawater temperature around the specimen was maintained at 0°C throughout the

testing period. The schematic view of the seawater circulation system with cooling arrangements is shown in Fig. 24. The sides and bottom of the sea water cooling tank were covered with a thick plastic sheet to minimize corrosion. However, the specimens and the inside surface of the test cell were free to corrode. The test set-up with test cell housing the specimen, and the main tank with cooling system are shown in Fig. 25.

4.5 Weld Surface Profiling [16,30]

Fatigue strength of welded tubular joints can be increased by improving the weld profiles. The most promising technique is grinding of weld toes (30). Grinding removes weld imperfections, slag inclusions, crack-like defects, and reduces stress concentration. In the present investigation, the weld toe grinding was carried out using a disc grinder. Care was taken to produce a smooth concave profile at the weld toe. To achieve the maximum advantage, the grinding depth was approximately 1 mm, and it was extended little beyond the weld toe so as to remove the undercuts as can be seen in Section A, Fig. 26. Section B (Fig. 26) shows the profiling of the weld done on the joint tested in air.

4.6 Measurement of Environmental Parameters

Offshore structures installed in hostile environments are subjected to both corrosion and fatigue. The combined effect of an aggressive environment and fluctuating stress accelerates the fatigue damage. The corrosion fatigue life can be affected by environmental factors, such as dissolved oxygen content, salinity, temperature, velocity of the surrounding fluid and pH value [27,38,39]. In the

present investigation, salinity, pH value, dissolved oxygen content, HCO_3^- concentration and temperature were measured once a day and the values shown in Table 6. The detailed measurement procedures are given in Appendix A.

5. TESTING PROCEDURE

5.1 Static Tests

The joints were instrumented with electrical resistance strain gauges. A shakedown of the instrumentation was performed by applying a partial load 4 to 5 cycles before the commencement of the test, to ensure satisfactory performance of the gauges and eliminate the drift. Strains were recorded when the joints were subjected to step-wise increasing and decreasing loads. The selected load levels and the recorded strains are given in Tables 7-10.

5.2 Fatigue Tests

Three monopod tubular joints were tested at a frequency of 0.20 Hz under constant amplitude loading and one joint under pseudo-random loading, all at stress ratio, R = -1. The method of generation and application of time history of the random load signal are described in Appendix B. The number of cycles were counted as positive zero crossings. During fatigue loading, strains from all the strain gauges were recorded at appropriate intervals for all the four specimens. A linear variable displacement transducer (LVDT) was installed at the free end of the chord above the level of the horizontal hydraulic actuator (Fig. 25). Use of LVDT gave better accuracy in the displacement measurements of the joints than those determined from the actuator stroke measurement.

Crack growth due to fatigue can be monitored by visual inspection, surface markings, measurement of the drop in strain level and non-destructive techniques (NDT). In the present investigation, an attempt was made to detect the crack initiation and propagation using non-destructive testing methods. Krautkramer Ultrasonic Miniature Flaw Detector USK 5MR and Miniature Chart Recorder SR5 and a portable Magnetic Particle Testing unit were used to detect the cracks at the weld toes. The water level around the specimens was first lowered well below the joint intersection level and the locations near the expected crack initiation regions were cleaned and dried. The portion was then magnetized with individual contact prod sets. Immediately after magnetizing, magnaflux liquid was applied and the cracks were observed with a Magnaglo black light. The magnetic particles in suspension adhered to the crack openings, if any, and reflected thereby indicating the presence of the crack.

Ultrasonic and magnetic particle methods were not successful in crack detection and as a result the reported surface crack lengths were measured visually using magnifying glass. The water level surrounding the test specimen was lowered for observing the crack initiation. The first crack initiation was noticed at the crack lengths ranging from 2 mm - 10 mm. However, the detection of through-thickness-cracking of the chord was very successful. This was made feasible by the use of kerosene filled inside the chord to a predetermined height of 75 mm. As soon as the through-cracking occurred, the kerosene oozed out during the crack opening in each cycle. This was immediately noticed not only by the smell but also by its floatation on the water surface. A fresh

batch of natural sea water was then added within a time period of 2500 to 3000 cycles to replace the water polluted by kerosene. This procedure was followed for all four specimens. The crack growth measurements after wall penetration might have been affected due to the traces of kerosene. Total crack length was measured considering the main crack in the chord together with the secondary cracks branching off from the main crack along the weld toe.

The joints, Corr.1 and Corr.4 were tested in as-welded condition, while the other two, Corr.2 and Corr.3 in weld toe ground condition. The number of cycles corresponding to 15% strain drop in the hot spot region, first crack initiation, through-thickness cracking and end of test were recorded and the results presented in Table 11.

6. RESULTS AND DISCUSSION

6.1 Stress and Strain Distributions

The stress analysis was carried out by finite element method and the results along the symmetry line with respect to bending loads are compared with the measured strains (Figs. 27 to 30). Generally the computed values compare reasonably well with the measurements, with the difference of only 10 to 15 percent. Neglecting the sixth degree of freedom in the thin shell element did not introduce any significant errors even when the bending effects are predominant. The maximum computed stresses occur at the midsurface intersection of the chord and brace. A more realistic estimate of the stress distribution can be determined if the weld dimensions are taken into account in the modelling. The difference between the numerical and experimental data

would be decreased by considering the influence of the size of the weld. In the vicinity of the weld and chord intersection, the secondary bending effects could be minimized by choosing the dimensions of the elements to be equal to one to two times the characteristic length, $\ell_c = \sqrt{TR}$, where T and R are the chord thickness and radius respectively (42,43). Due to the time constraints, this aspect has not been considered in the present investigation.

6.2 Hot Spot Stress and Strain Range

The hot spot stress and SCF are computed using i) finite element method, ii) parametric equations (Eqns. 12 and 13) and equations suggested by iii) Marshall (18) (Eqn. 6) and iv) Radenkovic (19). The extrapolation method from the strain measurements to the weld toe as suggested by the European Working Group III and Department of Energy, U.K. (16) gives the hot spot strain range, which is consistent with the finite element method (Table 12, and Figs. 27 to 30). For the joints with diameter ratio, $\beta = 0.428$ and wall thickness ratio, $\tau = 0.688$, this method can be applied easily and the average SNCF at the hot spot is 8.65 for the four joints compared with 9.70 as obtained by the finite element method. For the brace the average maximum measured SNCF was 4.54 compared with 6.58 determined by FEM (Table 12(b)). Table 13, shows the comparison of stress concentration factors as obtained from the experiment and finite element method. The variation in the results can be explained as due to i) absence of weld toe in the finite element discretization of the intersecting region and ii) limitations involved in obtaining consistent experimental data from the actual location with

respect to the weld toe. The experimental uncertainty is compounded by the size and type of strain gauge used. Although the use of three gauge rosette ensures the measurement of the principal strains, the physical size of the rosette causes difficulties in obtaining measurements near the actual weld toe. A relatively smaller uniaxial gauge will allow for the placement of the gauge closer to the weld toe, which requires a priori knowledge of the stress state to determine the maximum principal stress. The SCF computed by using Marshall's approach is lower than those determined by other methods, since it neglects the biaxiality of strains and the measured strain range (without extrapolation to the weld toe). On the other hand SCF computations by Radenkovic's approach (19) which considers the biaxial strain field and takes into account the extrapolated strains, yield higher values than Marshall's. Figs. 31 though 34, show the distribution of strains near weld toe of main chord from which the extrapolated strains were obtained.

Although the finite element method constitutes a viable technique for predicting the hot spot stress in tubular joints, the parametric equations provide an alternate approach to estimate the relative magnitude of the hot spot stress with respect to the nominal branch stress. The thickness to diameter ratio of the chord and branch to chord diameter ratio are the parameters, which govern the stress distribution. The branch to chord thickness ratio influences only the relative bending stiffness of the branch and chord and hence governs the bending stress in the branch at the intersection. Although the

parametric equations were developed for planar T-, Y-, and K-joints (20), the applicability to the spatial type joint is examined in the present study. The stress concentration factors (Table 13) based on relationships proposed by i) Beale and Toprac (40) and ii) Visser (41) are low compared to those obtained by other methods although the parameters of the joints tested are within the range of applicability. Beale and Toprac's equation retains the chord length as a significant parameter while Visser's relationship has been developed mainly for modelling T- and K- joints. The original data, which form the basis of the parametric equations, were obtained from models, which did not simulate the presence of the weld or its influence on hot spot stress and this can cause under estimation of the SCF.

6.3 Fatigue Lives

The corrosion fatigue test results are given in Table 11 and Figs. 48. The extrapolated hot spot strain range is plotted against the number of cycles at the end of the test. The lives corresponding to the crack initiation and wall penetration are also shown in Fig. 48. The resulting S-N diagram shows consistency with the AWS-XX and DD-55 curves with very little scatter. The measured hot spot stress ranges (defined by Radenkovic's SCF from Table 13) are plotted in the S-N diagram, (Fig. 49) using N_3, cycles to wall penetration as this is the preferred failure criteria used in the new British Rules (16). The experimental results are compared with i) deisgn T-curves for chord wall thicknesses of T<22 mm in air and sea water (unprotected), ii) basic T-curve application for T = 22 - 32mm and iii) experimental data from model tubular joints on which the design curves are based

(T = 16,22 and 32 mm). All the measured lives are longer than the design lives defined by the T-curve for T<22 mm in sea water. With the exception of joint Corr. 3, tested at a rather high stress range, the measured lives exceed the design lives for joint in air, or cathodically protected in sea water.

The data presented in Refs. 10, 33, 44 and 45 showed a clear trend to reduced endurance as the thickness increases at the same hot spot stress range. However there is no obvious thickness effect in the Japanese results. The present results fall just below the lower bound of the scatter (Fig. 49). The mean life of 6 mm (D-168 mm) thick joints was shown roughly three times longer than that of 16 mm thick joints by de Back (Ref. 44). The measured lives of monopod joints are thus seen to be shorter than those of T or Y joints of comparable dimensions. Table 11 shows the number of cycles corresponding to 15 percent strain drop, first visible crack, crack through chord wall and end of test and the ratio of fatigue lives. Surface cracks were as long as 50 percent of the circumference of the joints at the time of termination of the tests. Table 24 presents the comparison of results from available literature for the 'dry' and 'wet' tests. The selection of joints in Table 24 is based on comparable chord and brace dimensions and the hot spot stress levels close to those used in the present study. The variable amplitude test results, plotted on an rms basis (Eqn. 5) fit well in the S-N plot of the constant amplitude tests (Fig. 48).

6.4 Crack Initiation and Crack Growth Behaviour

The fatigue failure of the joints is a continuous process, which originate from micro scale defects, which cannot be detected in their

early stage by ordinary nondestructive methods. The early indication of the development of the cracks is obtained from the observed drop in the strain output from the rosette gauge located at the critical hot spot (as close as 6 mm to the weld toe). The crack initiation life, N_1 is based on the laboratory observation of the reduction in the initial full output strain amplitude by 15 per cent. The first visible crack corresponding to N_2, ranges from 2.5 mm to 10.00 mm (Table 11). The photographs of crack in joints Corr. 1, Corr. 2, Corr. 3, and Corr. 4 are shown in Figs. 42(a) to 42(d).

The crack propagation rates on the surface as well as in through thickness directions are quite different from the crack propagation behaviour associated with failures in other structures in which the propagation rates accelerate exponentially as the crack grows; the crack growth stage constitutes only a small part of the overall fatigue life. Although the tubular joints exhibit early crack initiation in view of the high SCF, it is compensated by the slow rate of propagation and the propagation stage constitutes the major span in the fatigue life (Table 11). The cracks always initiate at the weld toe in the hot spot region on the chord side close to the symmetry line in the plane of bending. The cracks then propagate along the weld toe for about 30° from the symmetry line and then branch away from the weld toe into the chord wall. Figs. 35 through 39 and Tables 14 through 23, show the characteristic results from the measurements of crack propagation on the chord side. The crack length and growth rate for one side of symmetry line for all the joints are shown in Figs. 40 and 41. Half crack length vs N/N_4 indicates a linear relation until the occurrence

of through thickness cracking. The crack growth rates on both sides of symmetry line at different stages of joint life vary from 1.05 to 158.82 x 10^{-4} mm per cycle depending on the magnitude of load range levels and the average crack growth rates for the joints Corr. 1, Corr. 2, Corr. 3, Corr. 4 and Dry 1 are 18.46, 5.81, 217.27, 24.71 and 4.39 x 10^{-4} mm/cycle respectively. Increased crack growth rates are caused by higher hot spot stress ranges. The crack initiation points in the joints were observed to be either left or right of the symmetry line in the first branch tube; while the main cracks started to grow into the chord surface, secondary cracks continued along the weld toe for a distance ranging from 10 to 25 mm.

6.4.1 Effect of Cold Sea Water Environment

The fatigue strength under free corrosion has been studied by several investigators (26,33,46,47). The Netherlands and Norwegian research programs have concluded that the free corrosion fatigue strength at water temperatures of 20°C and 12°C is significantly lower than that in air. But the tests carried out in U.K. have found that sea water at 5°C has no significant effect on fatigue strength, since the corrosion effect at the lower temperature should be less than that for tests at higher water temperatures. Sea water tests have been reported (23) which had a lifetime of only 43 percent of that expected in air. In the present study, the crack length of Joint Corr. 2 specimen, which was tested under variable amplitude loading in sea water at 0°C is compared with that of the companion specimen Dry 1 under identical loading. For the same fatigue life, the total crack lengths including the main and secondary cracks for the Joint Corr. 2

and Dry 1 are found to be 552 and 417 mm, respectively and the corresponding crack growth rates estimated as, 5.81×10^{-4} and 4.39×10^{-4} mm per cycle. The failure pattern for the two joints are shown in Figs. 42(b) and 43. The Dutch program concluded that fatigue crack growth rate in sea water is three times faster than that in air.

6.4.2 Effect of Weld Toe Grinding

The fatigue cracks tend to originate at the sharp defects left at the toe due to welding. Haagensen (30) and Mullen and Merwin (31), reviewed the advantages and limitations of several methods for improving the fatigue strength of welded joints. Weld toe grinding details of Dry. 1 and Corr. 2 joints are shown in Fig. 26. Toe radius in Corr. 2 joint (Section A, Fig. 26) is much larger than that of Dry. 1 (Section B, Fig. 26). The onset of crack initiation occurred at 6.1×10^5 cycles and 2.38×10^5 cycles for Corr. 2 and Dry. 1 joints respectively. Possible increase in the toe radius, weld defect removal and surface finish have delayed considerably the crack initiation event. The instantaneous crack growth rates for the two joints are approximately the same after the crack initiation. Similar findings have been reported for welded plate specimens and tubular joints (31,33,47). The stress ranges for the as welded joints Corr. 1 and Corr. 4 are different from those of toe ground specimens Corr. 2 and Corr. 3 and hence meaningful comparison of the effect of toe grinding cannot be made. However, it could be seen that in the present study, the toe grinding has a detrimental effect on fatigue life in sea water (Fig. 49). The thinning of the wall could have compensated for any benefits from the reduced stress concentration and the removal of weld toe defects.

6.5 Joint Stiffness Measurements

The specimen tip displacements vs. number of cycles for the four joints are shown in Figs. 44 through 47. Little change in the stiffness was observed until crack initiation. During the crack propagation in the main chord, a continuous increase in displacement was observed, along with a gradual increased variation in deflection when the crack fronts diverged from the weld toe into the main chord on either side of symmetry line. When the crack length was approximately equal to about 50 percent of the main tube circumference, the displacement remained almost constant until the termination of the test. Monitoring the stiffness change during the service life becomes very significant in assessing the structural integrity of offshore structures. The specimens deflected more during opening of the crack resulting from the reduced stiffness.

7. CONCLUSIONS

Based on the limited number of tests carried out on monopod tubular joints under constant amplitude and pseudo-random loadings in natural seawater the following conclusions can be drawn:

1) The fatigue crack initiation occurred in the joints (as welded and toe ground) on either side of symmetry line but not necessarily at the highest critical hot-spot location. (Figs. 35 to 39); this could be due to the presence of possible weld defects and slag inclusions.

2) Although a meaningful comparison of the effect of toe grinding cannot be made, it can be stated that weld toe grinding appears to have no beneficial effect on fatigue life in sea water (Fig. 49).

3) Based on the tests on Corr. 2 and Dry 1 joints, the instantaneous crack growth rates are approximately the same after crack initiation; but the overall crack growth rate is higher in the natural cold sea water than in air for the same fatigue life.
4) The crack initiation phase consumes major part of the joint lives. The number of cycles at which the visible crack initiation occurred ranges from 38.2 to 64.2 percent of the joint lives.
5) The measured lives of the spatial monopod joints are shorter than those of T or Y joints of comparable dimensions.
6) The joints resist the loads without significant displacement, even when the crack length becomes equal to half the circumference of the main chord; further crack propagation does not take place in the main chord, since the branch members opposite to the horizontal hydraulic actuator resist the applied cyclic loads.

8. RECOMMENDATIONS FOR FURTHER RESEARCH

Based on the tests carried out on monopod tubular joints in cold seawater environment at free corrosion potential, under constant amplitude and pseudo-random loading, the following recommendations are made:

1) More tests on similar joints with cathodic protection at normal potential, in the range of -800 mv to -1100 mv need be carried out to study the effect on fatigue life.
2) The main chord, branch tubes, base plate and the inside surface of the test-cell are affected by corrosion due to cold seawater which occurs after few days of wetting; the circulating sea water

polluted with these impurities may adversely affect the corrosion rate in the remainder of the testing. It is suggested that these areas be coated with an appropriate paint prior to the test except the region where the crack initiation and propagation are expected to occur. This precautionary measure will aid to establish a completely controlled corrosion test for better understanding of the corrosion effect in cold water. However this may introduce cell effects between weld, heat affected zone and plate.

3) The fatigue tests under wide and narrow band random load spectra, having different blocks of varying stress levels representative of those experienced in real offshore structures, would be more realistic.

4) Joint fatigue study for loads with a low cyclic frequency of 0.20 Hz - 1 Hz at low stress range levels may yield a high-cycle fatigue life in the range of $8.5 \times 10^6 - 1.5 \times 10^7$ cycles.

5) A more realistic estimate of the stress and strain distributions in the vicinity of the weld and chord intersection need be made using the finite element method, considering the weld dimensions and an appropriate choice of the element sizes.

9. REFERENCES

1. Bouwkamp, J.G., "Tubular Joints under Static and Alternating Loads", Structures and Materials Research Report No. 66-15, Department of Civil Engineering, University of California, Berkeley, June 1966.

2. Toprac, A.A. and Louis, B.G., "Research on the Fatigue Behaviour of Tubular Connections", Structures Fatigue Research Laboratory, Department of Civil Engineering, The University of Texas, Austin, Texas, S.F.R.L. Tech. Report P550-13, May 1970.

3. Evans, J.H. and Adamchak, J.C., Ocean Engineering Structures, M.I.T. Press, Cambridge, Massachusetts, 1969.

4. Michelson, F.C. and Meek, J., "Development of the Tripod Tower Platform Design", Third International Conference on the Behaviour of Offshore Structures (BOSS '82), M.I.T., August 1982.

5. Croasdale, K.R., "Ice Engineering for Offshore Petroleum Exploration in Canada", Fourth International Conference on Port and Ocean Engineering under Arctic Conditions, St. John's, Newfoundland, POAC 1977.

6. API-Code.

7. Becker, J.M., Gerberich, W.W., and Bouwkamp, J.G., "Fatigue Failure of Welded Tubular Joints", American Scoiety of Civil Engineers, Structural Division, Vol. 98, No. ST1, 1972.

8. Dover, W.D., Hibberd, R.D. and Holdbrook, S., "Fatigue Crack Growth in Tubular Welded Joints", Sheffield Conference on the Applications of Fracture Mechanics to Industrial Problems, September 1976.

9. Gibstain, M.B., "Fatigue Failure of T-Joints", Det Norske Veritas Fatigue Testing Program, European Offshore Steel Research Seminar, Cambridge, 1978.

10. Wylde, J.G. and McDonald, A., "The Influence of Joint Dimensions on the Fatigue Strength of Welded Tubular Joints", International Journal of Fatigue, January 1980.

11. Mang, F. and Dutta, D., "Fatigue Strength of Welded Joints of Hollow Sections", Symposium on Tubular Structures, Delft, October 1977.

12. Marshall, P.W., "Basic Considerations for Tubular Joint Design in Offshore Construction", WRC Bulletin 139, April 1974.

13. Dijkstra, O.D. and Vaessen, G.H.G., "The Fatigue Behaviour of Joints in Jacket Constructions", Offshore Technology Conference, paper OTC 2852, Houston, Texas, May 1977.

14. AWS Structural Welding Code, AWS D1.1.

15. "Fixed Offshore Structures", Draft for Development DD55: 1978.

16. Offshore Installations: Guidance on Design and Construction, Department of Energy, U.K., June 1981.

17. Dijkstra, O.D. and deBack, J., "Fatigue Strength of Tubular X and T-Joints", Paper No. 8.4 International Conference: Steel in Marine Structures, Paris, October 1981.

18. Marshall, P.W., "A Review of Stress Concentration Fa t s i Tubular Connections", CE-32 Report, Shell Oil Company, April 1978.

19. Radenkovic, D., "Stress Analysis in Tubular Joints", Paper PS1, International Conference Steel in Marine Structures, Paris, 1981.

20. Wardenier, J., Hollow Section Joints, Delft University Press, 1982.

21. Kuang, J.G., Potvin, A.B. and Lieck, R.D., "Stress Concentrations in Tubular Joints", Paper OTC 2205, Offshore Technology Conference, Houston, Texas, 1975.

22. Gibstein, M.B., "Fatigue Strength of Welded Tubular Joints at Det Norske Veritas Laboratories", Paper 8.5 International Conference - Steel in Marine Structures, Paris, 1981.

23. Blackman, R.B., and Tukey, J.W., "The Measurement of Power Spectra, Dover Publications, New York, 1958.

24. Hicks, J.G., "The Design of the UKOSRP Basic Fatigue Programme", Proceedings of Conference on Fatigue in Offshore Structural Steels, Institution of Civil Engineers, London, 1981.

25. Gibstein, M.G., "Numerical and Experimental Stress Analysis of Tubular Joints with inclined braces", Paper 6.3, International Conference Steel in Marine Structures, Paris, 1981.

26. Walker, E.F., "Effect of Marine Environment", Paper PS4, International Conference Steel in Marine Structures, Paris, 1981.

27. Scott, P.M. and Silvester, D.R.V., "The Influence of Mean Tensile Stress on Corrosion Fatigue Crack Growth in Structural Steel", The Institution of Mechanical Engineers, London, September 1977.

28. Schutz, W., "Procedures for the Prediction of Fatigue Life of Tubular Joints", Paper PS5, International Conference Steel in Marine Structures, Paris, 1981.

29. Vosikovsky, O., "Fatigue-Crack Growth in an X-65 Line-Pipe Steel at Low Cycle Frequencies in Aqueous Environments", Journal of Engineering Materials Technology, Transactions of the ASME, October 1975.

30. Haagensen, P.J., "Improvement of Fatigue Strength of Welded Joints". Paper PS6, International Conference - Steel in Marine Structures, Paris, 1981.

31. Mullen, C.L. and Merwin, J.E., "Fatigue Life Improvement Factors Obtained by Weld Reinforcement and Toe Grinding" Paper OTC 4240, Offshore Technology Conference, Houston, Texas, 1982.

32. Morgan, H.G., "The Effects of Plate Thickness on the Fatigue Performance of Simple Welded Joints", U.K. Department of Energy, To be published.

33. Tomkins, B., "Fatigue Design Rules for Steel Welded Joints in Offshore Structures", Paper OTC 4403, Offshore Technology Conference, Houston, Texas, May 1982.

34. Zwaans, M.H., J.M., Jonkers, P.A.M. and Overbeeke, J.L., "The Endurance of a Welded Joint Under Two Types of Random Loading in Air and Sea Water", Paper 7.3, International Conference - Steel in Marine Structures, Paris, 1981.

35. MSC/NASTRAN User's Manual, Analyst's Guide, The Macneal-Schwendler Corporation, 1980.

36. Intertechnology Ltd., Bulletin - "Protective Coating for Strain Gauge Applications", Don Mills, Ontario, 1980.

37. B & K Mannual for Strain Indicator Type 1526, Denmark, 1974.

38. Gowda, S.S., D.V. Reddy, D.B. Muggeridge and M. Arockiasamy, "Corrosion Fatigue of Tubular Joints in Offshore Structures", First Indian Conference in Ocean engineering, I.I.T., Madras, India, 1981.

39. Knight, J.W., "Corrosion Fatigue Related to Welded Steel Structures - A Literature Survey", Welding Research Institute, Vol. 7, No. 3, 1977.

40. Beale, L.A. and Toprac, A.A., "Analysis of In-plane T, Y, and K Welded Tubular Connections", Welding Research Council Journal, Vol. 125, October 1967.

41. Visser, W., "On the Structural Design of Tubular Joints", OTC 2117, Proceedings Offshore Technology Conference, Houston, Texas, May 1974.

42. Hans, D., Visser, W. and Zunderdorp, H.J., "The Stress Analysis of Tubular Joints for Offshore Structures", SPE 4342, Society of Petroleum Engineers of AIME, 1973.

43. Brink, F.I.A. and van der Krogt, "Design Stress Analysis of a Tubular Cross-Joint Without Internal Stiffening for Offshore Structures", Metal Construction and British Welding Journal, September 1974.

44. de Back, J., "Strength of Tubular Joints", PS7, International Conference - Steel in Marine Structures, Paris, 1981.

45. Iwasaki, T. and Wylde J.G., "Recent Research on the Fatigue Performance of Welded Tubular Joints", Paper 44, Second International Conference on Offshore Welded Structures, The Welding Institute, Cambridge, November 1982.

46. Van Leeuwen, J.L., de Back, J. and Vaessen, G.H.G., "Constant Amplitude Fatigue Tests on Welded Steel Joints Performed in Air and Seawater", Paper 2.1, International Conference - Steel in Marine Structures, Paris, 1981.

47. Irvine, N.M., "Comparison of Tubular Joint Stress Analysis Methods in the Near Weld Region", Paper 1.2, International Conference - Steel in Marine Structures, Paris, 1981.

48. Filler Metal Specifications, American Welding Society (AWS A 5.1-69), 1973.

49. Dijkstra, O.D. and de Back, J., "Fatigue Strength of Tubular T and X-Joints", Paper OTC 3696, Offshore Technology Conference, Houston, Texas, May 1980.

50. Lewis, E.L. and Perkin, R.G., "Salinity - Its Definition and Calculation", Institute of Ocean Sciences, Patricia Bay, Victoria, B.C., Report 76-28, December 1976.

51. American Optical Bulletin (Instruction Manual, 1978).

52. Thome, O., Abrahamsen, E., Eliassen, S., Helgeland, O. and Jensen, F., "Corrosion and Protection of Ofshore Steel Structures", Norges Teknisk - Naturvitenskapelige Forskningsrad (NTNF), Oslo, 1978.

53. HACH Chemical Co. Bulletin, 1971.

54. Sellars, F.H. and Loukakis, T.A., "The Analysis and Modelling of Irregular Waves", Report No. 66-5, Dept. of Naval Architecture and Marine Engineering, M.I.T., Cambridge, Massachusetts, July 1969.

TABLE 1: Mechanical Properties of Steel

Steel Grade	Yield Stress N/mm^2	Tensile Strength N/mm^2	Percentage Elongation %
ASTM A36	248	414	40
ASTM A53	372	483	36

TABLE 2: Chemical Composition of Steel (Weight Percentage)

Steel Grade	C	Mn	P	S	Si
ASTM A36	0.26	0.8	0.04	0.05	0.03
ASTM A53	0.09	1.11	0.002	0.016	0.05

TABLE 3: Joint Parameters (Dimensions in mm)

Steel Grade	Chord D	Brace d	Chord T	Brace t	α= 2L/D	β= d/D	γ= D/2T	τ= t/T
ASTM A36 and A53	318.75	133	9.4	6.5	11.47	0.43	16.38	0.70

TABLE 4: Mechanical Properties of Electrodes (Ref. 48)

Electrode Type	AWS-ASTM E6011	AWS-ASTM E7018
Yield Strength, σ_y N/mm^2	330 - 420	400 - 483
Tensile Strength, σ_u N/mm^2	413 - 510	483 - 586
Elongation in 50 mm, %	20 - 30	22 - 30
Reduction in Area, %	35 - 60	55 - 75

TABLE 5: Welding Details (Fig. 10)

Electrode Type	Electrode Size (mm)	Current (Amperes)	Weld Speed (mm/min.)	Applicable Joint Detail (Fig. 10)		
				Detail	Range of Dihedral Angle	Location
E6011 and E7018	3.2 - 3.97	90 - 140 130-220	100 - 150	AA BB CC DD	180° - 135° 150° - 50° 75° - 30° 40° - 15°	Toe Zone Side Zone Transient Zone Heel Zone

TABLE 6: Range of Seawater Parameters

Parameter	Range
Salinity	34.5% - 38%
Chlorinity	19.93 g/l - 21.04 g/l
pH	7.25 - 7.55
Dissolved O_2 concentration	10 mg/l - 12 mg/l
Temperature	-1°C - +1°C
HCO_3^- concentration	0.06 - 0.26 g/l

TABLE 7: Static Strain Readings for Joint One (Corr. 1)
(Vertical 133 kN; Horizontal ∓ 53 kN)

Gauge No.	Strains (Microstrains) Horizontal Load.		Gauge No.	Strains (Microstrains) Horizontal Load	
	-53 KN	+ 53 KN		- 53 KN	+ 53 KN
1	150	-130	28	70	-60
2	240	-220	29	80	-120
3	150	-160	30	30	-40
4	340	-280	31	-	-
5	360	-480	32	-	-
6	560	-780	33	-	-
7	340	-460	34	-10	50
8	560	-400	35	-60	45
9	640	-520	36	-	-
10	340	-300	37	-170	40
11	290	-340	38	-60	+20
12	300	-320	39	-200	380
13	180	-280	40	-210	250
14	125	-200	41	-360	170
15	-	-	42	-370	170
16	-	-	43	-	-
17	-	-	44	-280	130
18	-	-	45	-180	160
19	-60	- 70	46	-155	130
20	-495	-390	47	30	+60
21	-350	-210	48	-200	70
22	-100	- 60	49	30	+60
23	-	-	50	-250	160
24	-75	- 20	51	-180	140
25	-103	-185	52	-	-
26	-20	-130	53	-	-
27	-20	-			

TABLE 8: Static Strain Readings for Joint Two (Corr. 2)
(Vertical 178 kN; Horizontal ∓ 62 kN)

Gauge No.	Strains (Microstrains) Horizontal Load.		Gauge No.	Strains (Microstrains) Horizontal Load	
	-62 kN	+62 kN		-62 kN	+62 kN
1	220	-280	20	80	60
2	420	-300	21	80	0
3	340	-560	22	240	-40
4	520	-920	23	200	-20
5	320	-540	24	-320	+160
6	240	-420	25	-520	+240
7	240	-540	26	-500	+160
8	260	-320	27	-160	+100
9	460	-200	28	-340	+200
10	320	-200	29	-280	+320
11	180	-120	30	-160	+180
12	320	-40	31	-100	+200
13	160	0	32	-140	+280
14	100	100	33	- 40	+200
15	60	40	34	100	-80
16	120	0	35	140	-180
17	280	-80	36	280	-120
18	300	-120	37	400	-240
19	220	20			

TABLE 9: Static Strain Readings for Joint Three (Corr. 3)
(Vertical 178 kN; Horizontal ∓ 80 kN)

Gauge No.	Strains (Microstrains) Horizontal Load		Gauge No.	Strains (Microstrains) Horizontal Load	
	-80 kN	+80 kN		-80 kN	+80 kN
1	640	-320	19	+180	200
2	520	-400	20	260	-100
3	640	-340	21	140	-200
4	520	-720	22	-80	600
5	840	-1140	23	-140	780
6	500	-680	24	-280	580
7	200	-80	25	-160	+300
8	340	-180	26	- 20	+460
9	40	-15	27	- 40	+440
10	200	-80	28	-120	+420
11	100	-60	29	-220	+120
12	100	-20	30	-100	+120
13	940	-640	31	-100	320
14	800	-740	32	-260	+280
15	840	-440	33	-180	400
16	60	-20	34	360	-340
17	320	-100	35	-120	140
18	40	-10			

TABLE 10: Static Strain Readings for Joint Four (Corr. 4)
(Vertical 133 kN; Horizontal ∓ 58 kN)

Gauge No.	Strains (Microstrains) Horizontal Load		Gauge No.	Strains (Microstrains) Horizontal Load.	
	-58 kN	+58 kN		-58 kN	+58 kN
1	+260	-240	17	280	-320
2	200	-200	18	220	-180
3	100	-100	19	80	-60
4	+380	-300	20	240	-160
5	+500	-400	21	60	-40
6	+840	-640	22	+ 60	-40
7	+480	-380	23	100	-20
8	+660	-500	24	+100	-40
9	+360	-240	25	- 60	60
10	+240	-140	26	-200	440
11	+160	- 40	27	- 80	120
12	80	- 30	28	- 80	80
13	600	-440	29	-140	+300
14	700	-560	30	- 80	+260
15	360	-320	31	- 60	+220
16	460	-380	32	- 20	+160

Table 11: Fatigue Test Results

Specimen No.	Number of cycles for (in 10^4)					Ratio of Fatigue Lives		
	15% Strain Drop N_1	First Visible Crack		Crack Through Chord Wall N_3	End of Test N_4	$\frac{N_1}{N_4}$	$\frac{N_2}{N_4}$	$\frac{N_3}{N_4}$
		N_2	Length mm					
Corr. 1	6.53	8.90	2.5	11.68	23.3	0.280	0.382	0.501
Corr. 2	41.7	61.00	9.0	82.86	95.0	0.439	0.642	0.872
Corr. 3	1.26	-	-	1.52	3.3	0.382	-	0.461
Corr. 4	7.20	8.20	6.0	11.20	20.6	0.350	0.398	0.544
Dry 1	15.35	23.80	10.0	81.15	95.0	0.162	0.251	0.854

Table 12(a) Hot Spot Strain Range and Strain Concentration Factor (SNCF) - Main Chord

Specimen No.	Weld Condition	Nominal Strain Range (με)	Hot Spot Strain Range (με)			SNCF	
			Measured	Extrapolated	FEM	Extrapolated	FEM
Corr. 1	as welded	160	1340	1365	1549	8.53	9.68
Corr. 2	toe ground	84	684	713	815	8.49	9.69
Corr. 3	toe ground	240	1980	2070	2327	8.63	9.70
Corr. 4	as welded	173	1480	1550	1680	8.96	9.71
Dry 1	toe ground (Fig. 26, Section 8)	84	684	713	815	8.49	9.69

Table 12(b) Hot Spot Strain Range and Strain Concentration Factor (SCF) - Branch Tube

Specimen No.	Weld Condition	Nominal Strain Range (μs)	Hot Spot Strain Range (μs)			SNCF	
			Measured	Extrapolated	FEM	Extrapolated	FEM
Corr. 1	as welded	160	640	730	1052	4.56	6.58
Corr. 2	toe ground	84	333	378	553	4.50	6.59
Corr. 3	toe ground	240	940	1100	1578	4.58	6.58
Corr. 4	as welded	173	700	790	1138	4.57	6.58
Dry 1	toe ground	84	333	378	553	4.50	6.59

Table 13: Hot Spot Stress Range and Stress Concentration Factor (SCF) - Main Chord

Specimen No.	Nominal Stress Range (N/mm^2)	Hot Spot Stress Range (N/mm^2)				SCF					
		Measured	FEM	Marshall (18)	Radenkovic (19)	Measured	FEM	Marshall (18)	Radenkovic (19)	Parametric Equations: Beale & Toprac (40) Eqn. (12)	Parametric Equations: Visser (41) Eqn. 13
Corr. 1(AW)	31.92	295.76	333.17	267.94	299.41	9.29	11.82	8.39	9.38		
Corr. 2(TG)	16.76	152.24	198.34	129.97	156.54	9.09	11.83	7.76	9.34		
Corr. 3(TG)	47.89	464.07	566.47	395.91	454.48	9.69	11.83	8.26	9.49	4.86	4.04
Corr. 4(AW)	34.58	343.66	408.96	295.93	340.96	9.94	11.83	8.56	9.86		
Dry 1	16.76	152.24	198.34	129.97	156.54	9.09	11.83	7.76	9.34		

( ) Numbers in parenthesis refer to references

AW = As Welded

TG = Toe Ground

Table 14: Summary of Crack Growth Data (Fig. 35) - Right of Centre Line

Test Specimen: Joint Corr. 1
Load Range = 106 kN
Frequency = 0.20 Hz
$N_4 = 23.3 \times 10^4$ cycles

Main Crack Length = 164 mm
Secondary Crack Length = 23 mm
Total Crack Length = 430 mm

Location of crack tip	Increase in cycles in 10^4 units	Total number of cycles in 10^4 units (N)	$\frac{N}{N_4}$	Increase in crack length (mm)	Crack growth rate (10^{-4} mm/cycle)	Crack length (mm)
0	8.90	8.90	6.38	2.5	0.28	2.5
A	0.45	9.35	0.40	5.5	12.22	8
B	0.59	9.94	0.42	3	5.08	11
C	0.66	10.60	0.46	12	18.18	23
D	1.29	11.89	0.51	11	8.53	34
E	0.68	12.57	0.54	-	-	
	0.53	13.10	0.56	14	26.42	48
F	0.90	14.00	0.60	23	25.55	71
	0.50	14.50	0.62	16	32.00	87
G	0.98	15.48	0.66	23	23.47	110
H	0.67	16.15	0.69	13	19.40	123
	1.24	17.39	0.75	10	8.07	133
I	0.66	18.05	0.77	7	10.61	140
	1.00	19.05	0.82	9	9.00	149
	1.11	20.16	0.86	9	8.11	158
	1.39	21.55	0.93	-	-	-
J	1.75	23.30	1.00	6	3.43	164

Table 15: Summary of Crack Growth Data (Fig. 36) - Right of Centre Line

Test Specimen: Joint Corr. 2
Load Range = 125 kN
Frequency = Variable
N_4 = 95x10^4 cycles

Main Crack Length = 214 mm
Secondary Crack Length = 93 mm
Total Crack Length = 552 mm

Location of crack tip	Increase in cycles in 10^4 units	Total number of cycles in 10^4 units (N)	$\frac{N}{N_4}$	Increase in crack length (mm)	Crack growth rate (10^{-4} mm/cycle)	Crack length (mm)
0	61.00	61.00	0.64	9	0.15	9
A	3.05	64.00	0.67	15	5.00	24
B	1.9	65.90	0.69	26	13.68	50
C	3.93	69.83	0.74	18	4.58	68
D	0.82	70.65	0.74	10	12.19	78
-	-	-	-	-	-	-
E	2.73	73.38	0.77	13	4.76	91
F	1.92	75.30	0.79	10	5.21	101
-	-	-	-	-	-	-
G	9.60	84.90	0.89	37	3.85	138
H	1.45	86.35	0.91	17	11.72	155
I	1.43	87.78	0.92	16	11.19	171
J	2.42	90.20	0.95	14	5.78	185
K	2.37	92.57	0.97	6	2.53	191
L	2.26	94.83	0.99	7	3.10	198
M	2.43	95.00	1.00	16	6.58	214

Table 16: Summary of Crack Growth Data (Fig. 37) - Right of Centre Line

Test Specimen: Joint Corr. 3
Load Range = 160 kN
Frequency = 0.20 Hz
$N_4 = 3.3 \times 10^4$ cycles

Main Crack Length = 229 mm
Secondary Crack Length = 116 mm
Total Crack Length = 717 mm

Location of crack tip	Increase in cycles in 10^4 units	Total number of cycles in 10^4 units (N)	$\frac{N}{N_4}$	Increase in crack length (mm)	Crack growth rate (10^{-4} mm/cycle)	Crack length (mm)
A	1.53	1.53	0.46	83	54.25	83
B	0.17	1.70	0.52	27	158.82	110
	0.26	1.96	0.59	29	111.54	139
C	0.09	2.05	0.62	13	144.44	152
D	0.15	2.20	0.67	16	106.67	168
E	0.16	2.36	0.72	10	62.50	178
F	0.23	2.59	0.79	20	86.96	198
	0.24	2.83	0.86	16	66.67	214
	0.28	3.11	0.94	8	28.57	222
G	0.19	3.30	1.00	7	36.84	229

Table 17: Summary of Crack Growth Data (Fig. 38) - Right of Centre Line

Test Specimen: Joint Corr. 4

Load Range = 116 kN
Frequency = 0.20 Hz
N_4 = 20.6×10^4 cycles

Main Crack Length = 263 mm
Secondary Crack Length = 41 mm
Total Crack Length = 509 mm

Location of crack tip	Increase in cycles in 10^4 units	Total number of cycles in 10^4 units (N)	$\frac{N}{N_4}$	Increase in crack length (mm)	Crack growth rate (10^{-4} mm/cycle)	Crack length (mm)
A	0.85	9.05	0.44	14	16.47	14
B	0.47	9.52	0.46	11	23.40	24
C	1.07	10.59	0.51	66	61.68	91
D	0.47	11.06	0.54	34	72.34	125
E	1.34	12.40	0.60	4	2.98	129
F	0.65	13.05	0.63	5	7.69	134
G	1.25	14.30	0.69	39	31.20	173
H	0.95	15.25	0.74	18	18.95	191
I	0.92	16.17	0.78	19	20.65	210
J	0.73	16.90	0.82	12	16.44	222
K	0.86	17.76	0.86	28	32.56	250
L	1.48	19.24	0.93	10	6.77	260
M	1.36	20.60	1.00	3	2.21	263

Table 18: Summary of Crack Growth Data (Fig. 39) - Right of Centre Line

Test Specimen: Joint Dry-1
Load Range = 125 kN
Frequency = Variable
$N_4 = 95 \times 10^4$ cycles

Main Crack Length = 210 mm
Secondary Crack Length = 4 mm
Total Crack Length = 417 mm

Location of crack tip	Increase in cycles in 10^4 units	Total number of cycles in 10^4 units (N)	$\frac{N}{N_4}$	Increase in crack length (mm)	Crack growth rate (10^{-4} mm/cycle)	Crack length (mm)
0	23.80	23.80	0.25	5	0.21	5
A	3.77	27.57	0.29	6	1.59	11
B	0.57	28.14	0.29	10	17.54	21
C	0.30	28.44	0.30	6	20.00	27
D	7.36	35.80	0.38	15	2.04	42
E	8.54	44.34	0.47	9	1.05	51
F	6.42	70.76	0.75	10	1.56	61
G	4.12	74.88	0.79	8	1.94	68
H	3.78	78.66	0.83	9	2.38	77
I	4.27	82.93	0.87	25	5.86	102
J	2.10	85.03	0.89	24	11.43	126
K	1.17	86.20	0.91	14	11.96	140
L	2.30	88.50	0.93	33	14.35	173
M	1.10	89.60	0.94	10	9.09	183
N	3.71	92.31	0.97	21	5.66	204
P	2.69	95.00	1.00	6	2.23	210

Table 19: Summary of Crack Growth Data (Fig. 35) - Left of Centre Line

Test Specimen: Joint Corr. 1

Load Range = 106 kN
Frequency = 0.20 Hz
N_4 = 23.2x10^4 cycles

Main Crack Length = 217 mm
Secondary Crack Length = 26 mm
Total Crack Length = 430 mm

Location of crack tip	Increase in cycles in 10^4 units	Total number of cycles in 10^4 units (N)	$\frac{N}{N_4}$	Increase in crack length (mm)	Crack growth rate (10^{-4} mm/cycle)	Crack length (mm)
A'	9.35	9.35	0.40	9	0.96	9
-	0.59	9.94	0.43	11	18.64	20
-	0.66	10.60	0.46	20	30.30	40
B'	1.29	11.89	0.51	40	31.01	80
C'	0.68	12.57	0.54	12	17.65	92
D'	0.53	13.10	0.56	17	32.08	109
E'	0.90	14.00	0.60	16	17.78	125
-	0.50	14.50	0.62	19	38.00	144
F'	0.98	15.48	0.66	15	15.31	159
-	0.67	16.15	0.69	9	13.43	168
G'	1.24	17.39	0.75	9	7.26	177
H'	0.66	18.05	0.78	8	12.12	185
I'	1.00	19.05	0.81	7	7.00	192
-	1.11	20.16	0.86	11	9.91	203
J'	1.39	21.55	0.92	8	5.76	211
K'	1.75	23.30	1.00	6	3.43	217

Table 20: Summary of Crack Growth Data (Fig. 36) - Left of Centre Line

Test Specimen: Joint Corr. 2
Load Range = 125 kN
Frequency = Variable
N_4 = 95 x10^4 cycles

Main Crack Length = 143 mm
Secondary Crack Length = 109 mm
Total Crack Length = 552 mm

Location of crack tip	Increase in cycles in 10^4 units	Total number of cycles in 10^4 units (N)	$\frac{N}{N_4}$	Increase in crack length (mm)	Crack growth rate (10^{-4} mm/cycle)	Crack length (mm)
A'	64.00	64.00	0.67	13	0.20	13
B'	1.90	65.90	0.69	10	5.26	23
C'	3.93	69.83	0.74	12	3.05	35
D'	0.82	70.65	0.75	15	18.29	50
F'	4.65	75.30	0.79	10	21.51	60
G'	9.60	84.90	0.89	7	0.73	67
H'	1.45	86.35	0.91	14	9.66	81
I'	1.43	87.78	0.92	17	11.89	98
J'	2.42	90.20	0.95	18	7.44	116
K'	2.37	92.57	0.97	7	2.93	123
L'	2.26	94.83	0.99	9	3.98	132
M'	2.43	95.00	1.00	11	4.53	143

Table 21: Summary of Crack Growth Data (Fig. 37) - Left of Centre Line

Test Specimen: Joint Corr. 3
Load Range = 160 kN
Frequency = 0.20 Hz
N_4 = 3.3×10^4 cycles

Main Crack Length = 260 mm
Secondary Crack Length = 112 mm
Total Crack Length = 717 mm

Location of crack tip	Increase in cycles in 10^4 units	Total number of cycles in 10^4 units (N)	$\frac{N}{N_4}$	Increase in crack length (mm)	Crack growth rate (10^{-4} mm/cycle)	Crack length (mm)
C'	1.53	1.53	0.46	103	67.32	103
D'	0.17	1.70	0.52	16	94.12	119
	0.26	1.96	0.59	15	57.69	134
E'	0.09	2.05	0.62	21	233.33	155
F'	0.15	2.20	0.67	24	160.00	179
G'	0.16	2.36	0.72	29	181.25	208
H'	0.23	2.59	0.79	15	65.22	223
	0.24	2.83	0.86	19	79.17	242
	0.28	3.11	0.94	12	42.86	254
I'	0.19	3.30	1.00	6	31.58	260

Table 22: Summary of Crack Growth Data (Fig. 38) - Left of Centre Line

Test Specimen: Joint Corr. 4

Load Range = 116 kN
Frequency = 0.20 Hz
N_4 = 20.6x10^4 cycles

Main Crack Length = 173 mm
Secondary Crack Length = 32 mm
Total Crack Length = 509 mm

Location of crack tip	Increase in cycles in 10^4 units	Total number of cycles in 10^4 units (N)	$\frac{N}{N_4}$	Increase in crack length (mm)	Crack growth rate (10^{-4} mm/cycle)	Crack length (mm)
0	8.20	8.20	0.39	6	0.73	6
A'	0.85	9.05	0.44	16	18.82	22
B'	0.47	9.52	0.46	19	40.43	41
G'	0.78	14.30	0.69	25	5.23	66
H'	0.53	14.83	0.72	26	49.06	92
	0.17	15.00	0.73	13	76.47	105
	0.60	15.60	0.76	20	33.33	125
I'	0.57	16.17	0.79	6	10.53	131
J'	0.73	16.90	0.82	15	20.55	146
	0.60	17.50	0.85	9	15.00	155
K'	0.26	17.76	0.86	7	26.92	162
	0.74	18.50	0.89	5	6.76	167
M'	2.10	20.60	1.00	6	2.86	173

Table 23: Summary of Crack Growth Data (Fig. 39) - Left of Centre Line

Test Specimen: Joint Dry-1
Load Range = 125 kN
Frequency = Variable
N_4 = 95.0x10^4 cycles

Main Crack Length = 198 mm
Secondary Crack Length = 5 mm
Total Crack Length = 417 mm

Location of crack tip	Increase in cycles in 10^4 units	Total number of cycles in 10^4 units (N)	$\frac{N}{N_4}$	Increase in crack length (mm)	Crack growth rate (10^{-4} mm/cycle)	Crack length (mm)
A'	27.57	27.57	0.29	11	0.39	11
B'	3.77	28.44	0.30	6	1.59	17
C'-C"	1.76	30.20	0.30	8	4.54	25
D'	1.74	31.94	0.34	8	4.59	33
E'	12.40	44.34		15		48
E"	12 40	44.34	0.47	5	1.61	53
F'and F"	26.42	70.76	0.75	15	0.57	68
F"-E'	3.99	74.75	0.79	9	2.26	77
H'	3.91	78.66	0.83	13	3.33	90
I'	4.27	82.93	0.87	10	2.34	100
J'	2.10	85.03	0.89	25	11.91	125
K'	1.17	86.20	0.91	11	9.40	136
L'	2.30	88.50	0.93	26	11.31	162
M'	1.10	89.60	0.94	13	11.82	175
N'	2.71	92.31	0.97	17	6.27	192
P'	2.69	95.00	1.00	6	2.23	198

Table 24: Comparison of Fatigue Test Results ( )

	Specimen Dimensions (mm)				Type of Loading (IPB)	Hot Spot Stress+/ Strain Range* (N/mm^2)	Fatigue Life (cycles)	Remarks
	Chord		Brace					
	D	T	d	t				
Present Investigation	318	9.4	133	6.5	CA	295.76+/1340*	2.33×10^5	-
					VA	152.24+/684*	9.50×10^5	
					CA	464.07+/1980*	3.30×10^4	
					CA	343.66+/1480*	2.06×10^5	
Available Literature	457	16	457	16	CA	271+	5.0×10^5	Ref. 16
	457	16	457	16	CA	401+	3.3×10^5	Ref. 16
	472	22	340	22	CA	242+	1.9×10^5	Ref. 16
	685	40	343	22	CA	146+	7.6×10^5	Ref. 16
	947	44	683	44	CA	126+	6.5×10^5	
	168	6.3	168	T = 4.47	CA	2000*	2.65×10^5	Ref. 10
	168	6.3		T = 3.15		1285*	3.7×10^5	Ref. 49
	168	6.3		3.15		1445*	4.8×10^5	Ref. 49

IPB - In-plane Bending
CA - Constant Amplitude
VA - Variable Amplitude

FIG. 1 JACKET-TYPE STEEL STRUCTURE (EVANS & ADAMCHAK, 1968)

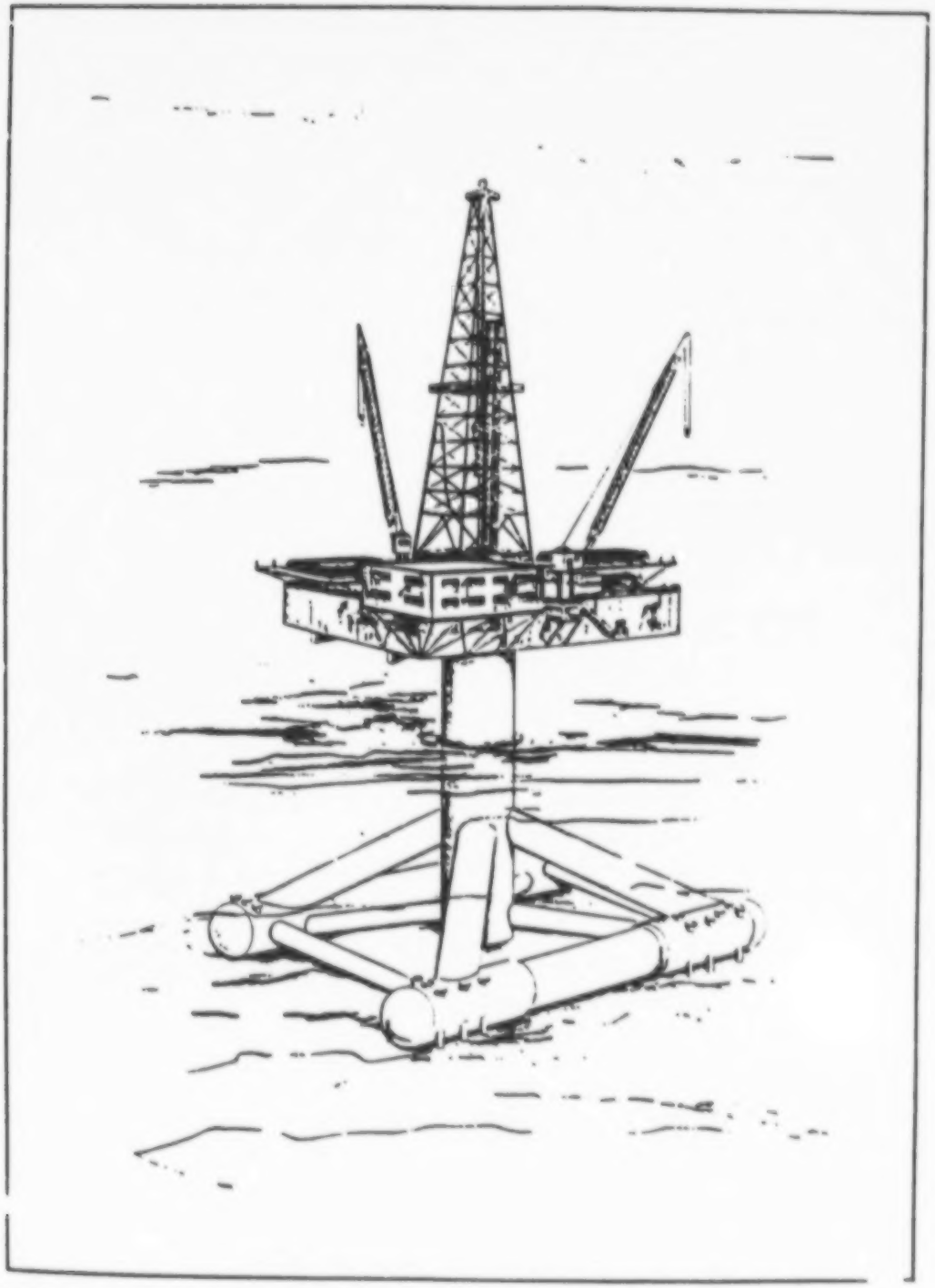

FIG.2 COOK INLET MONOPOD PLATFORM (EVANS & ADAMCHAK, 1969)

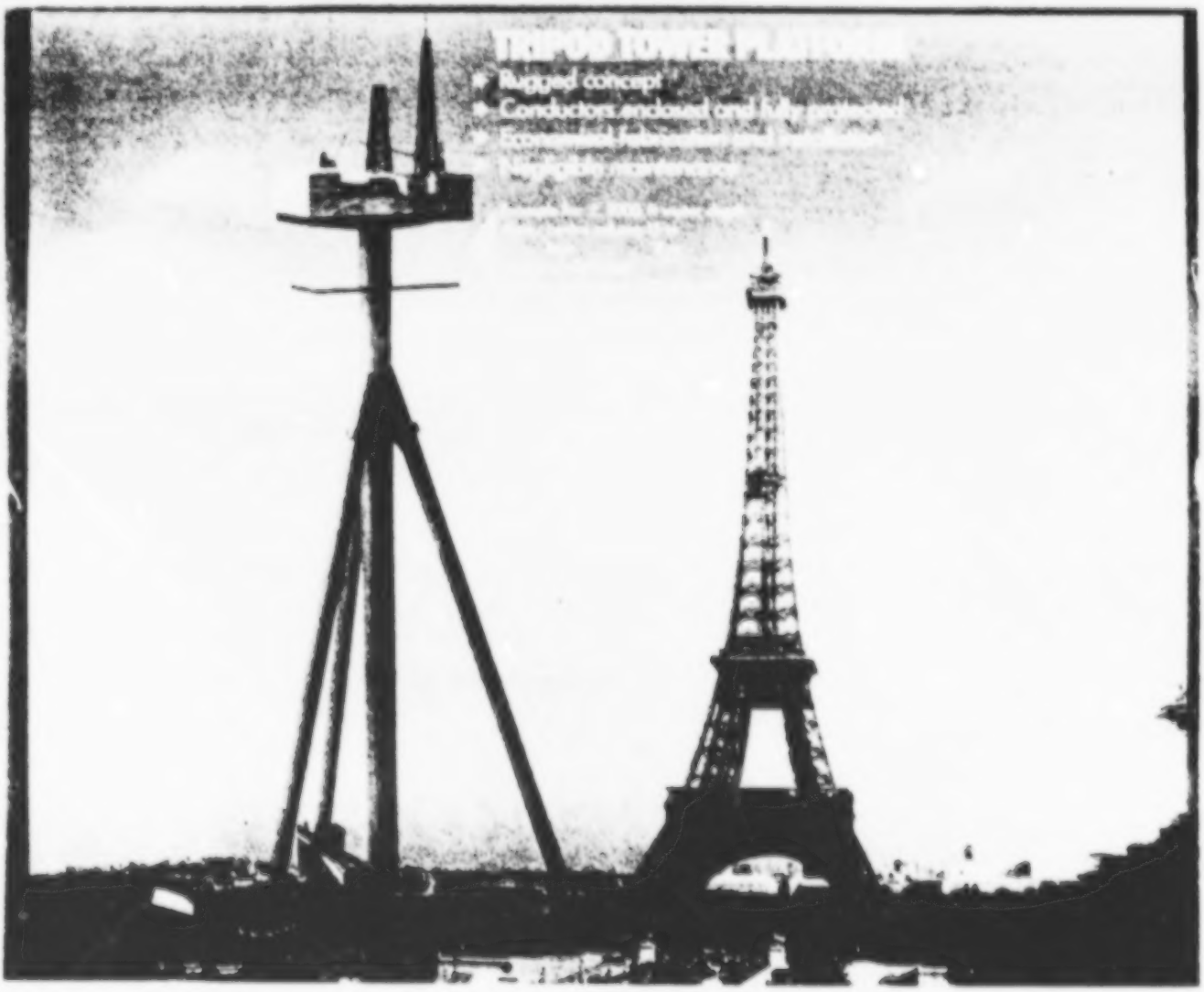

FIG.3 TRIPOD TOWER PLATFORM (MICHELSON & MEEK, 1982)

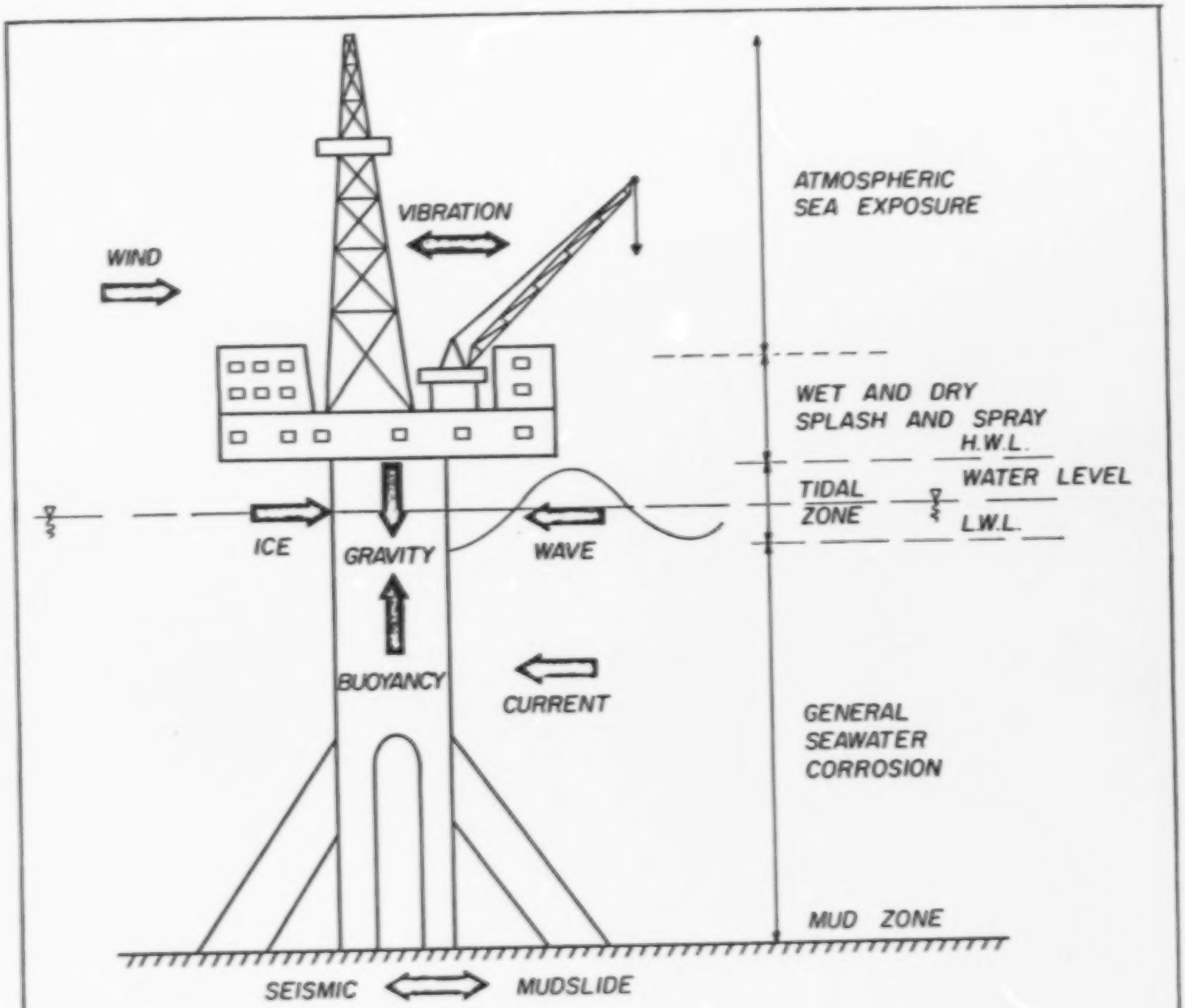

FIG. 4 MAJOR PLATFORM LOADS AND CORROSION ZONES

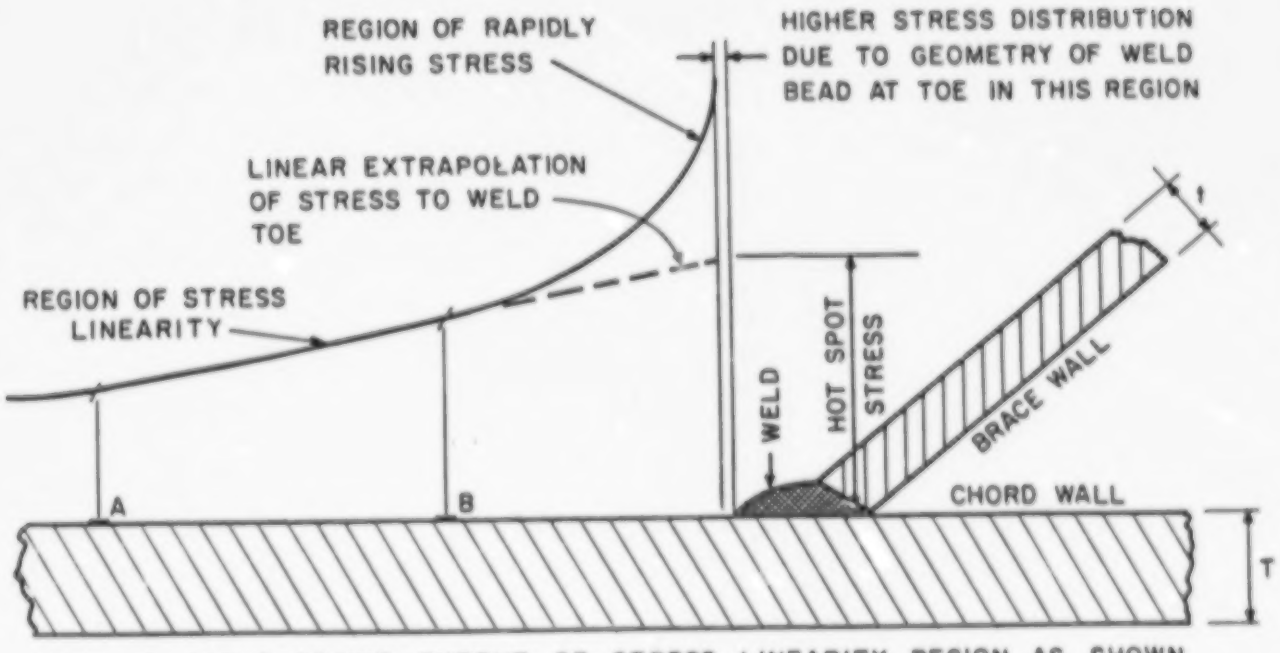

NOTE: A AND B DEFINE EXTENT OF STRESS LINEARITY REGION AS SHOWN BELOW.

(a)

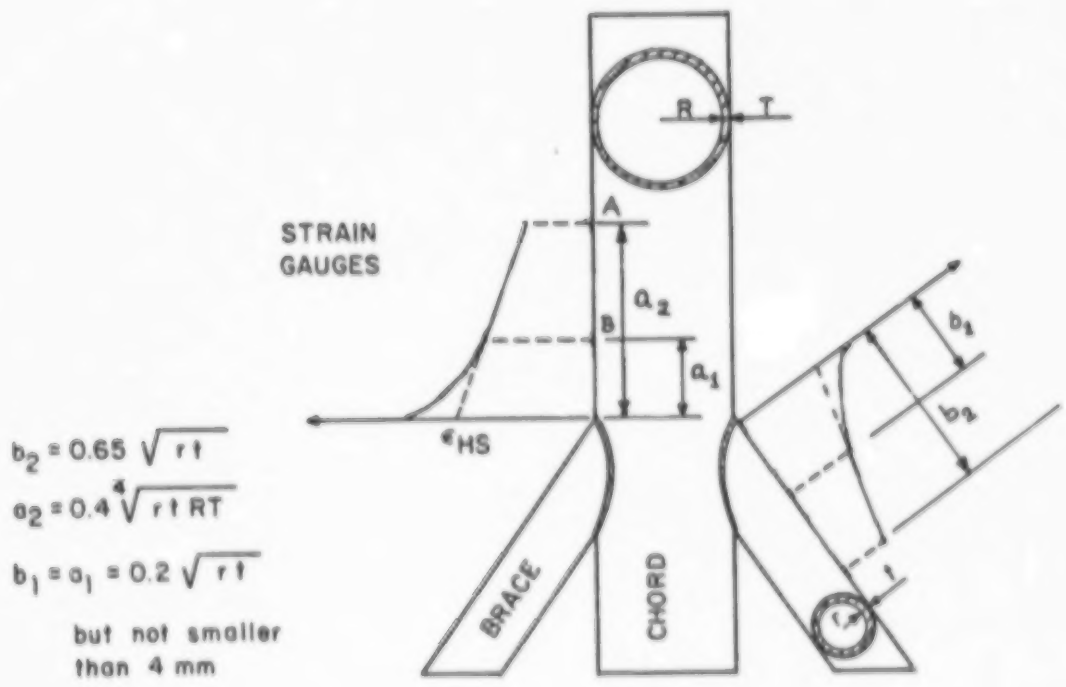

$b_2 = 0.65\sqrt{rt}$

$a_2 = 0.4\sqrt[4]{rt\,RT}$

$b_1 = a_1 = 0.2\sqrt{rt}$

but not smaller than 4 mm

(b)

FIG. 5 DIAGRAMMATIC REPRESENTATION DEFINING IDEALIZED HOT SPOT STRESS

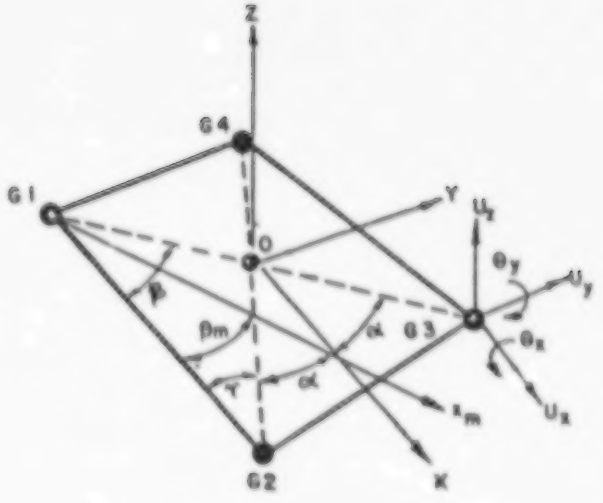

FIG. 6 QUADRILATERAL ELEMENT - QUAD4

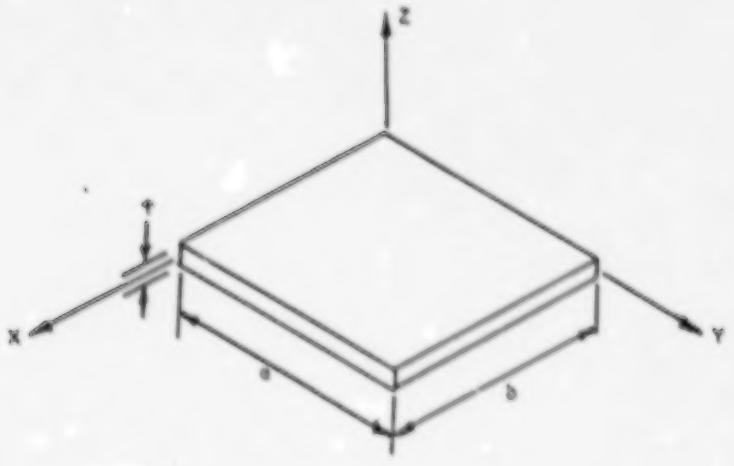

(a) Plate Configuration

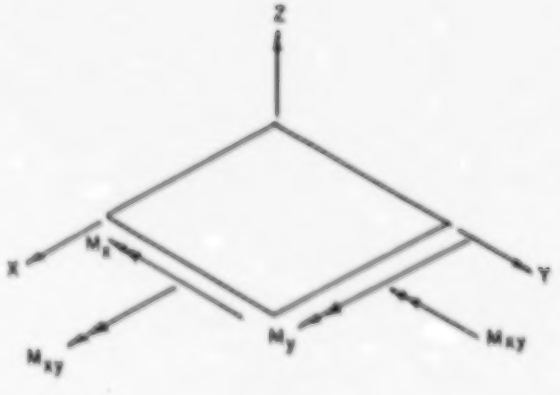

(b) Positive Moment Resultants

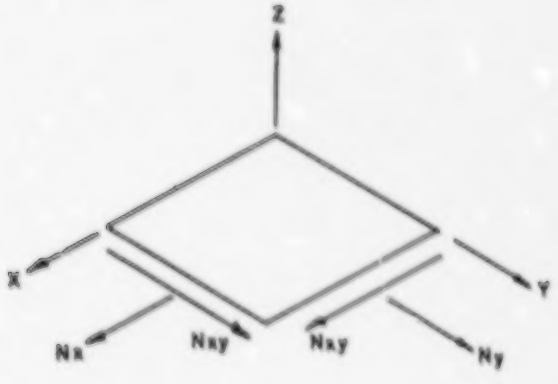

(c) Positive Force Resultants

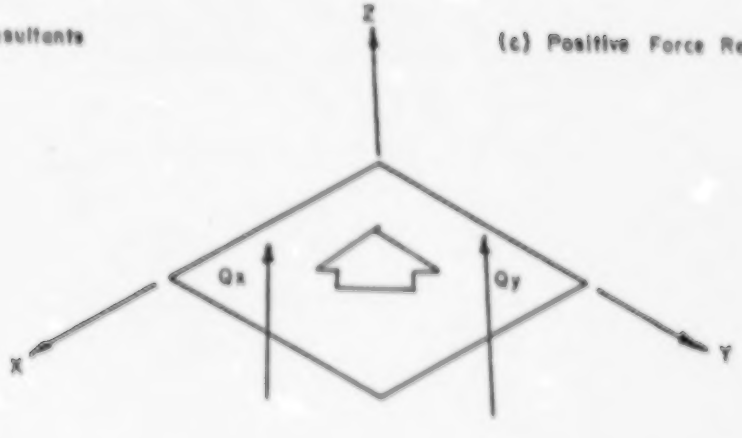

(d) Transverse Load and Shear Forces

FIG. 7 FORCE AND MOMENT RESULTANTS

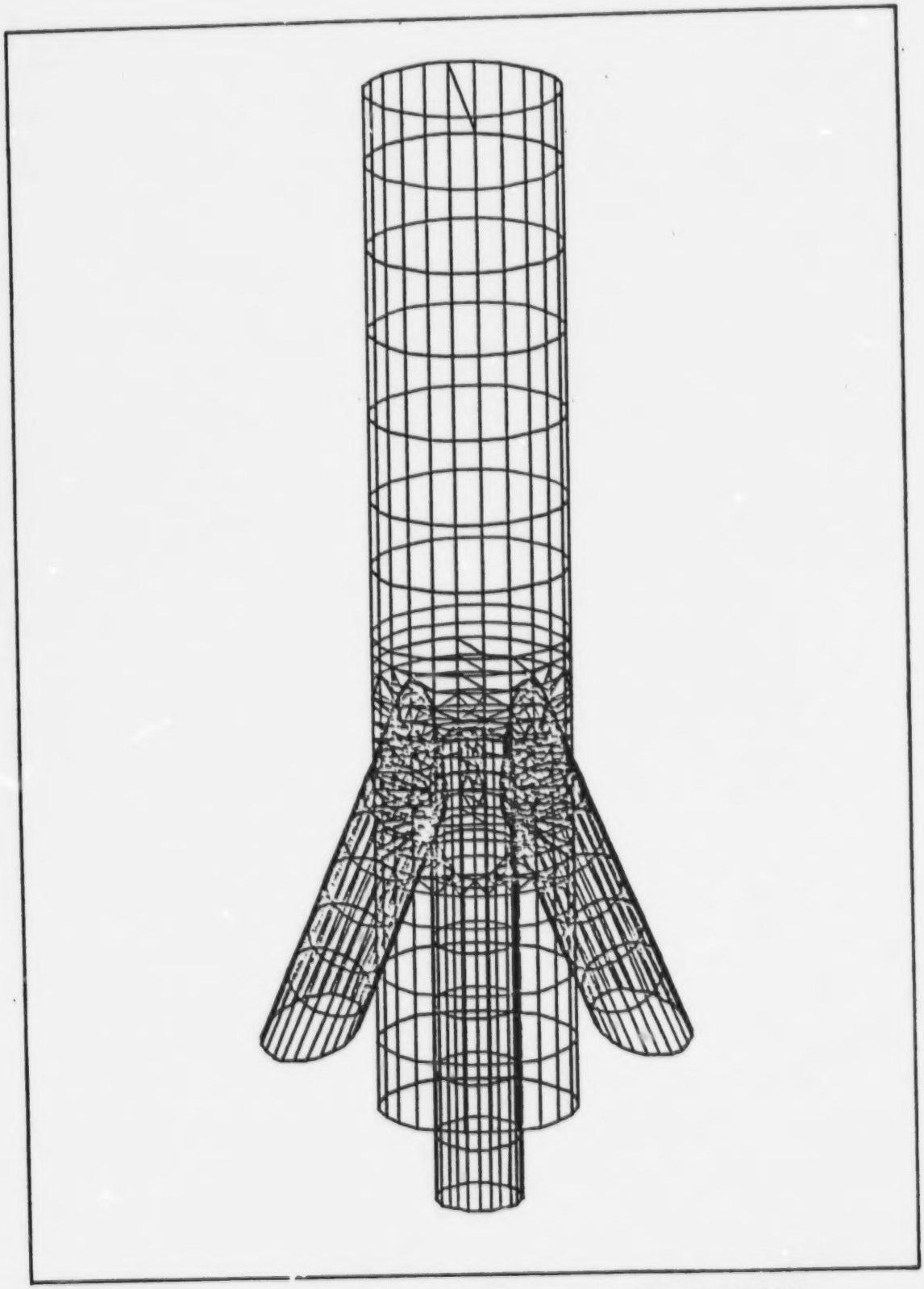

FIG. 8 a) FINITE ELEMENT MESH GENERATION

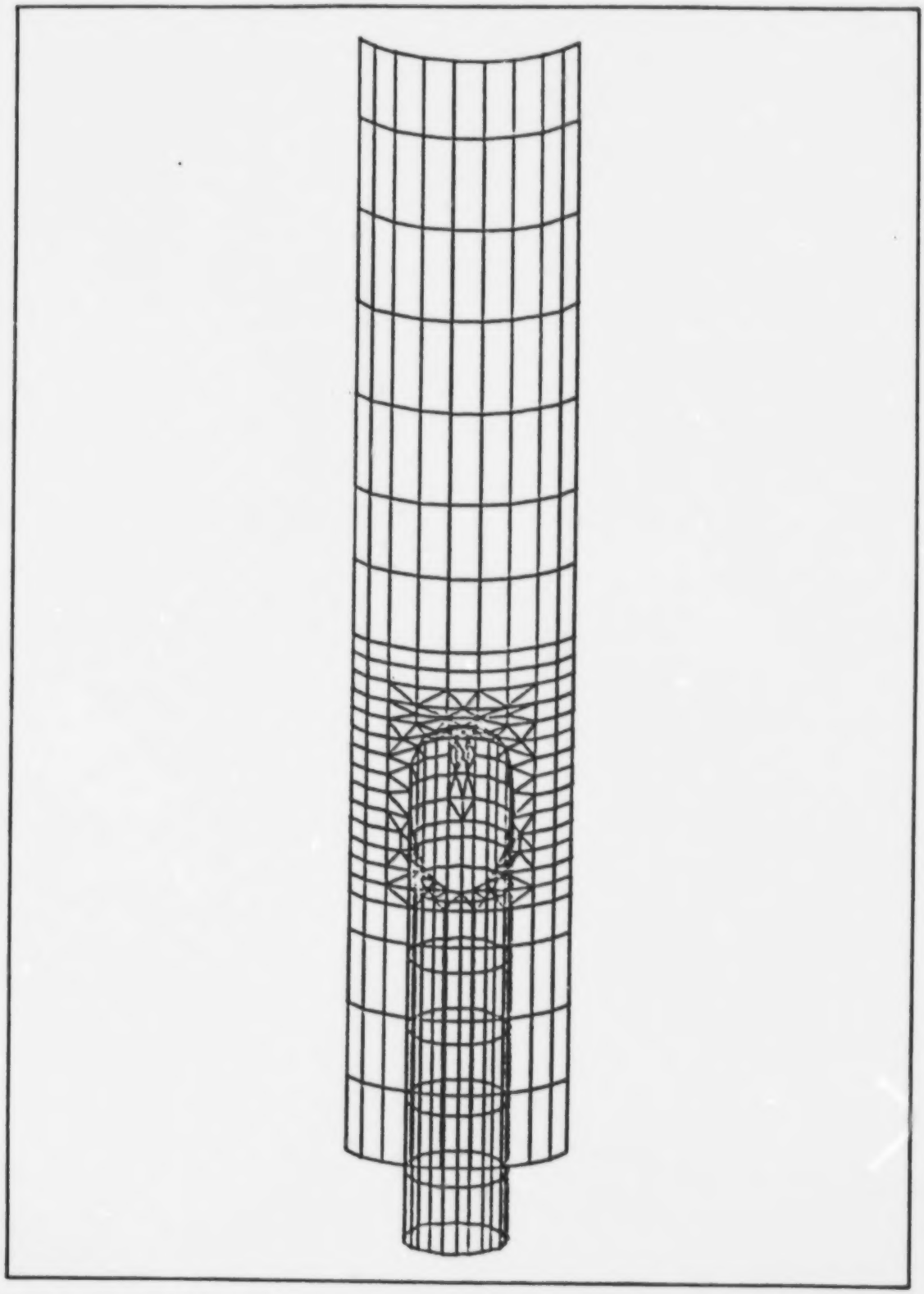

FIG. 8 b) FINITE ELEMENT MESH WITH FIRST BRANCH TUBE

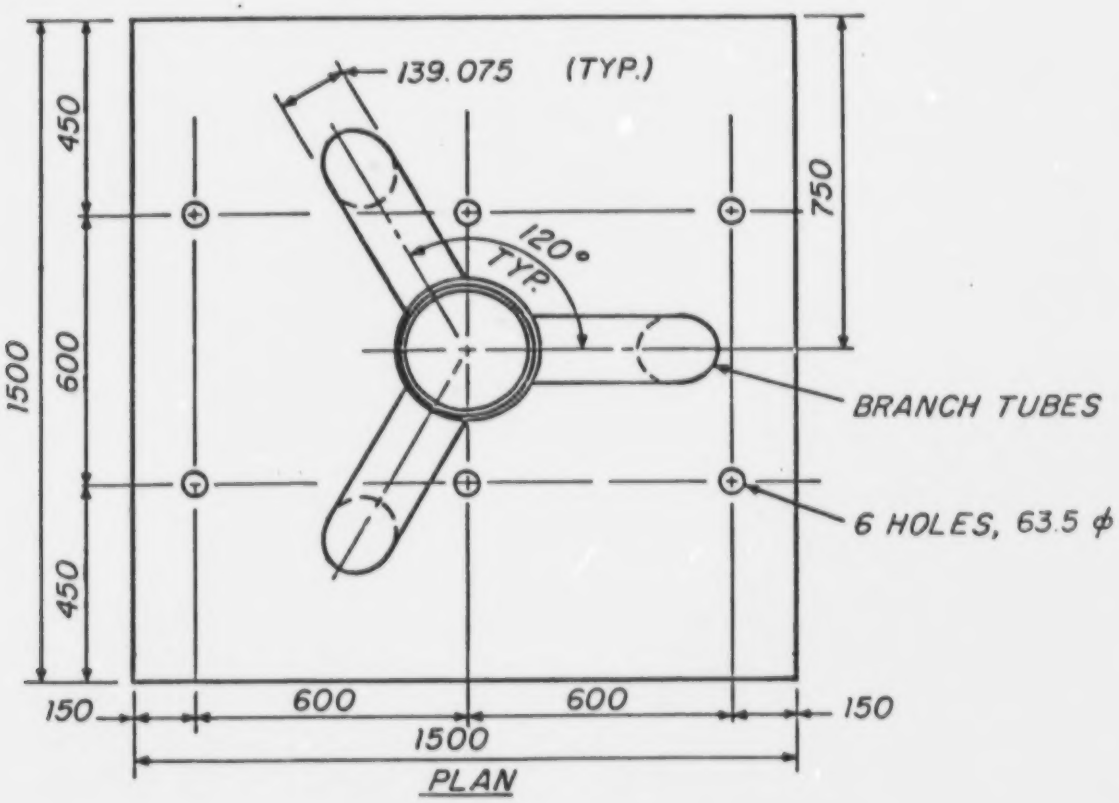

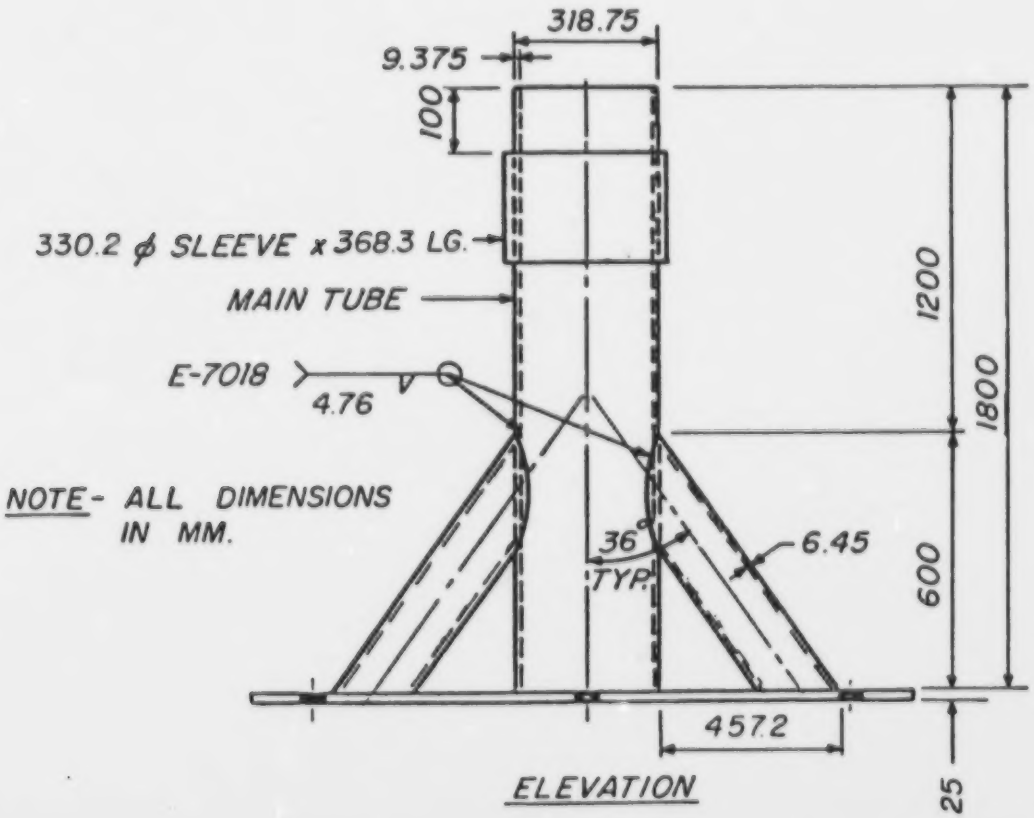

FIG. 9 MONOPOD TUBULAR JOINT

WELDING DETAILS

ALL WELD TOES TO BECOME TANGENT TO PIPE SURFACE IN A SMOOTH RADIUS

ANGLE a IS MEASURED PERPENDICULAR TO JOINT LINE AND ON THE OUTSIDE OF PIPE

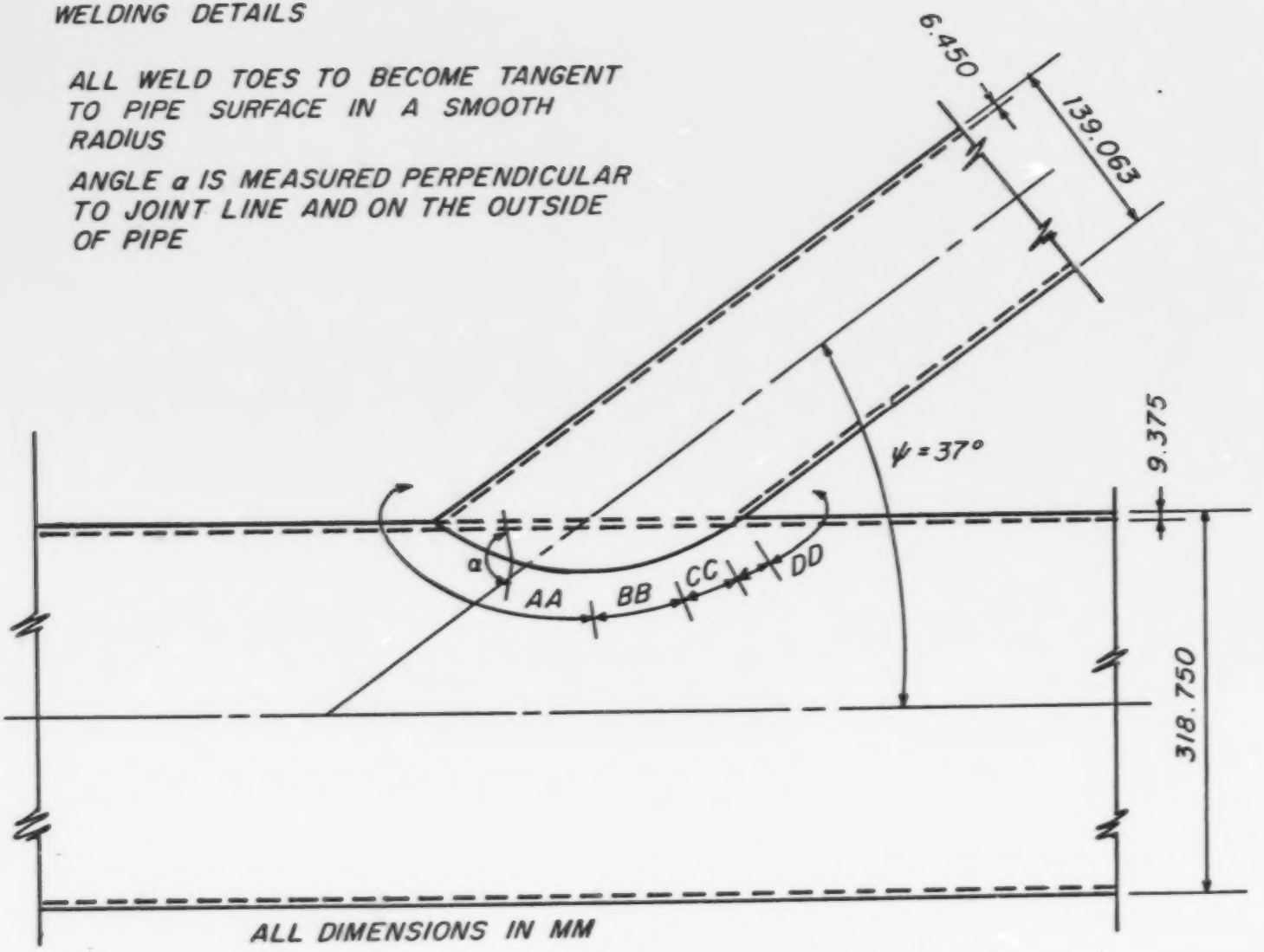

TYPICAL CONNECTION ELEVATION

FIG. 10 TUBE WELD CONNECTION ELEVATION

WELD DETAILS FROM ONE SIDE ONLY – TYPES I & II

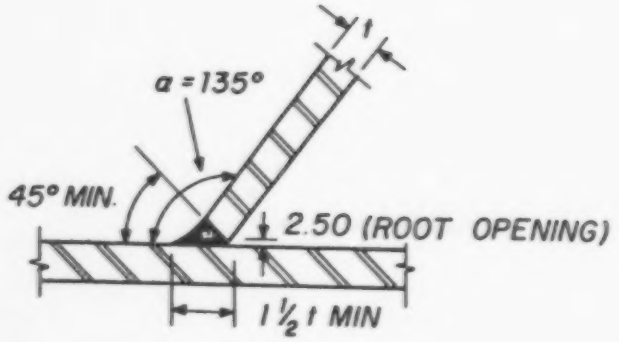

(a) AA (TOE)

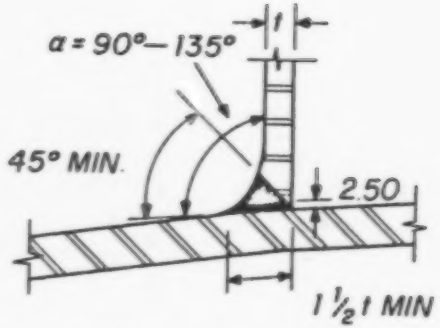

(b) BB (SIDE)

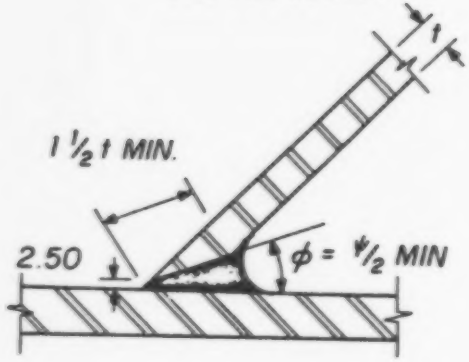

(c) CC (TRANSITION)

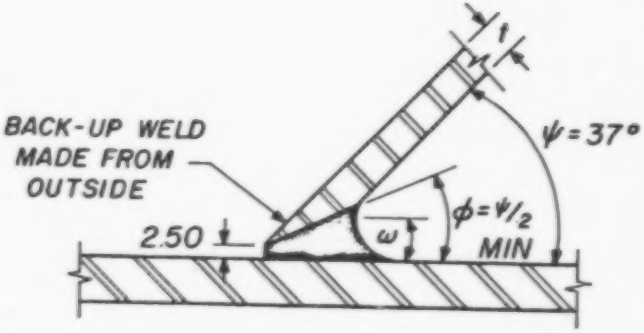

(d) TRANSITION FROM DETAIL CC TO DD BY GRADUAL UNIFORM BEVELLING

NOTE = BACK-UP WELD INITIAL PASSES DISCONTINUED UNTIL WIDTH OF GROOVE "W" IS SUFFICIENT TO ASSURE SOUND WELDING T = 12.5 MM. MIN, W = 5 MM. MIN

FIG. 11 WELDING DETAILS

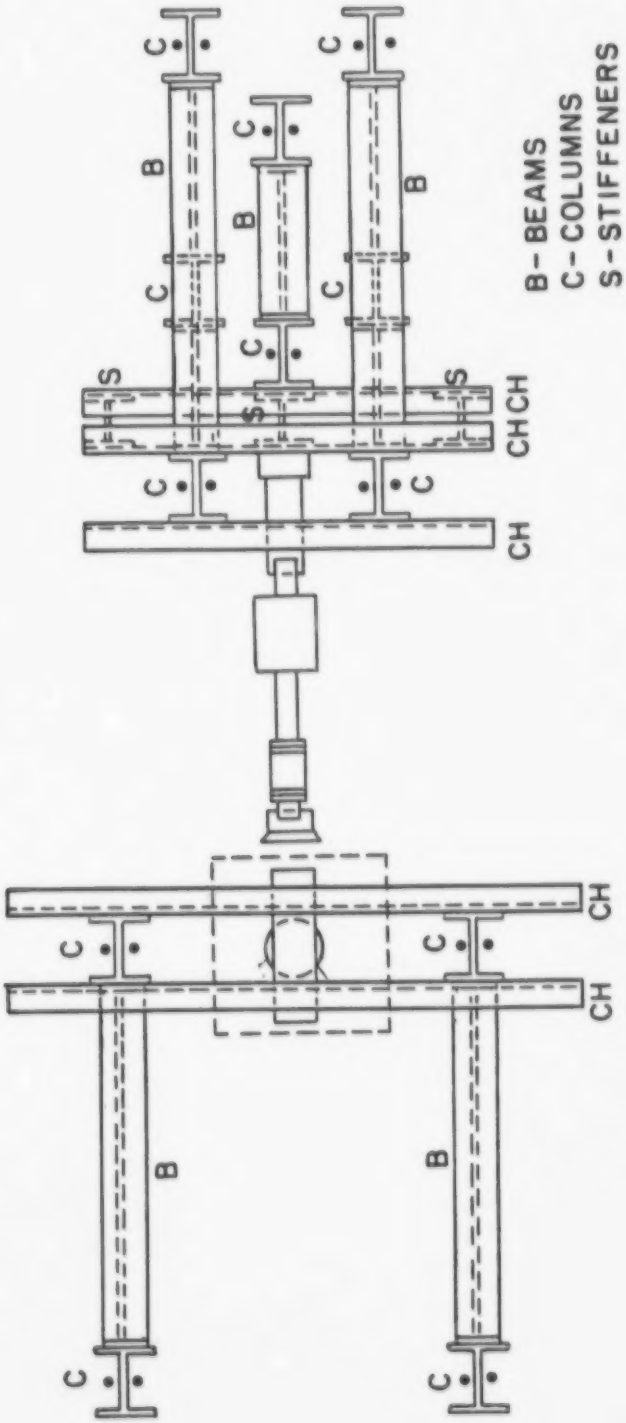

FIG. 12 PLAN OF TEST ASSEMBLY

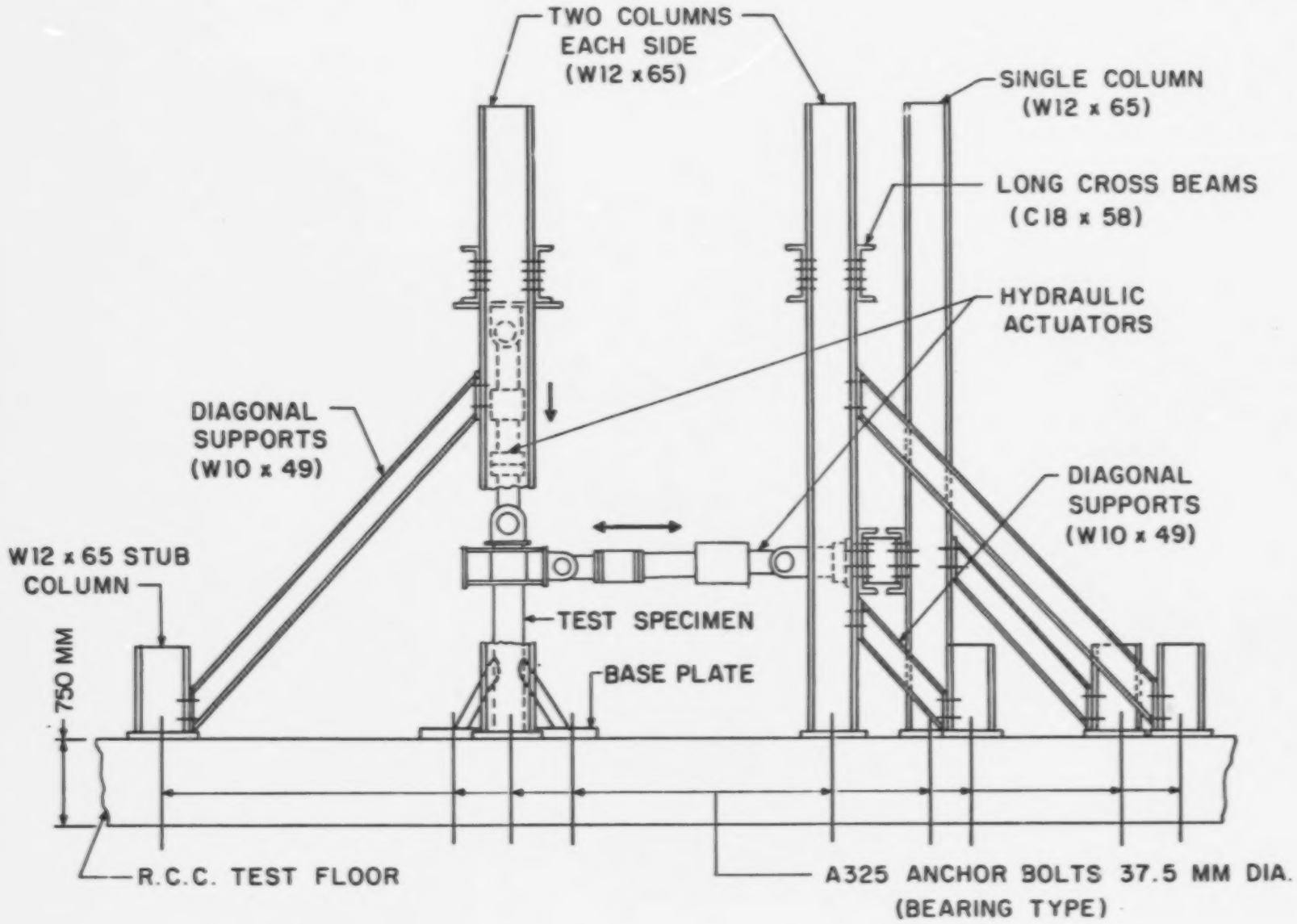

FIG. 13 TEST ASSEMBLY FOR FATIGUE LOADING

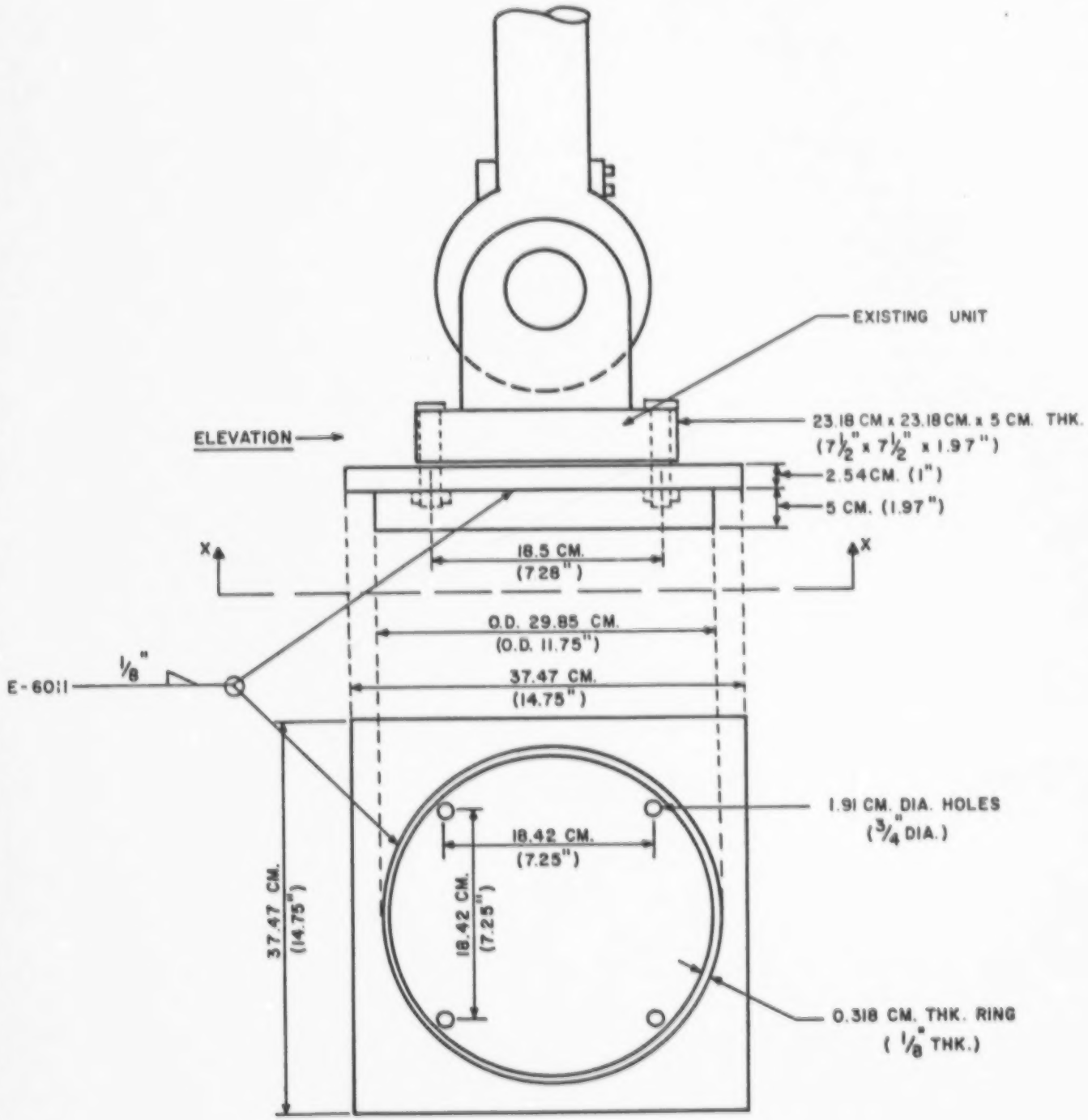

BOTTOM VIEW X - X

FIG. 14 CONNECTION UNIT FOR VERTICAL LOADING

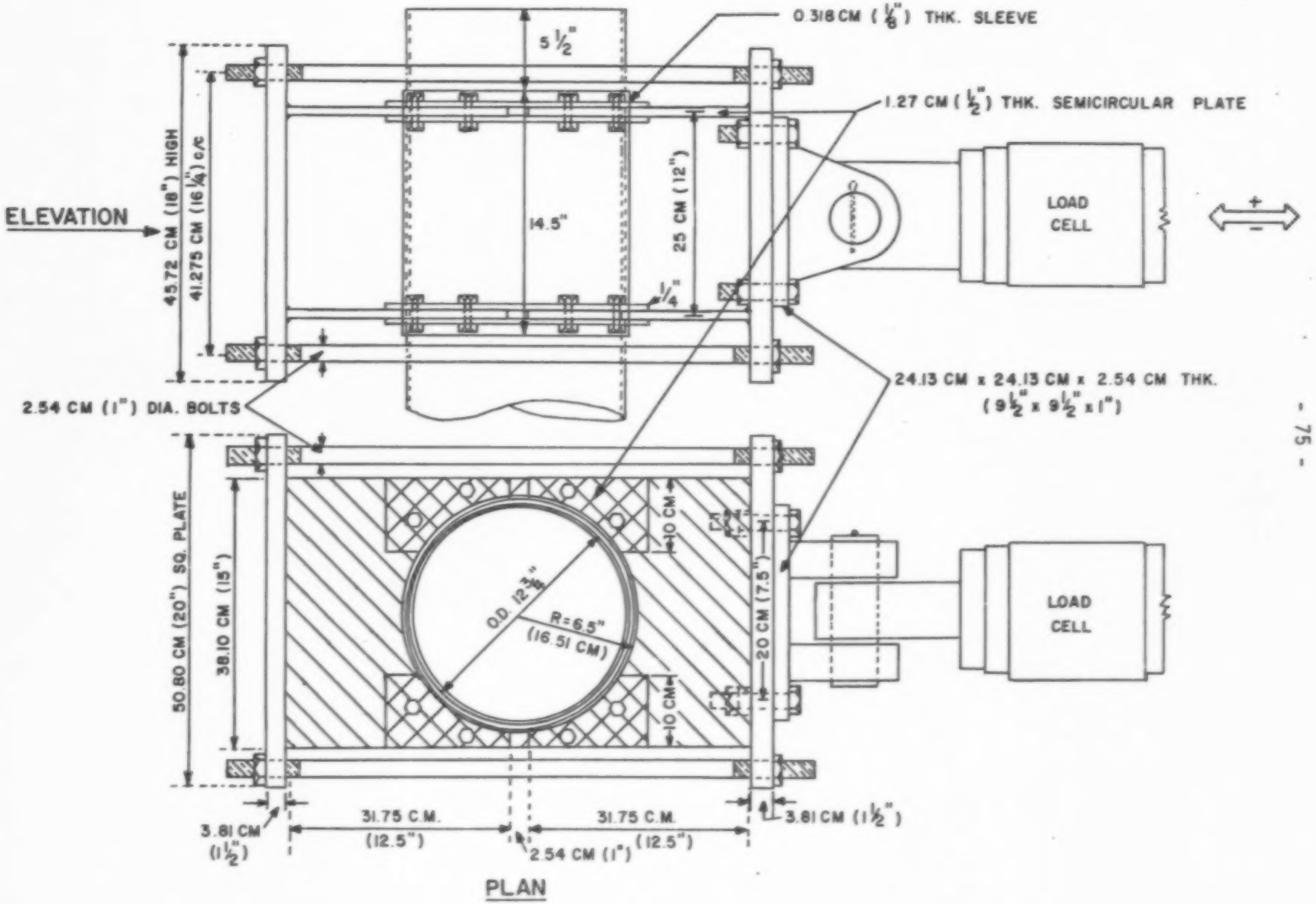

FIG. 15 CONNECTION UNIT FOR HORIZONTAL LOADING

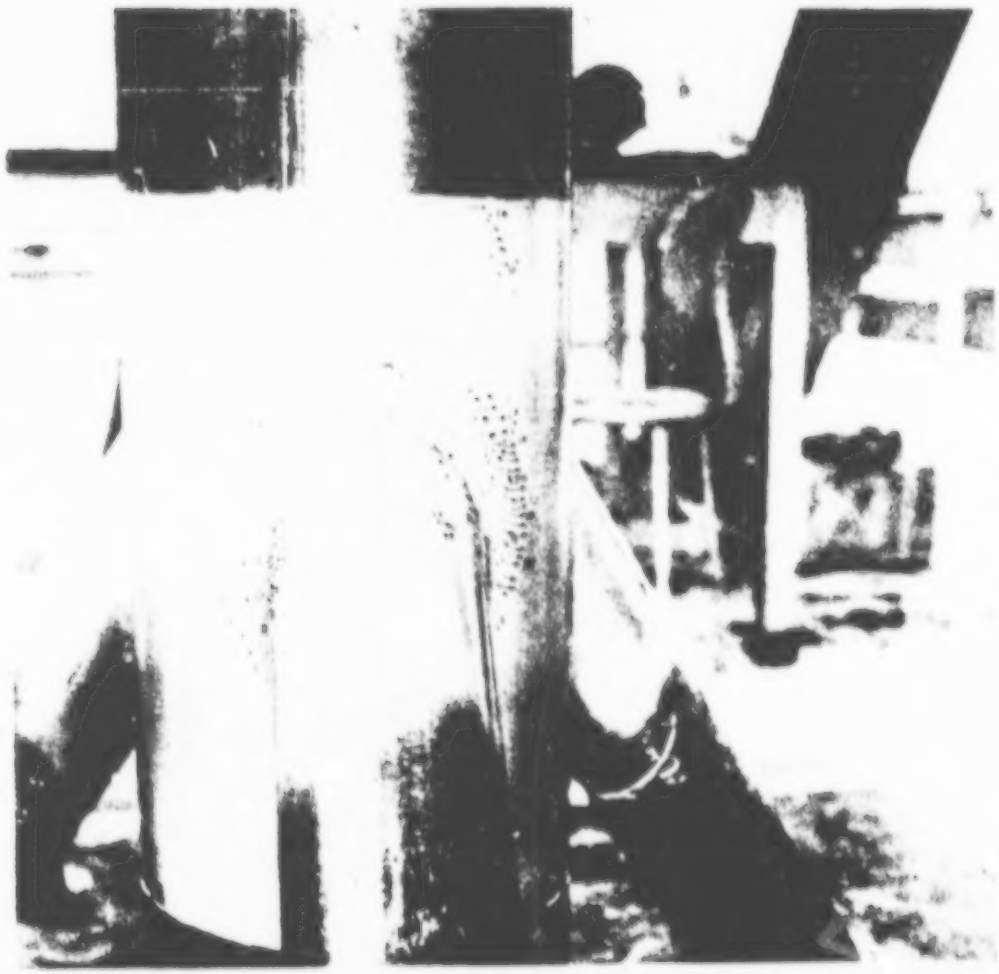

FIG. 16 BRITTLE COATING CRACKS AROUND JOINT INTERSECTION

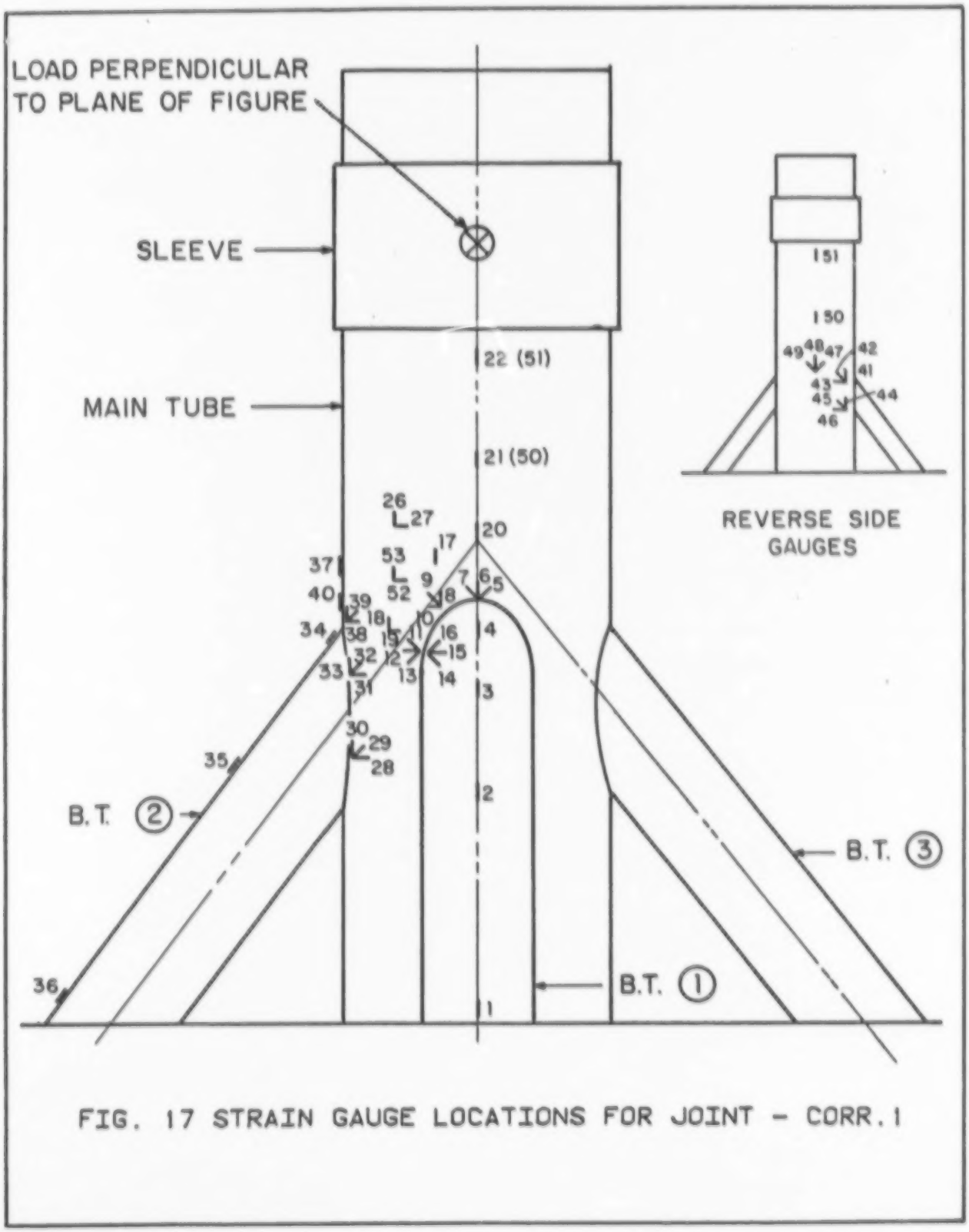

FIG. 17 STRAIN GAUGE LOCATIONS FOR JOINT - CORR. 1

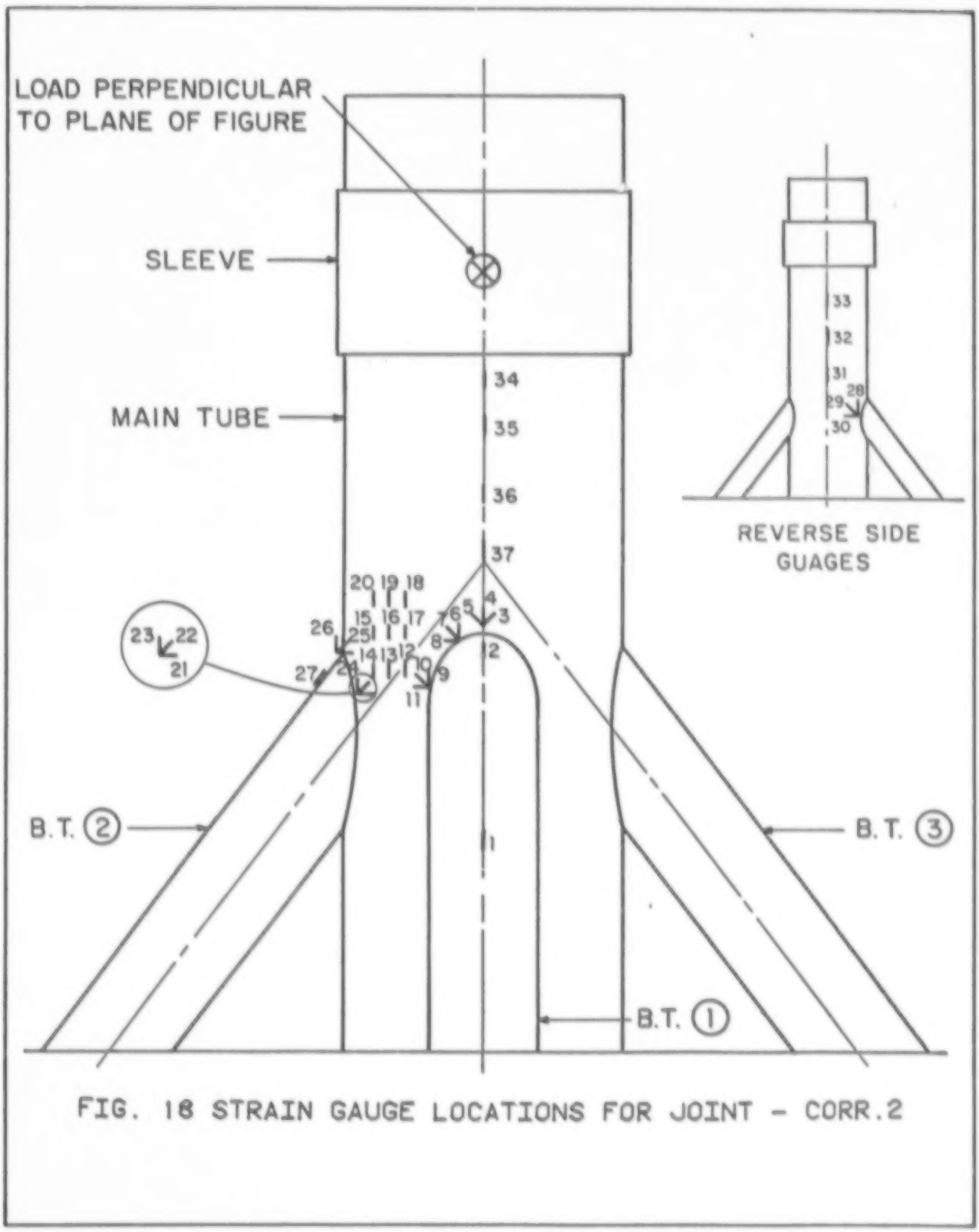

FIG. 18 STRAIN GAUGE LOCATIONS FOR JOINT - CORR.2

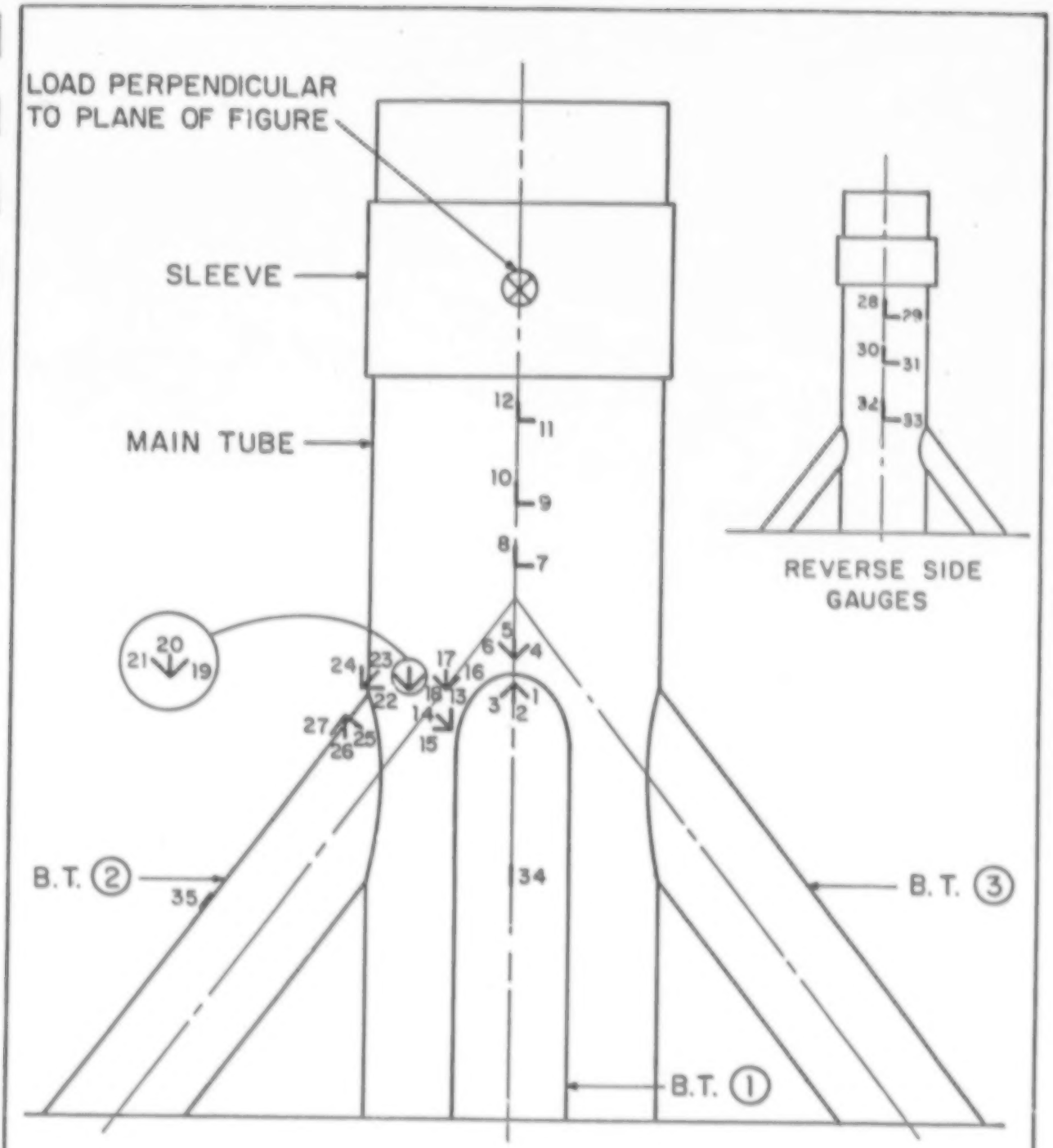

FIG. 19 STRAIN GAUGE LOCATIONS FOR JOINT - CORR.3

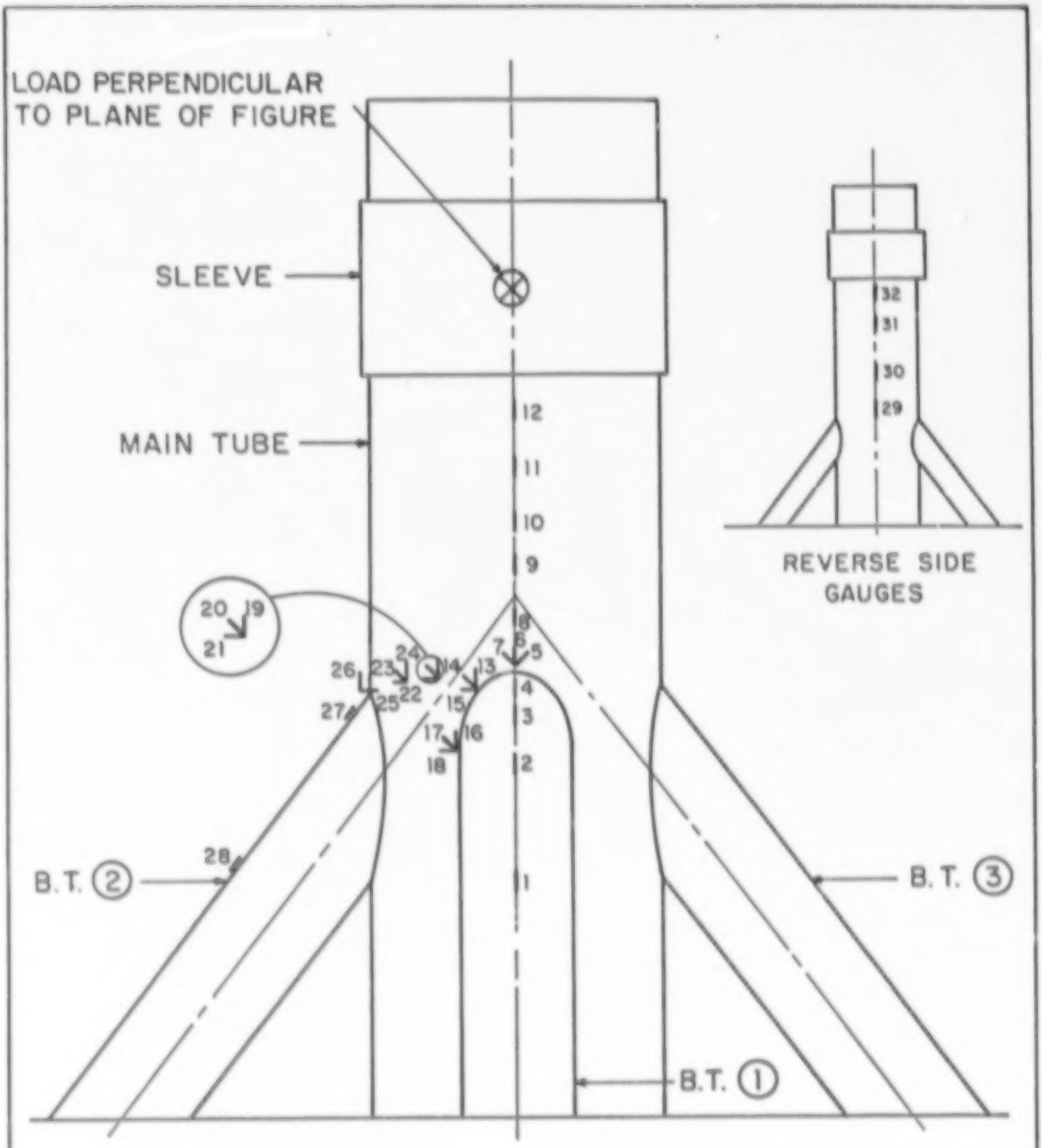

FIG. 20 STRAIN GAUGE LOCATIONS FOR JOINT - CORR. 4

Protective Coatings for Strain Gage Applications.

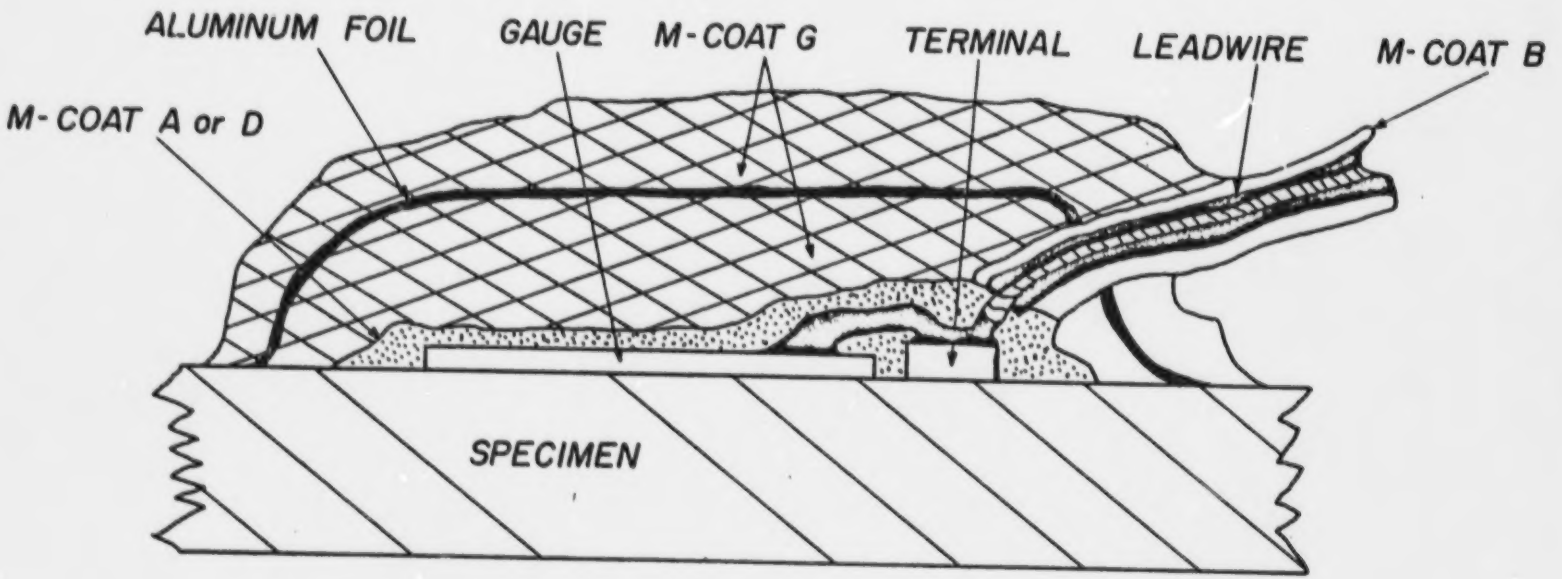

FIG. 21 CROSS-SECTIONAL VIEW OF PROTECTIVE COATINGS FOR STRAIN GAUGE INSTALLATIONS IN WATER

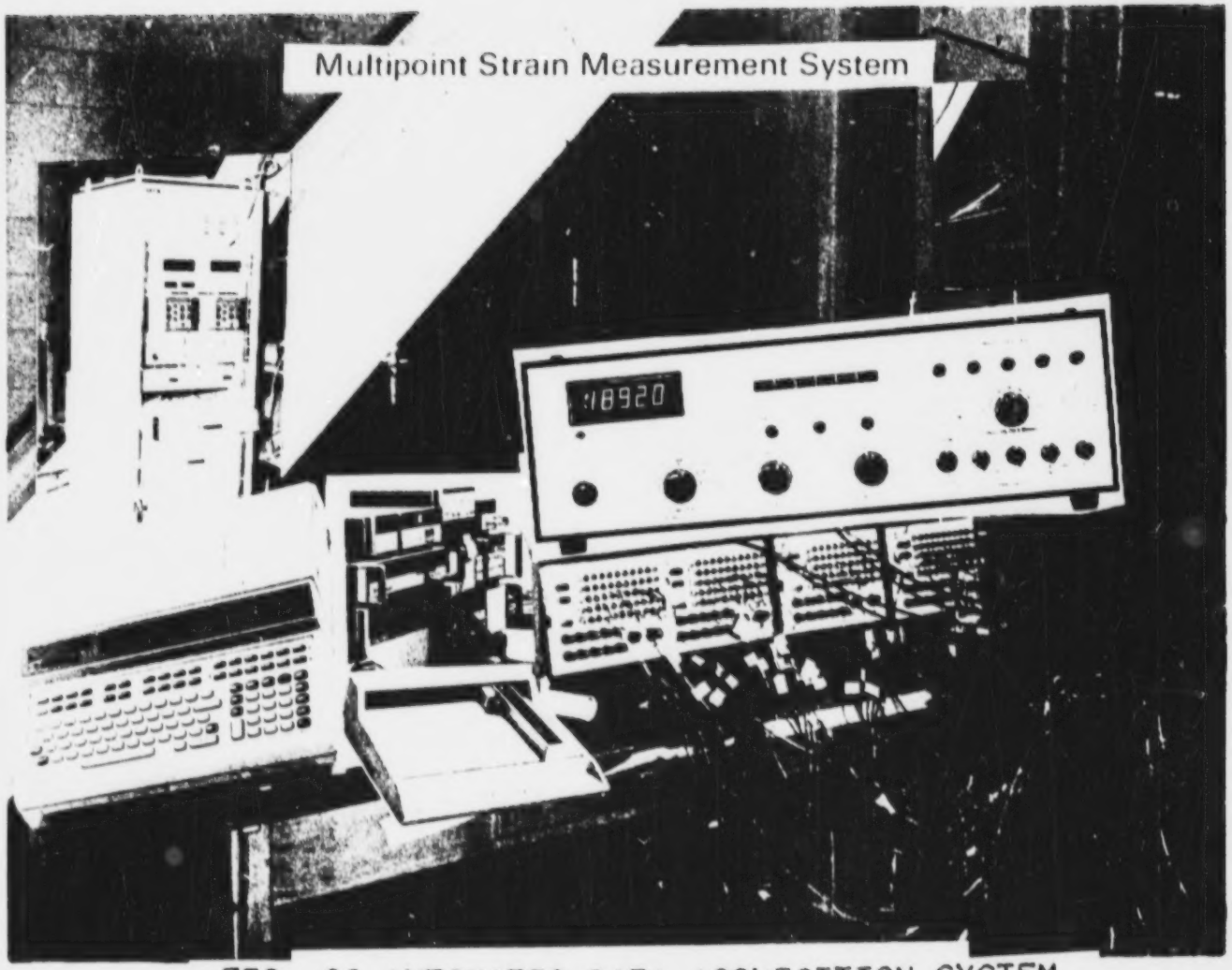

FIG. 22 AUTOMATIC DATA ACQUISITION SYSTEM

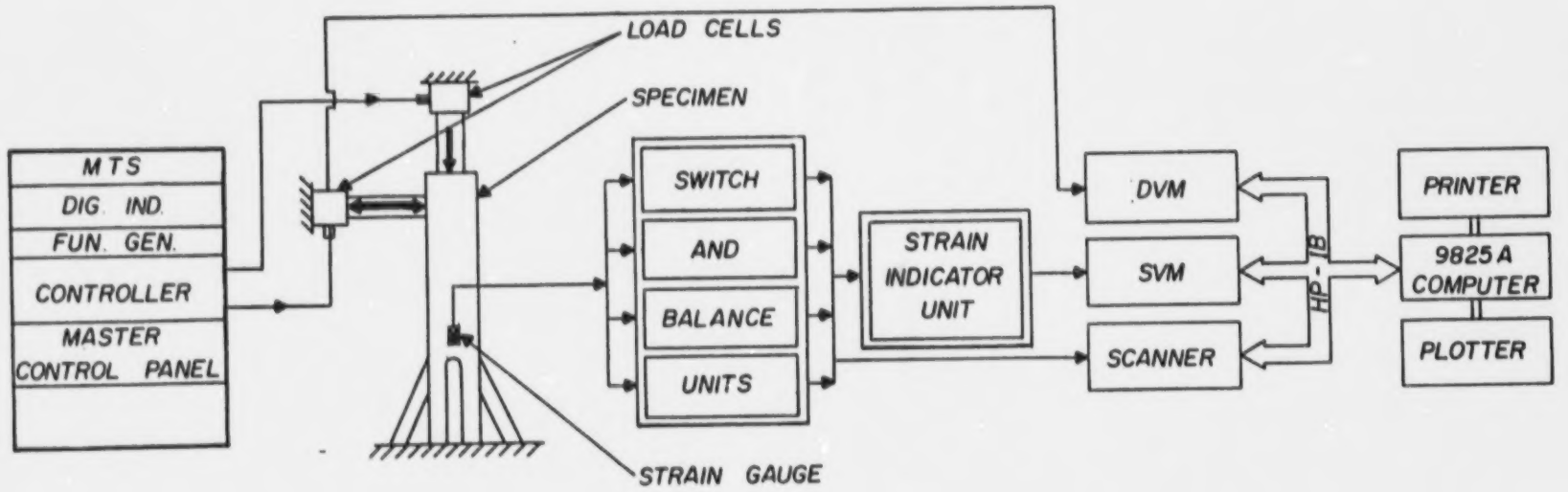

FIG. 23 BLOCK DIAGRAM OF DATA ACQUISITION SYSTEM

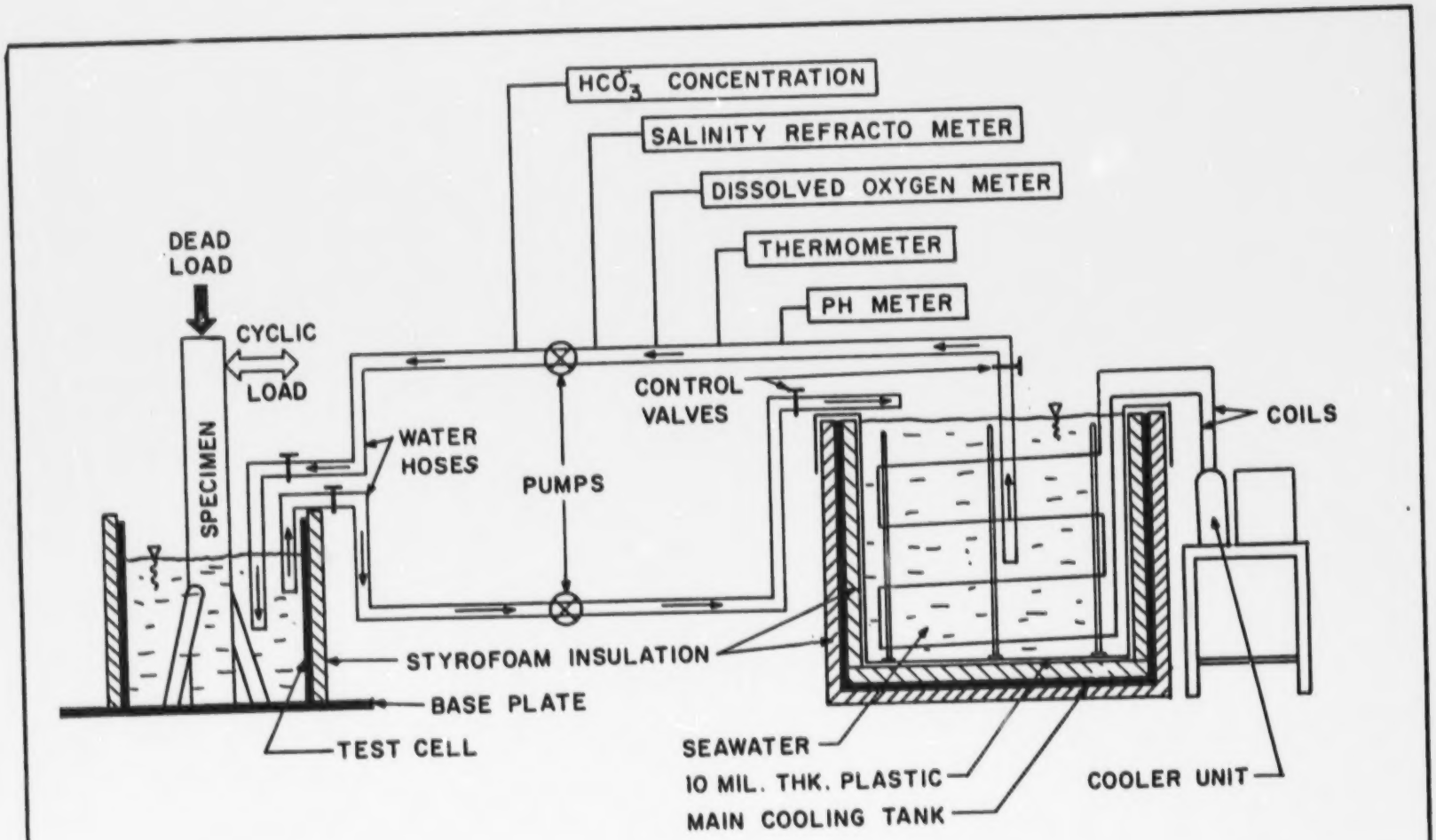

FIG. 24 SCHEMATIC ILLUSTRATION OF SAEWATER COOLING AND CIRCULATION SYSTEMS

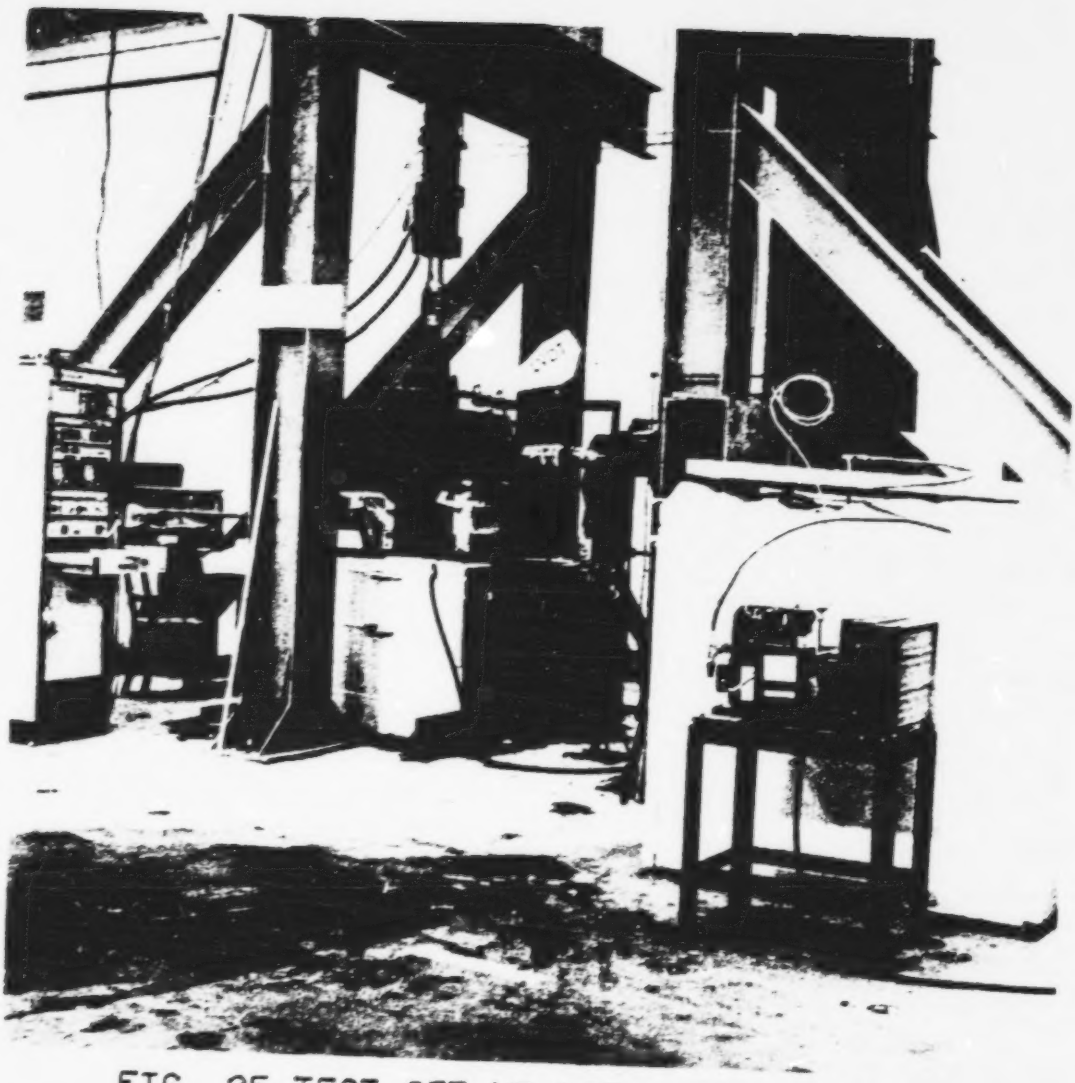

FIG. 25 TEST SET-UP WITH COOLING UNIT

Weld toe grinding extended below the plate surface to remove toe defects

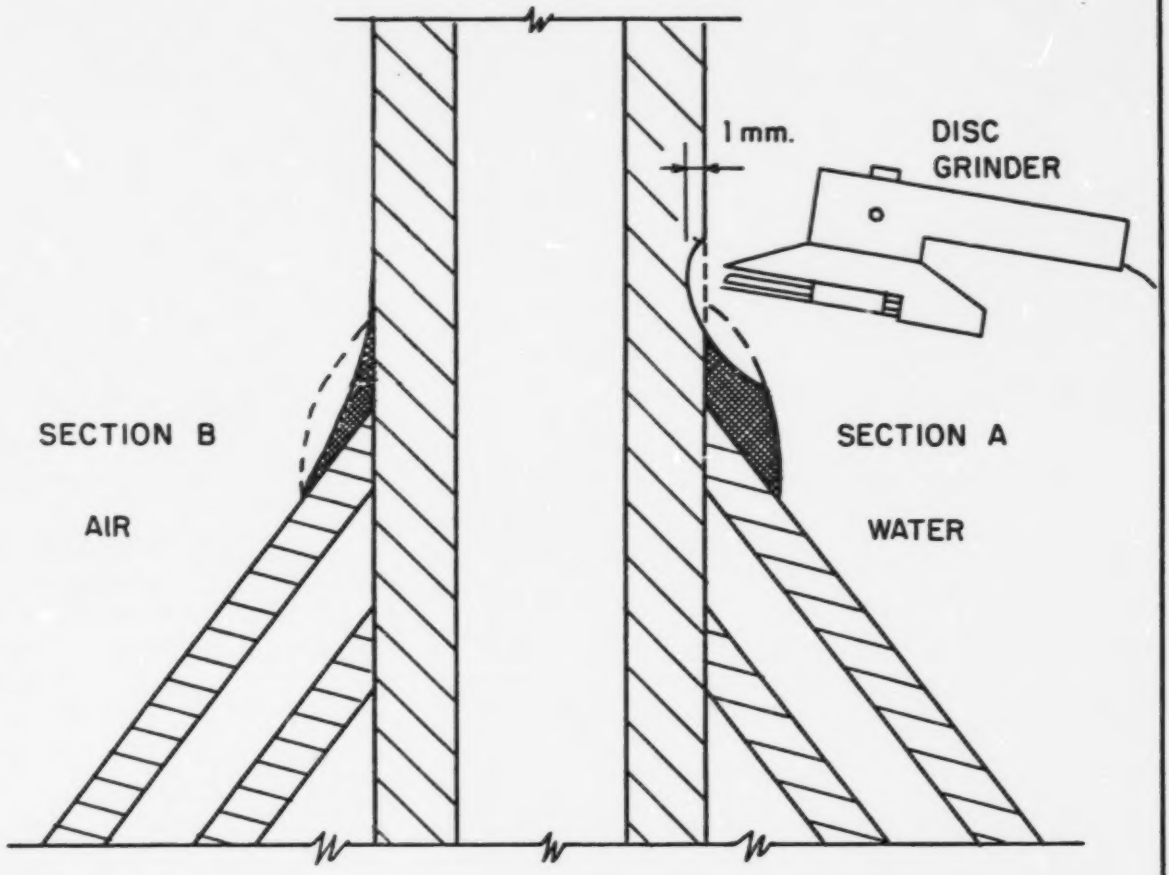

FIG. 26 WELD TOE GRINDING PROFILE

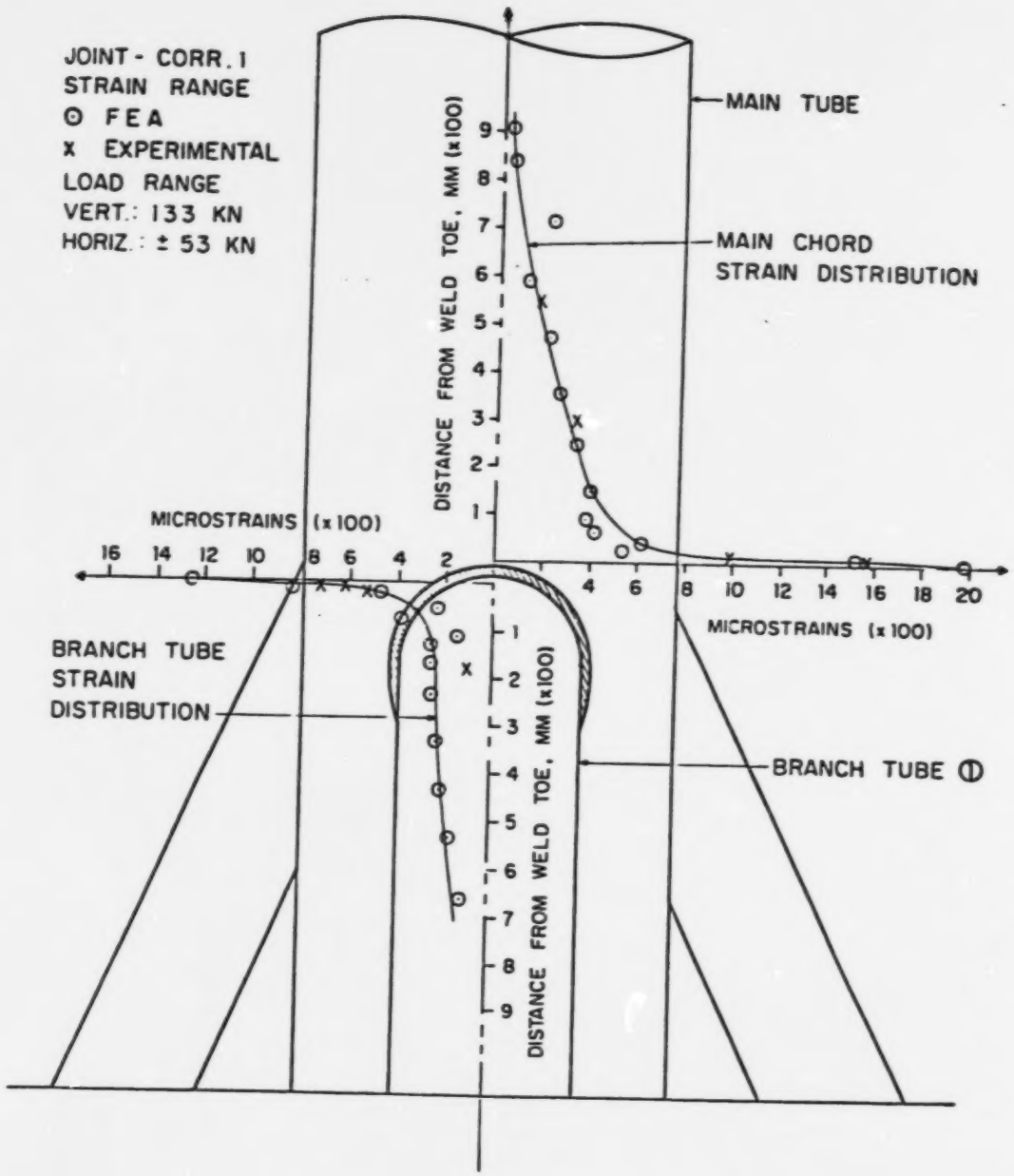

FIG. 27 COMPARISON OF STRAIN DISTRIBUTION: JOINT - CORR. 1

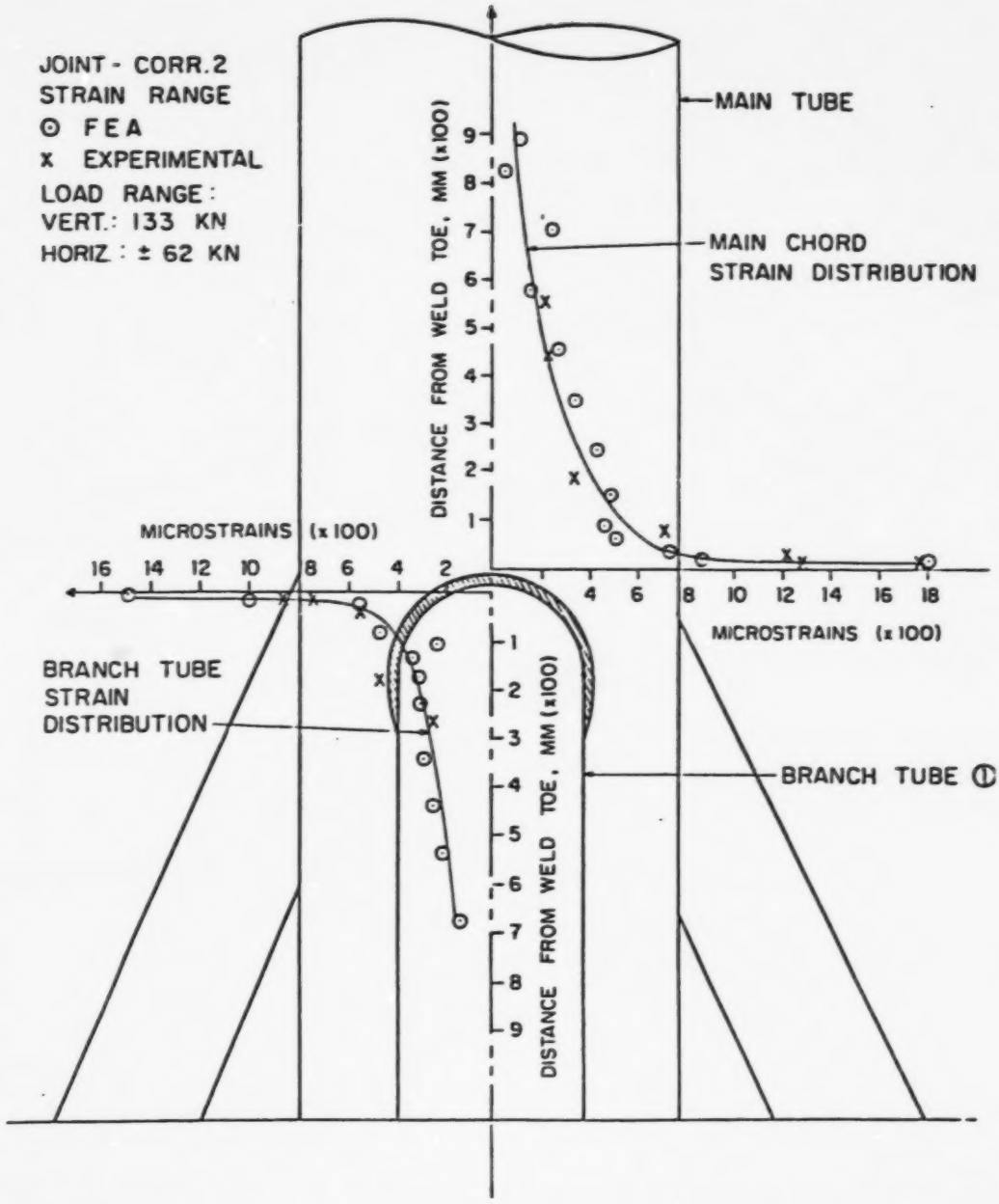

FIG. 28 COMPARISON OF STRAIN DISTRIBUTION: JOINT - CORR.2

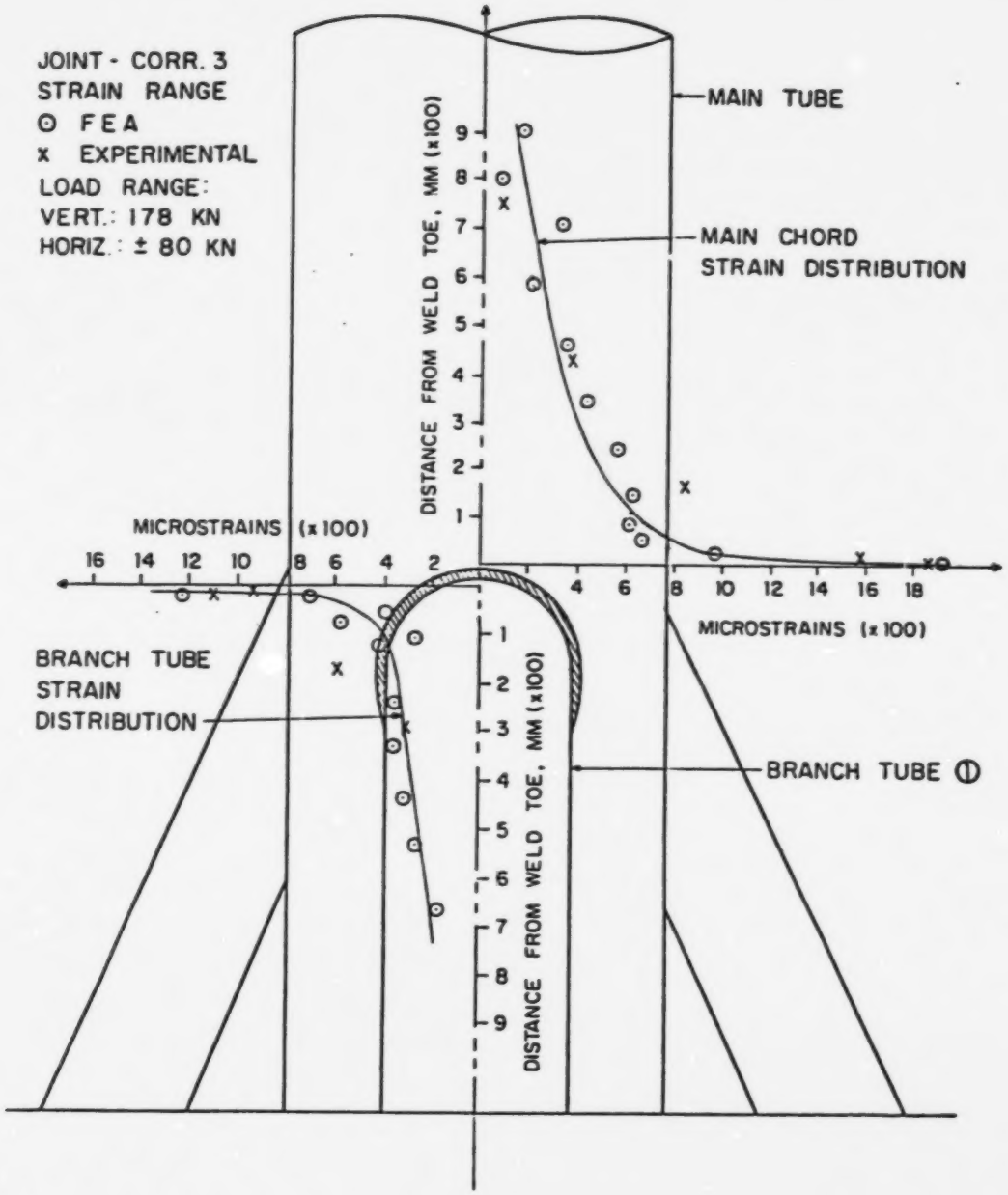

FIG. 29 COMPARISON OF STRAIN DISTRIBUTIONS: JOINT - CORR.3

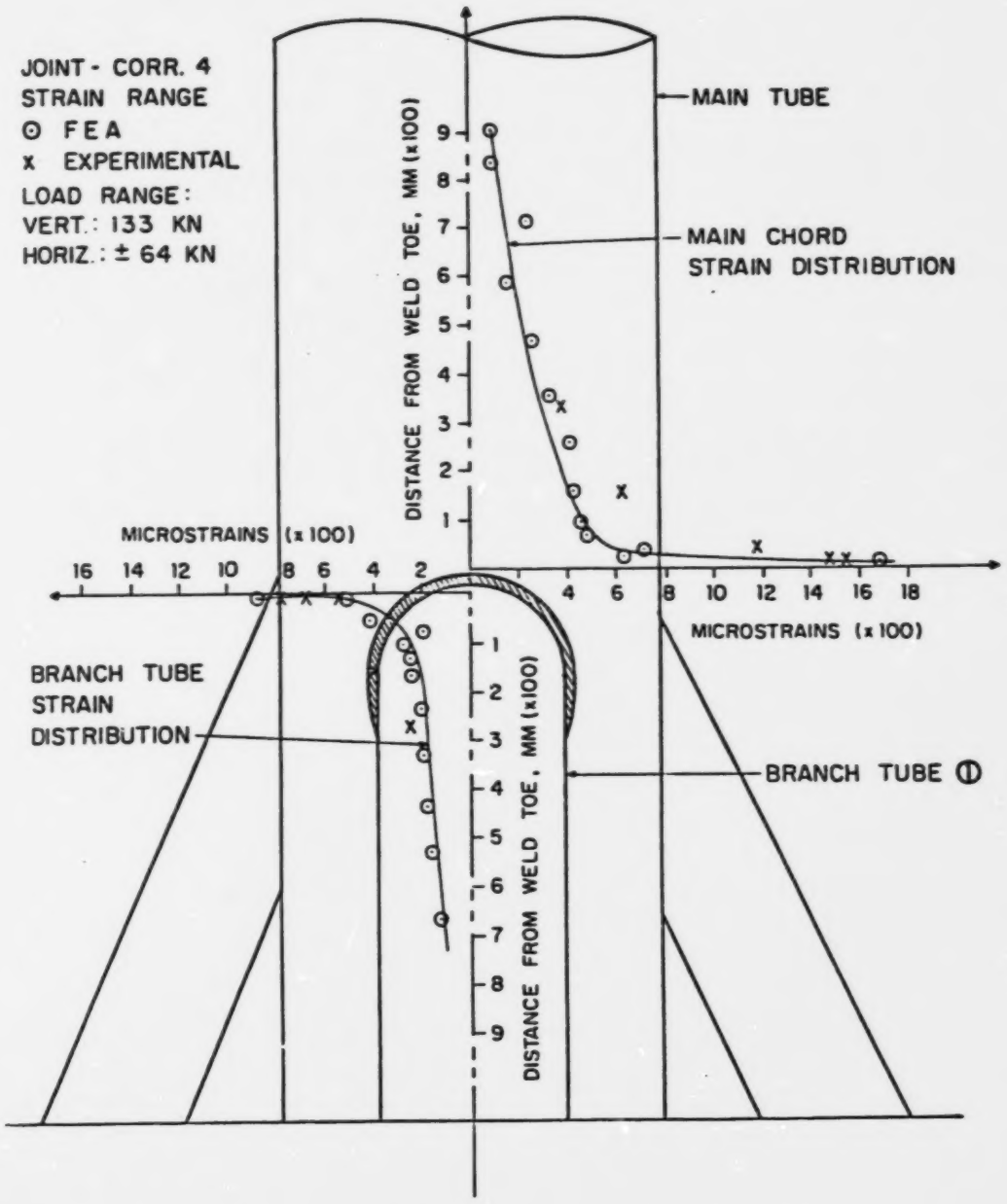

FIG. 30 COMPARISON OF STRAIN DISTRIBUTIONS: JOINT - CORR.4

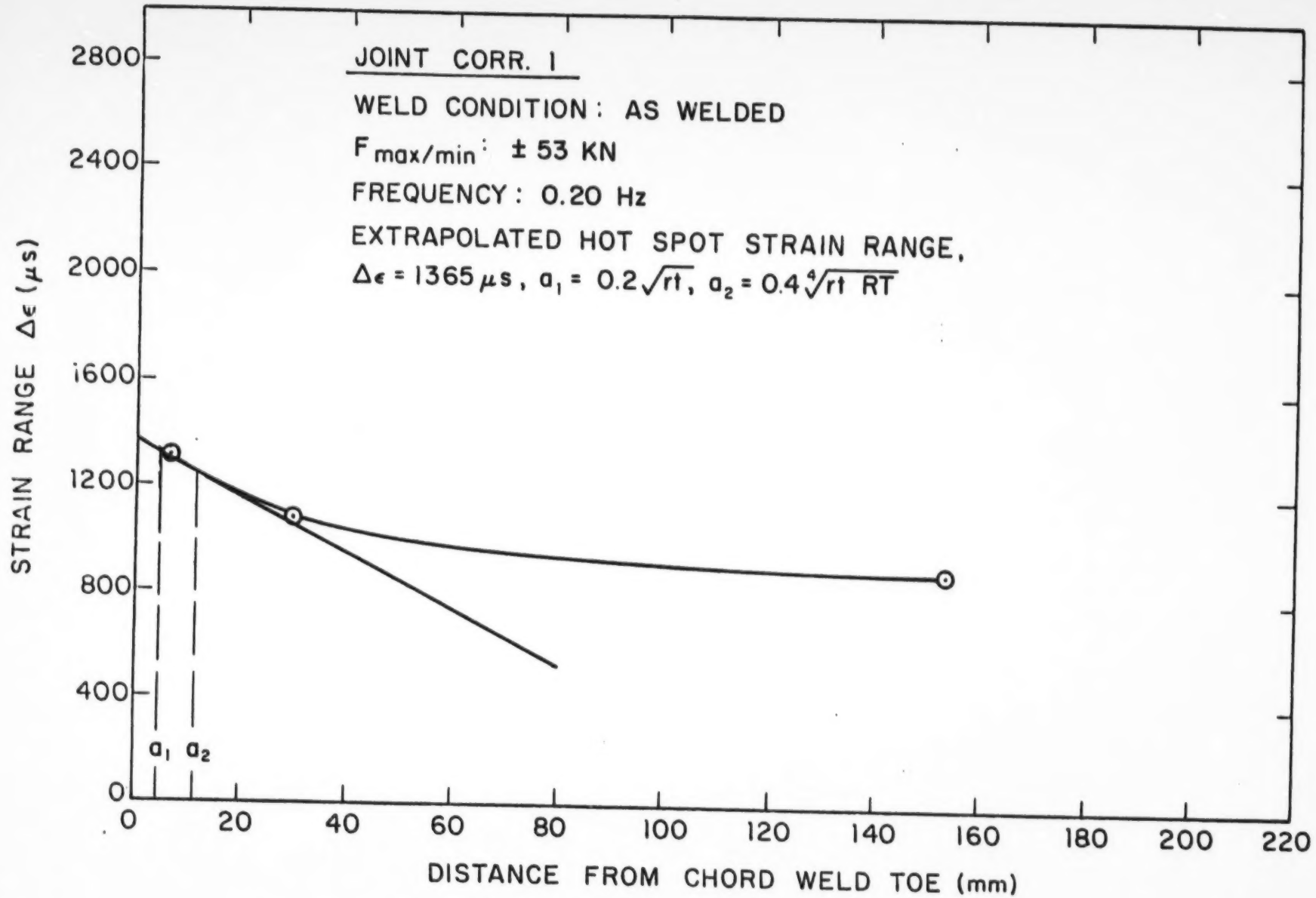

FIG. 31 STRAIN DISTRIBUTION NEAR WELD TOE: JOINT - CORR. 1

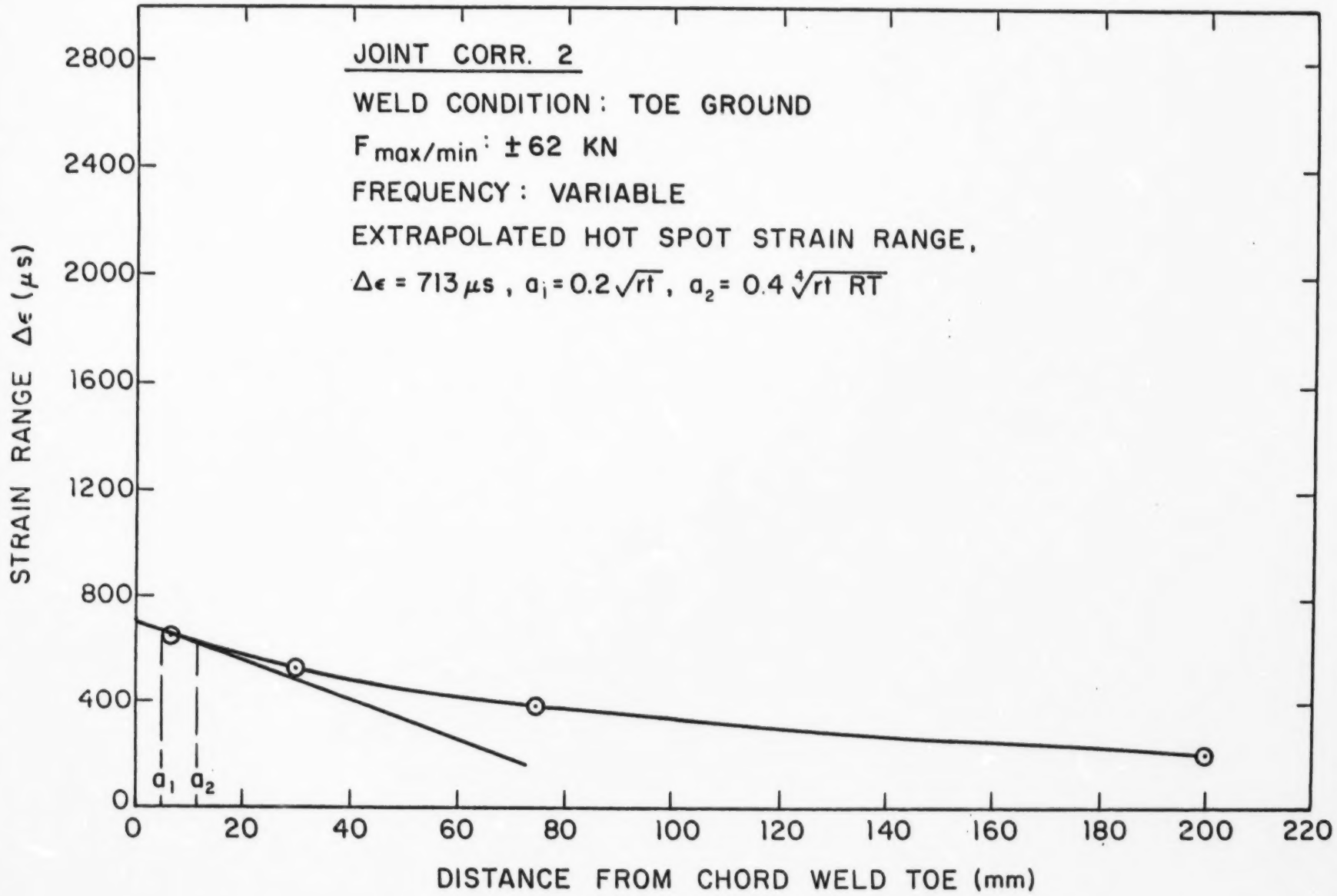

FIG. 32 STRAIN DISTRIBUTION NEAR WELD TOE, JOINT - CORR.2

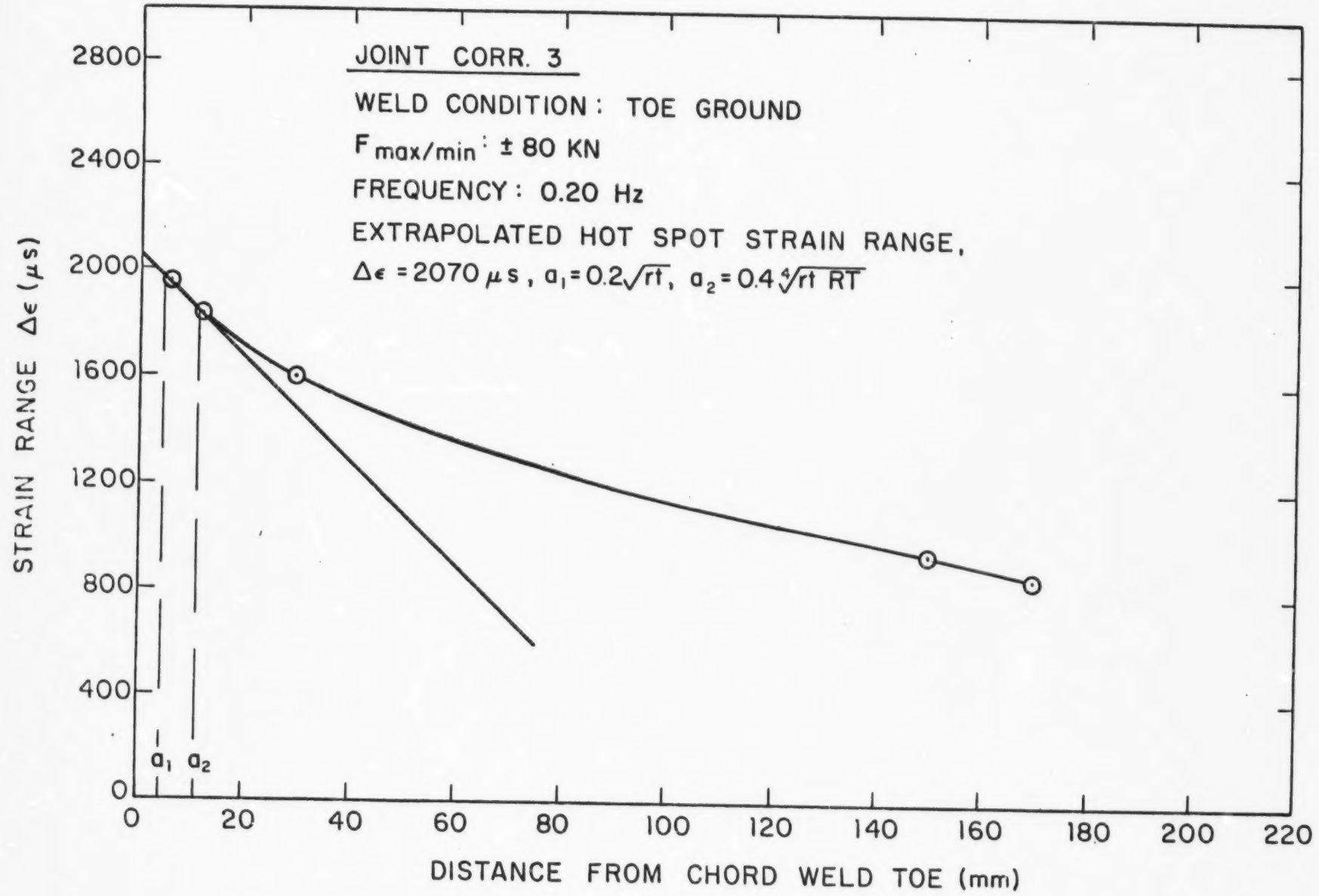

FIG. 33 STRAIN DISTRIBUTION NEAR WELD TOE: JOINT - CORR.3

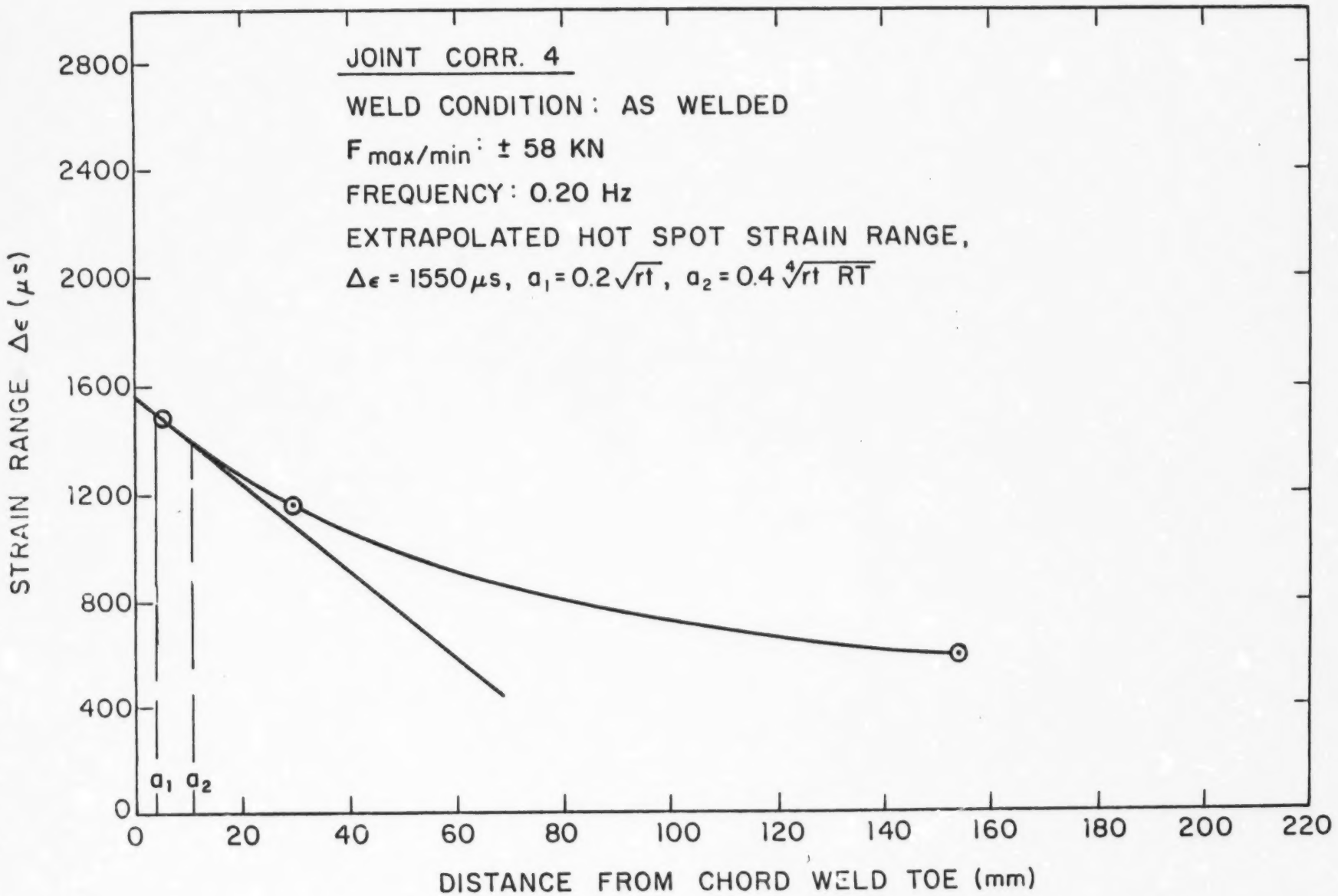

FIG. 34 STRAIN DISTRIBUTION NEAR WELD TOE: JOINT - CORR.4

JOINT CORR. 1

• POINT OF CRACK INITIATION

– N x 10^4 CYCLES

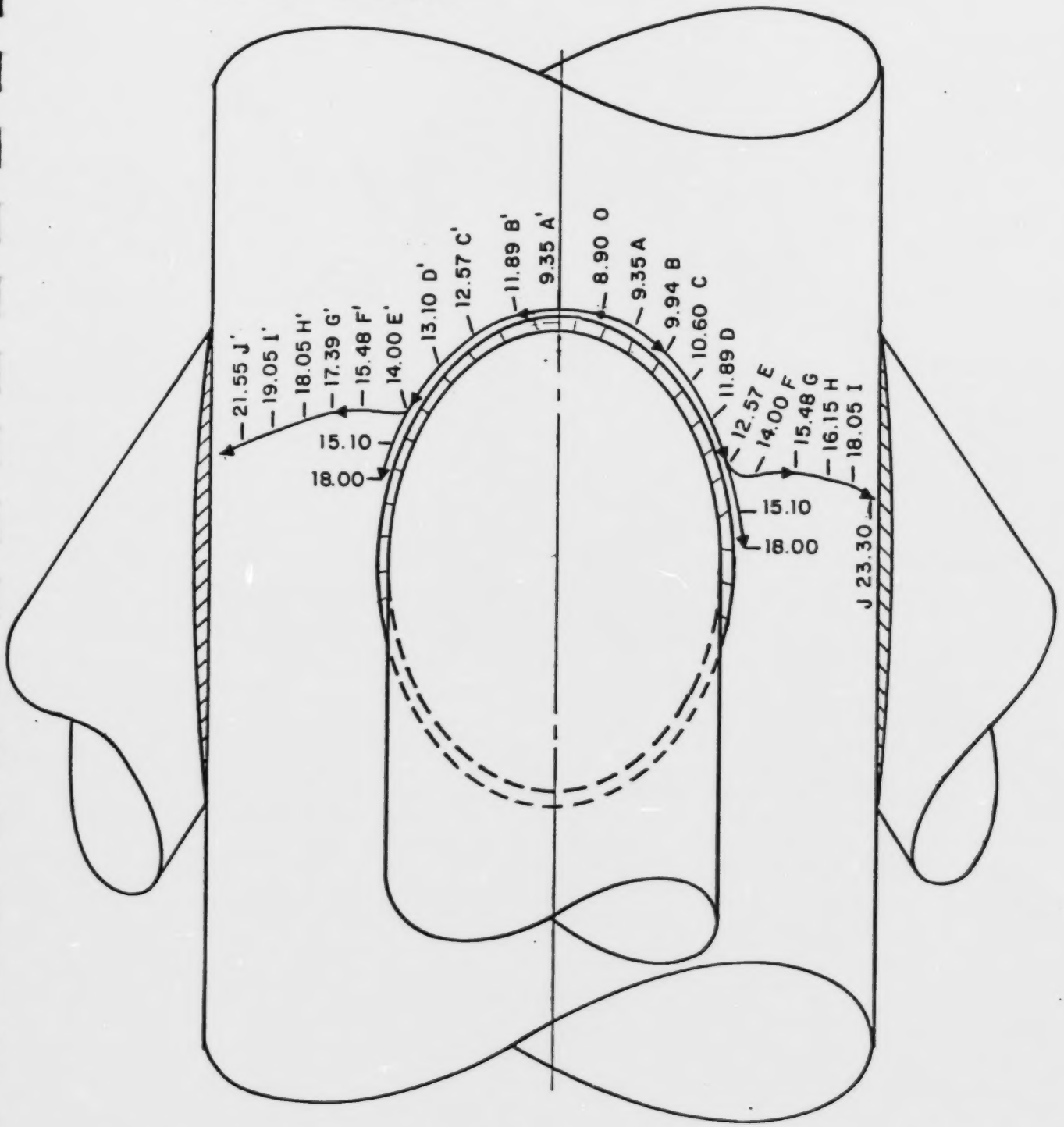

FIG. 35 SURFACE CRACK GROWTH DEVELOPMENT: JOINT – CORR. 1

JOINT CORR. 2

• POINT OF CRACK INITIATION

– N x 10^4 CYCLES

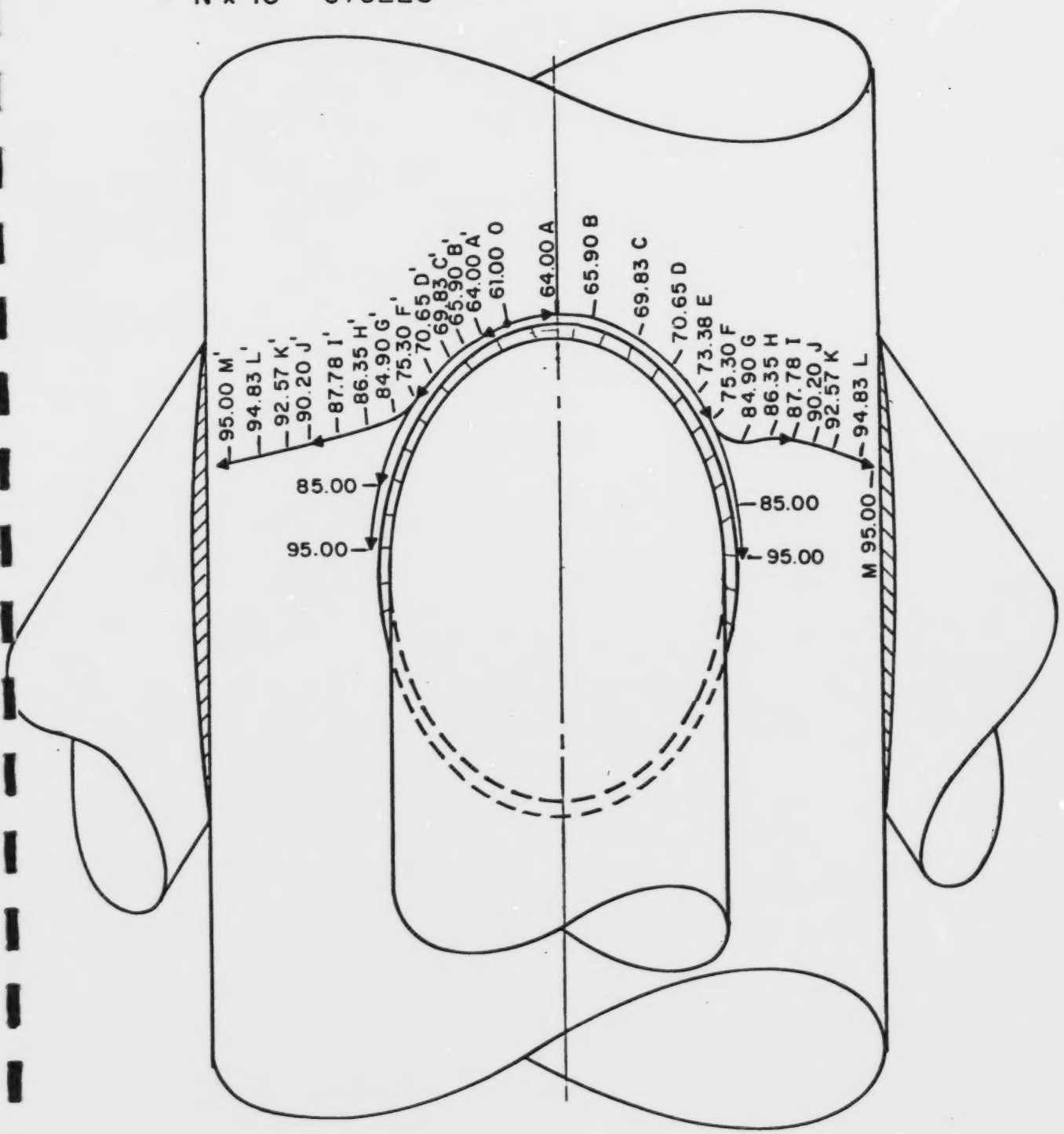

FIG. 36 SURFACE CRACK GROWTH DEVELOPMENT: JOINT – CORR.2

JOINT CORR. 3

• POINT OF CRACK INITIATION

– N x 10^4 CYCLES

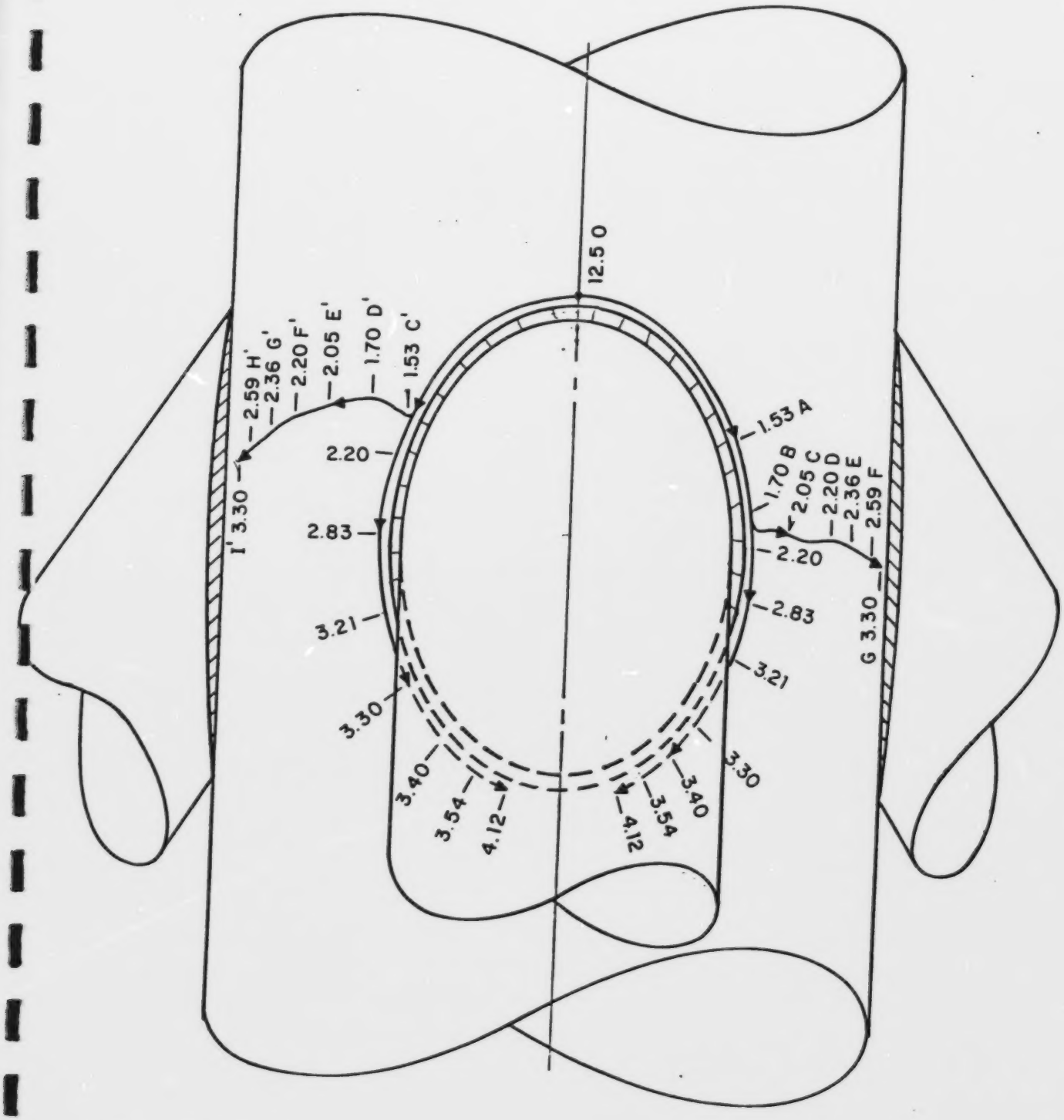

FIG. 37 SURFACE CRACK GROWTH DEVELOPMENT: JOINT – CORR. 3

JOINT CORR 4

• POINT OF CRACK INITIATION

– N x 10^4 CYCLES

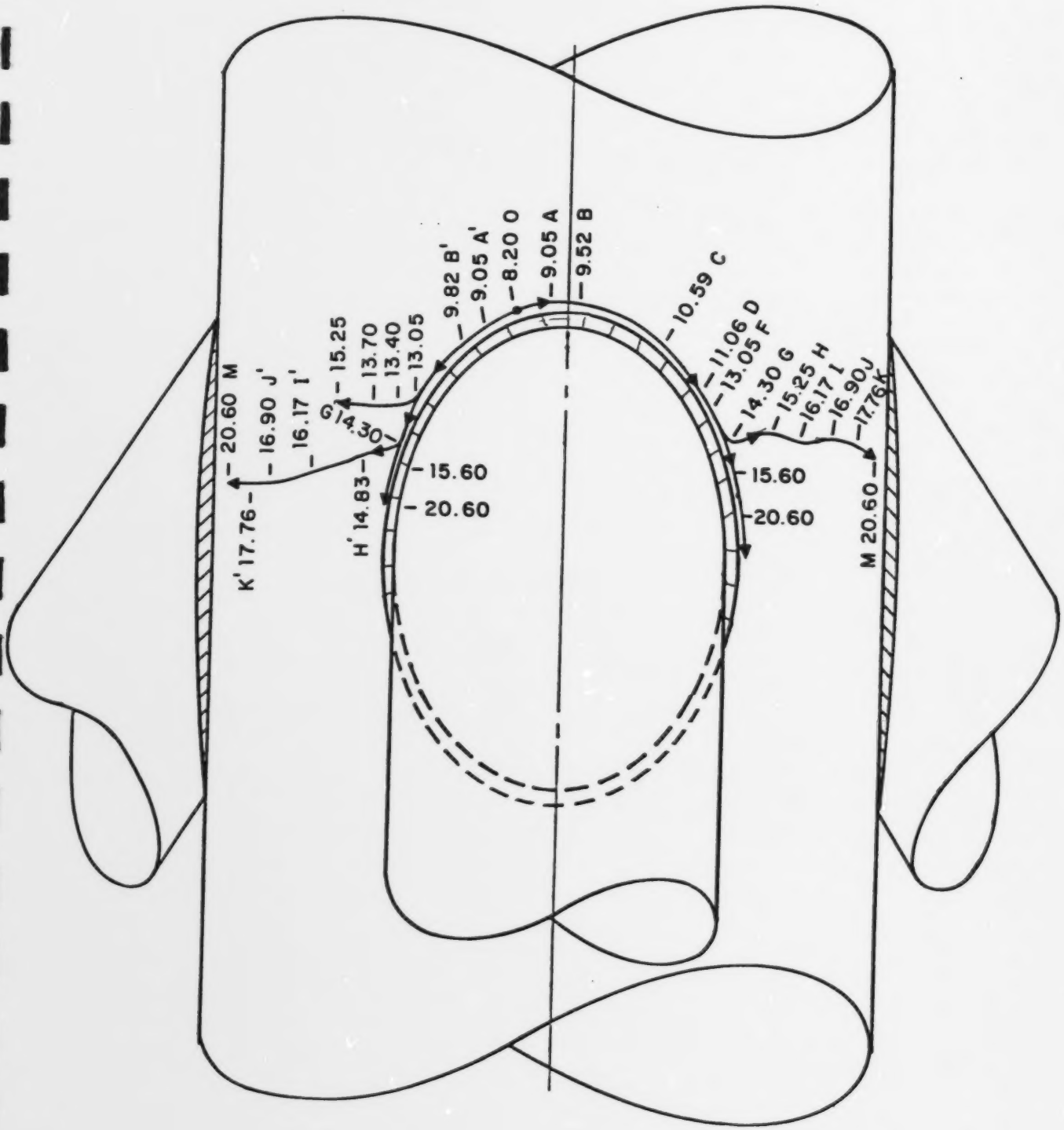

FIG. 38 SURFACE CRACK GROWTH DEVELOPMENT: JOINT – CORR.4

JOINT DRY 1

• POINT OF CRACK INITIATION

– N x 10^4 CYCLES

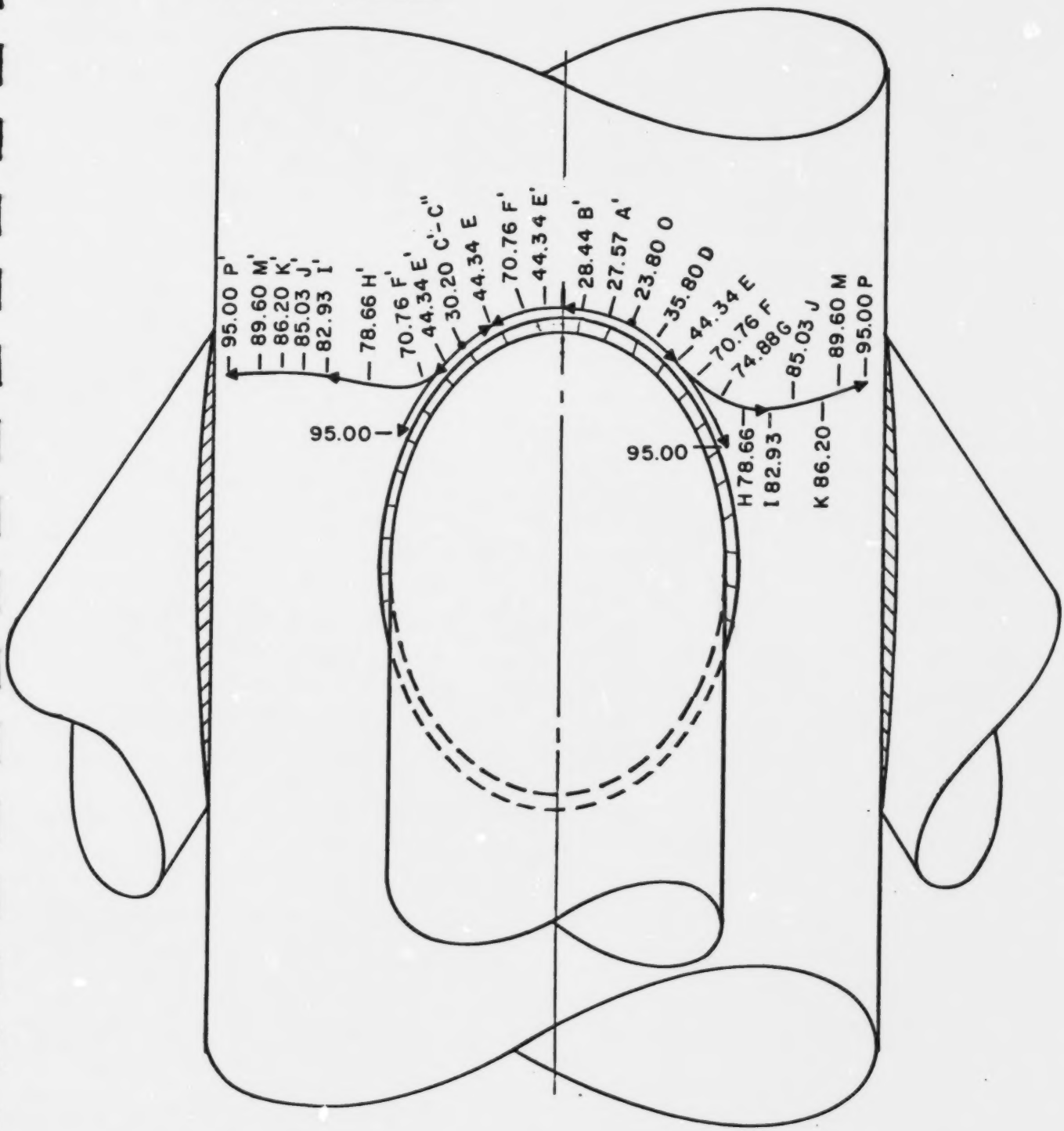

FIG. 39 SURFACE CRACK GROWTH DEVELOPMENT: JOINT – DRY 1

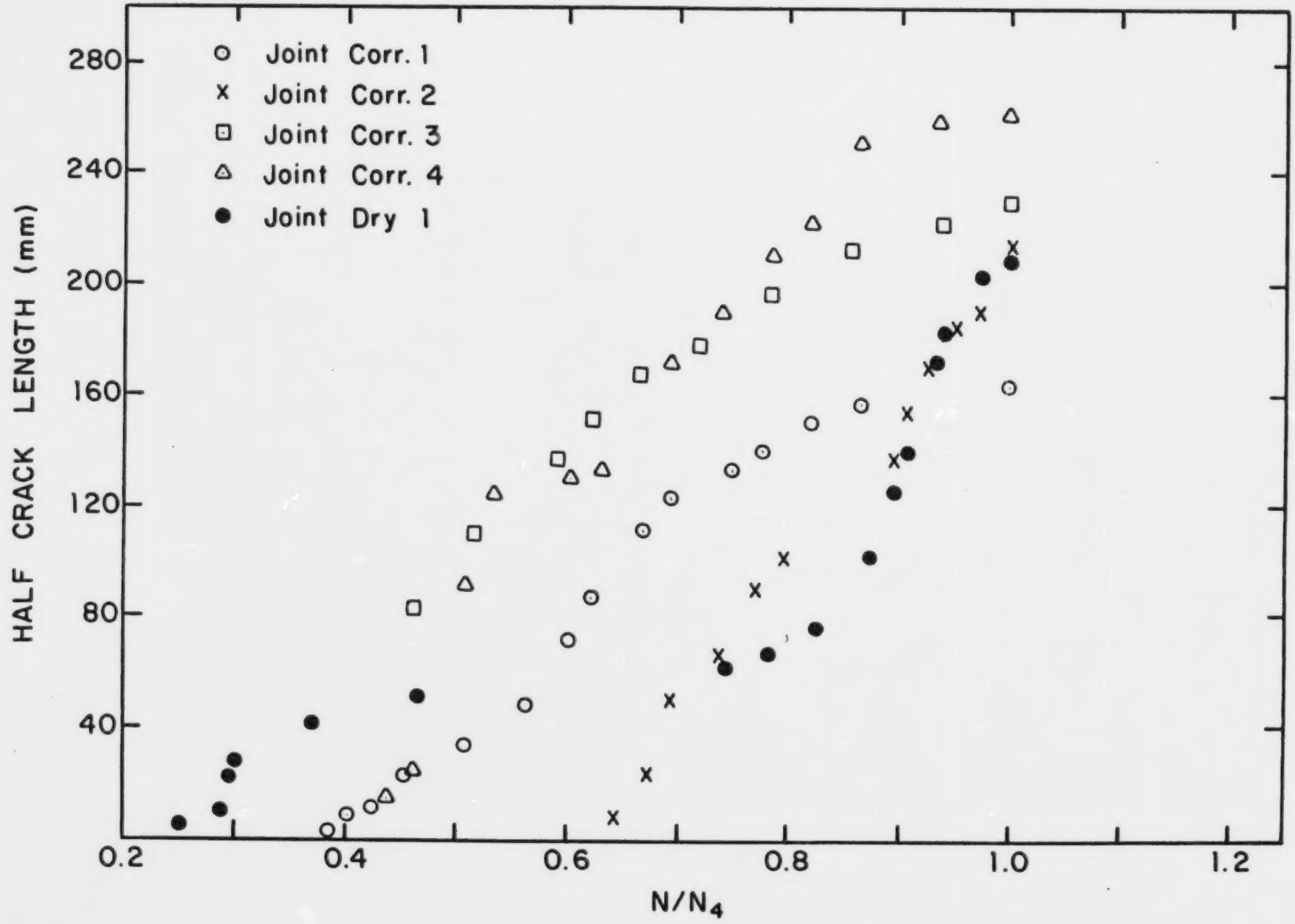

FIG. 40 CRACK GROWTH CHARACTERISTICS OF JOINTS

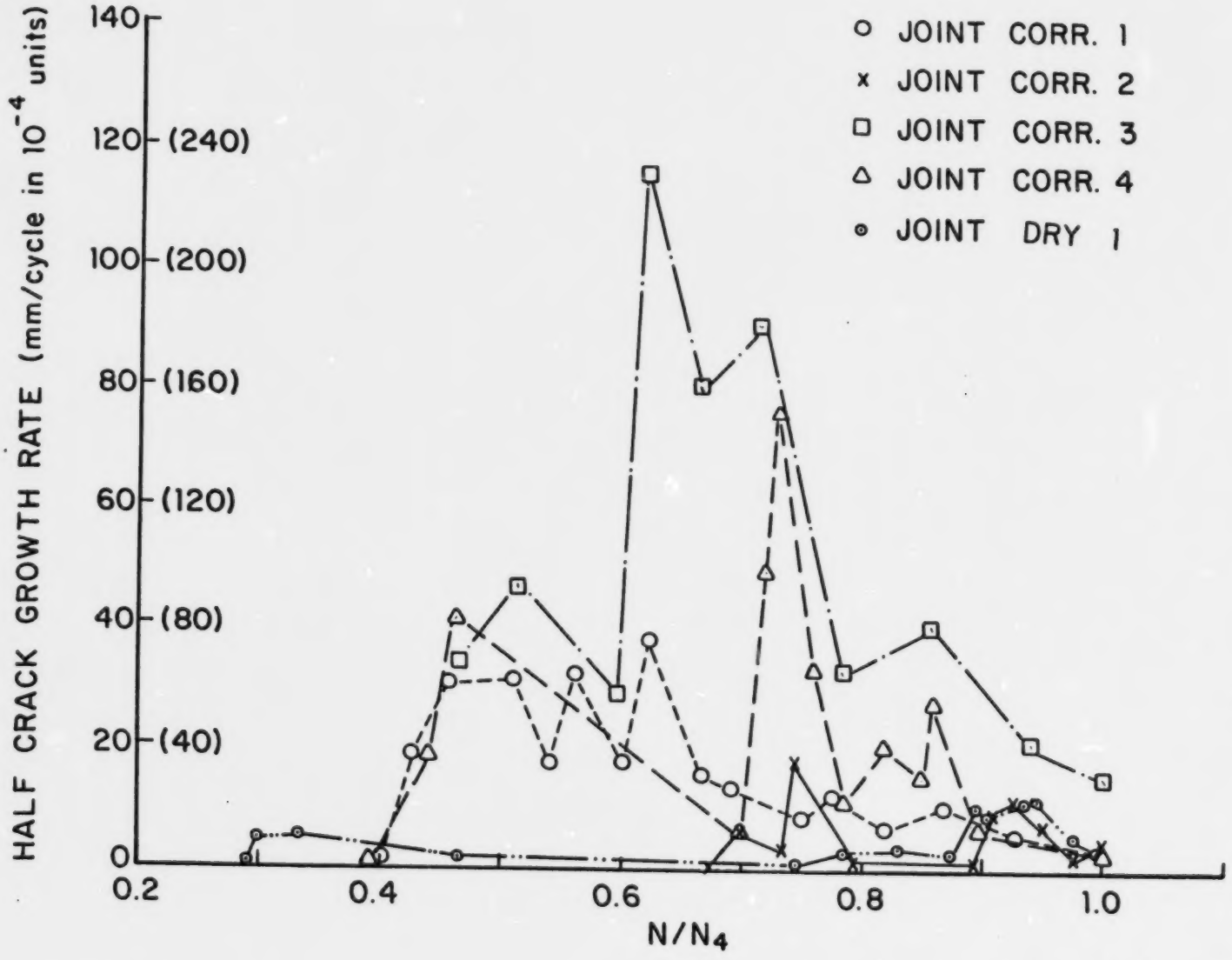

FIG. 41 CRACK GROWTH RATE

FIG. 42 a) PHOTOGRAPH OF JOINT - CORR.1 (HARMONIC LOAD)

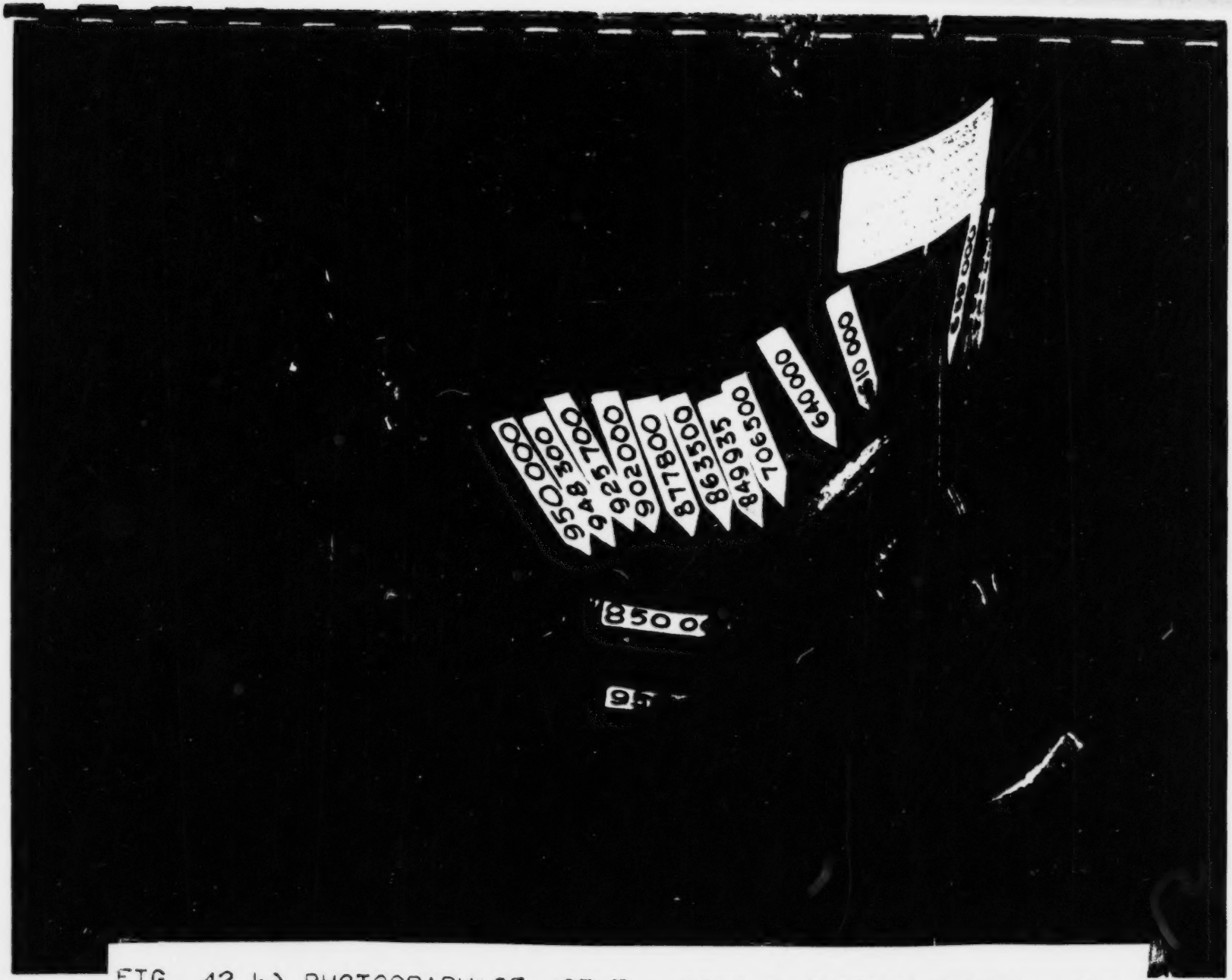

FIG. 42 b) PHOTOGRAPH OF JOINT - CORR.2 (PSEUDO-RANDOM LOAD)

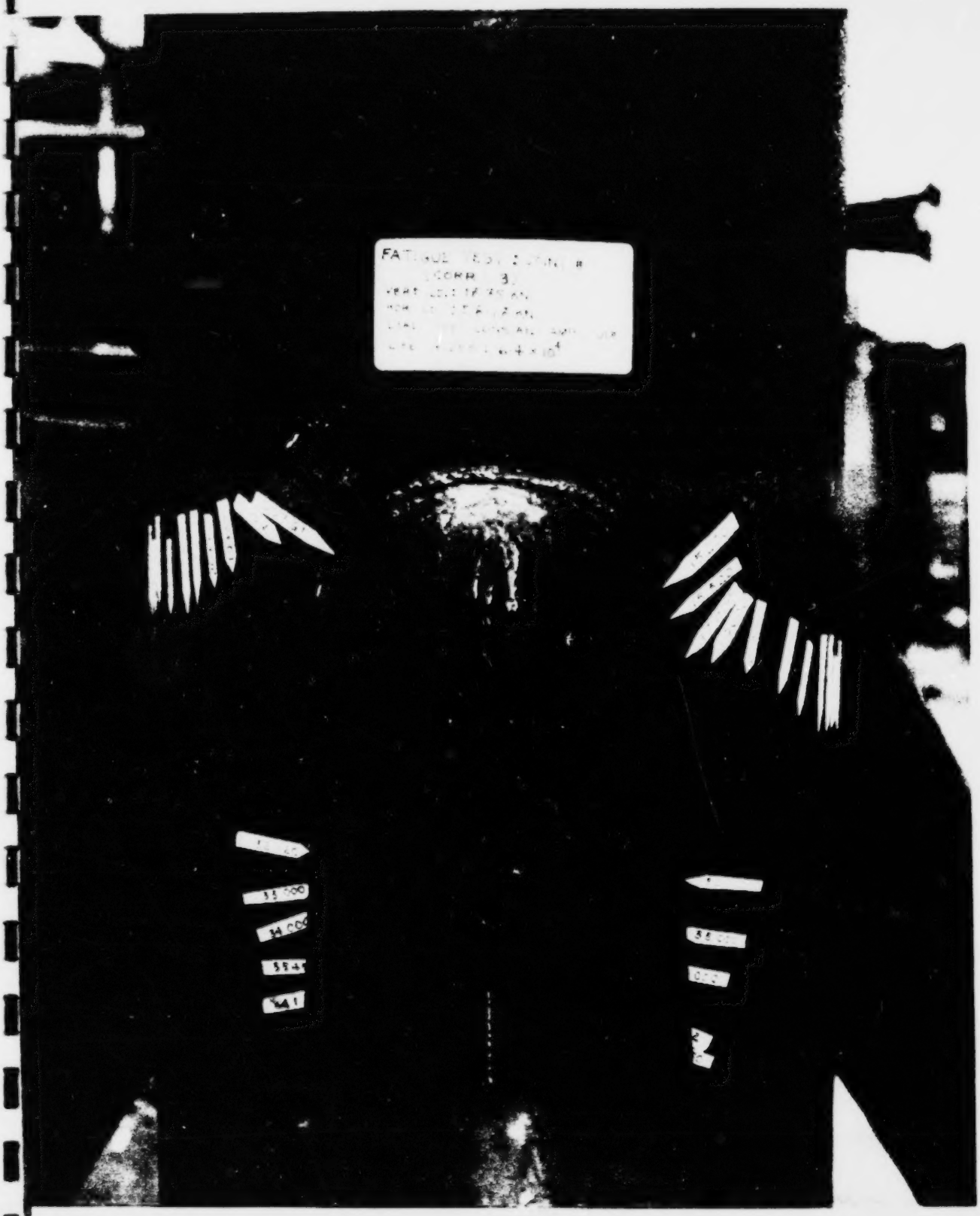

FIG. 42 c) PHOTOGRAPH OF JOINT - CORR.3 (HARMONIC LOAD)

FIG. 42 d) PHOTOGRAPH OF JOINT - CORR.4 (HARMONIC LOAD)

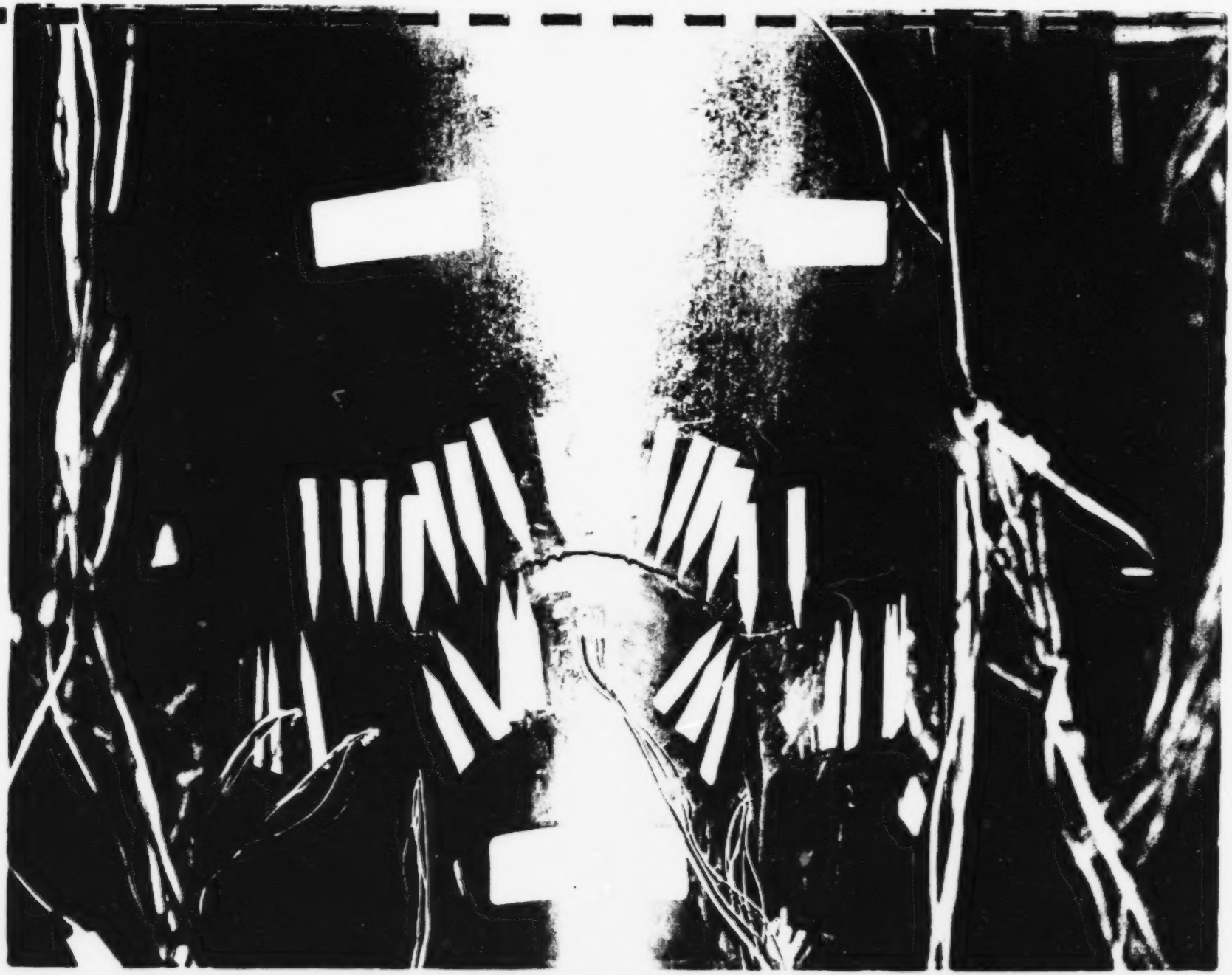

FIG. 43 PHOTOGRAPH OF JOINT - DRY 1 (PSEUDO-RANDOM LOAD)

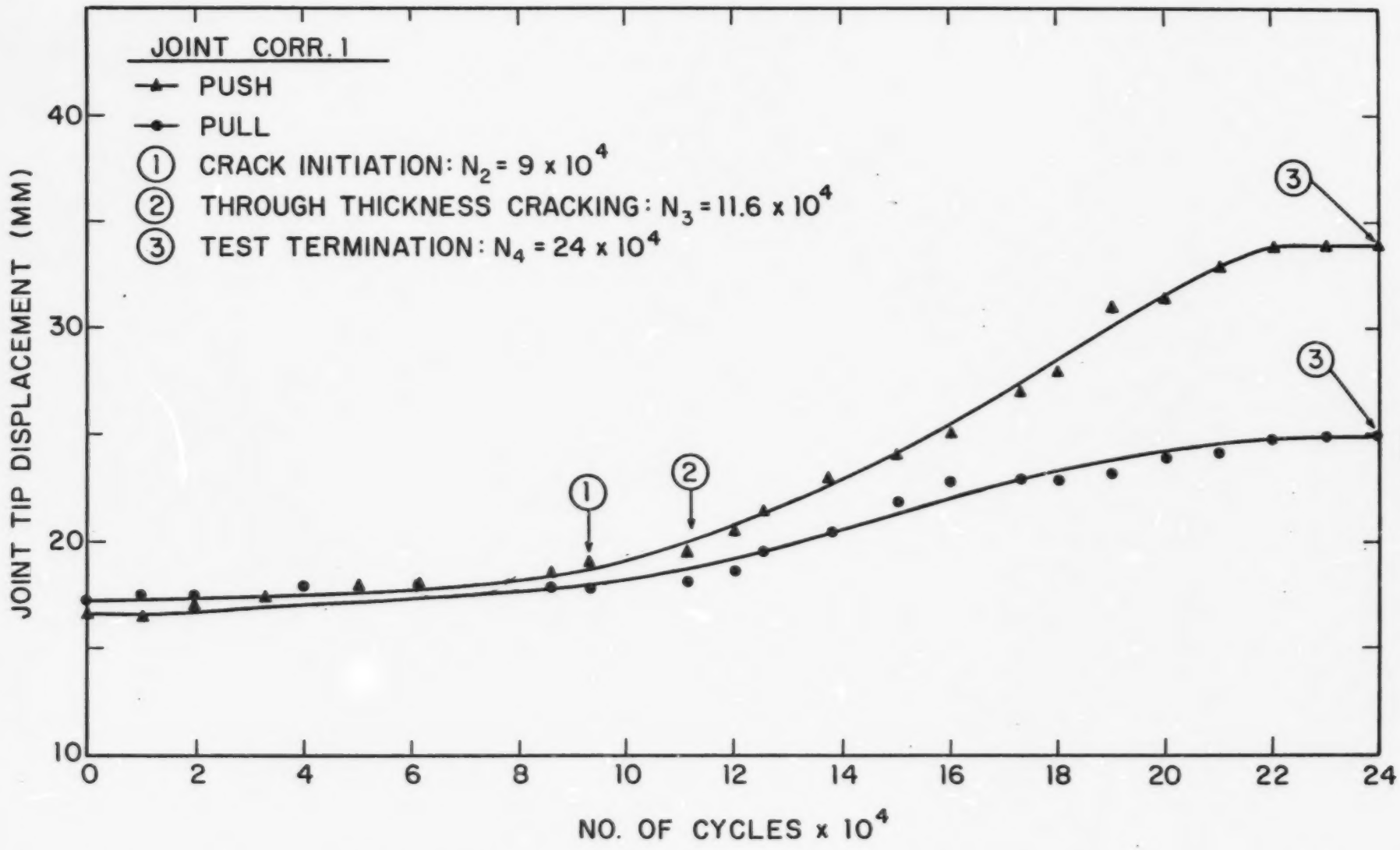

FIG. 44 SPECIMEN TIP DISPLACEMENT: JOINT - CORR. 1

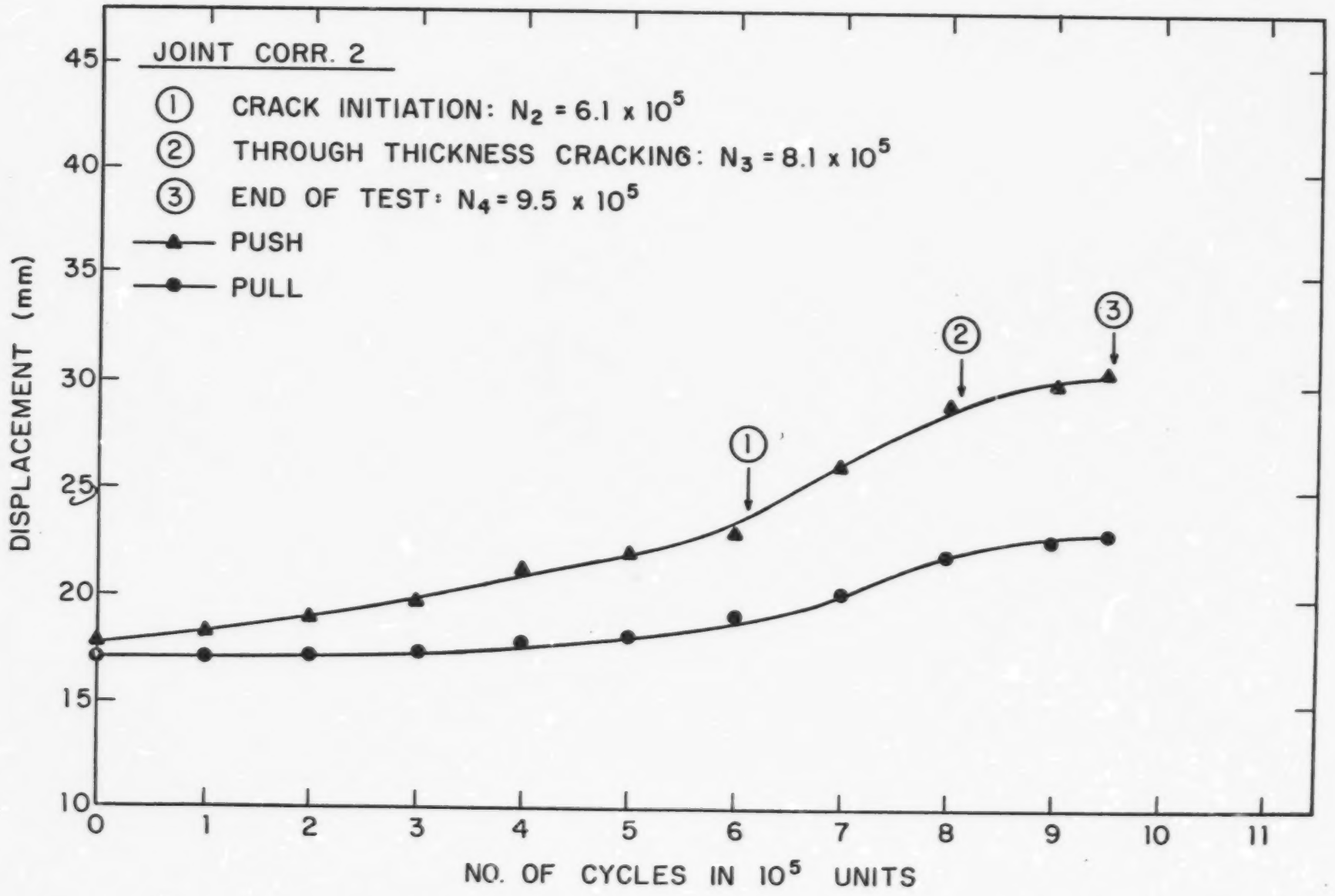

FIG. 45 SPECIMEN TIP DISPLACEMENT: JOINT - CORR.2

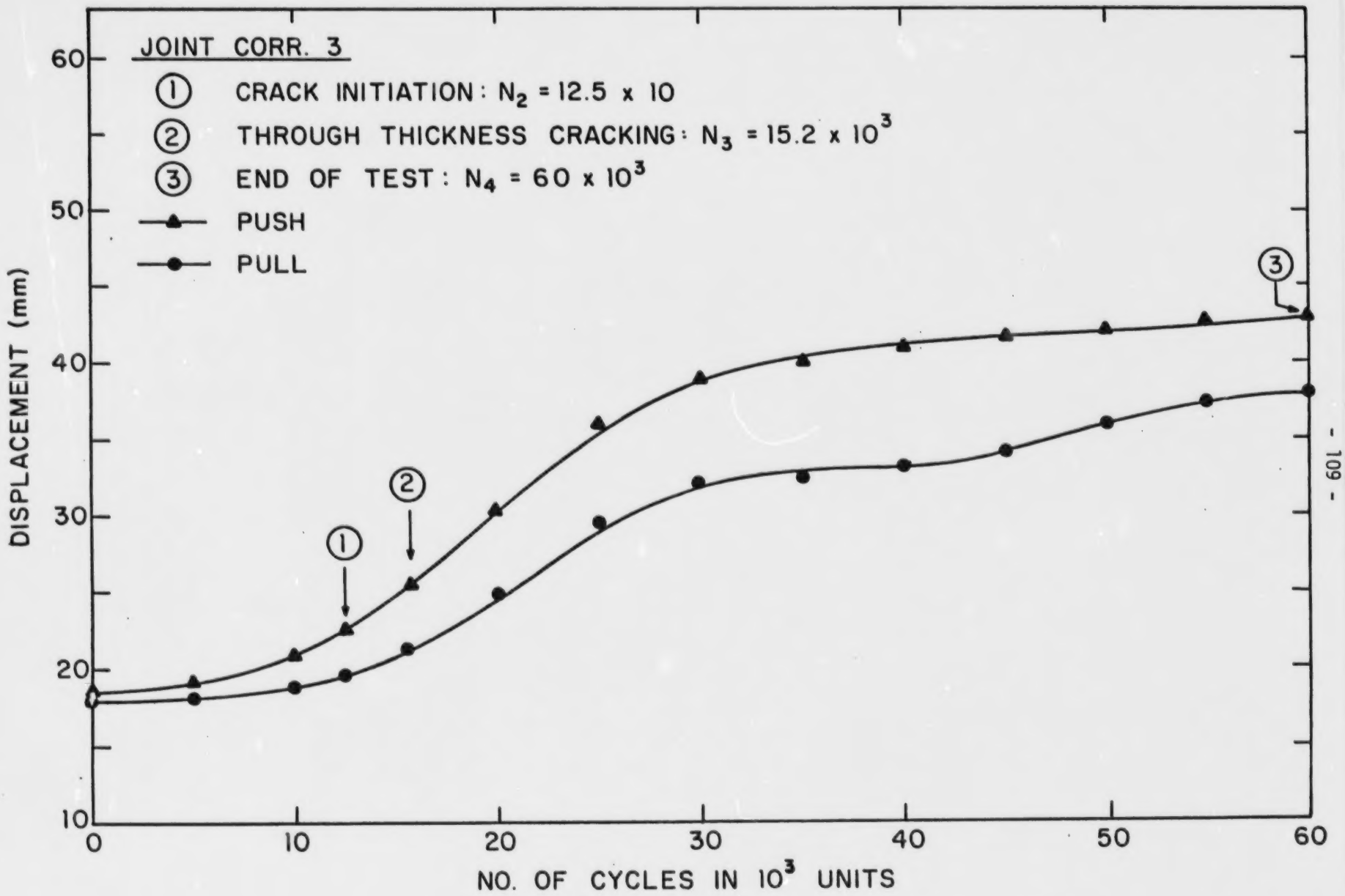

FIG. 46 SPECIMEN TIP DISPLACEMENT: JOINT – CORR.3

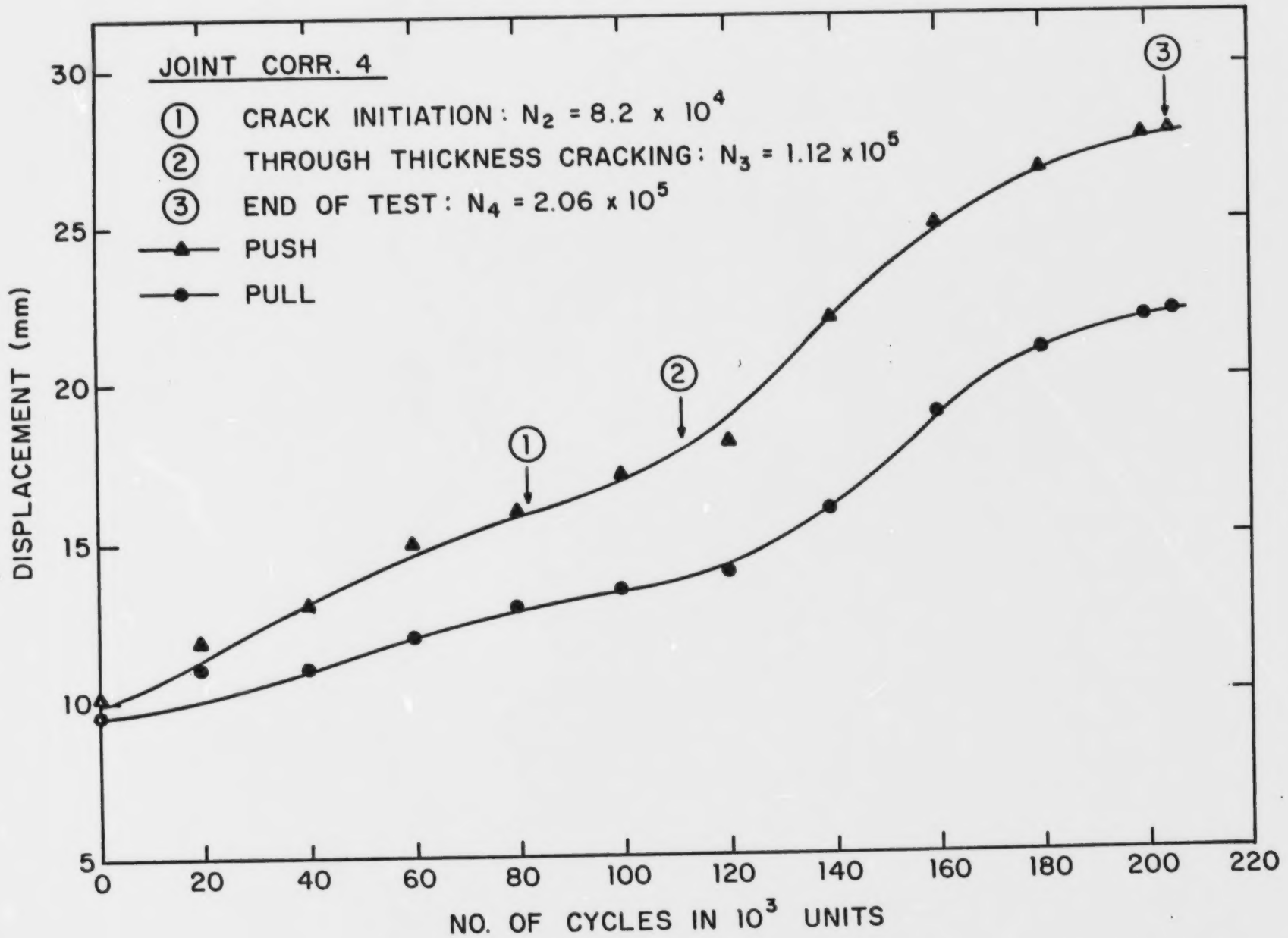

FIG. 47 SPECIMEN TIP DISPLACEMENT: JOINT – CORR. 4

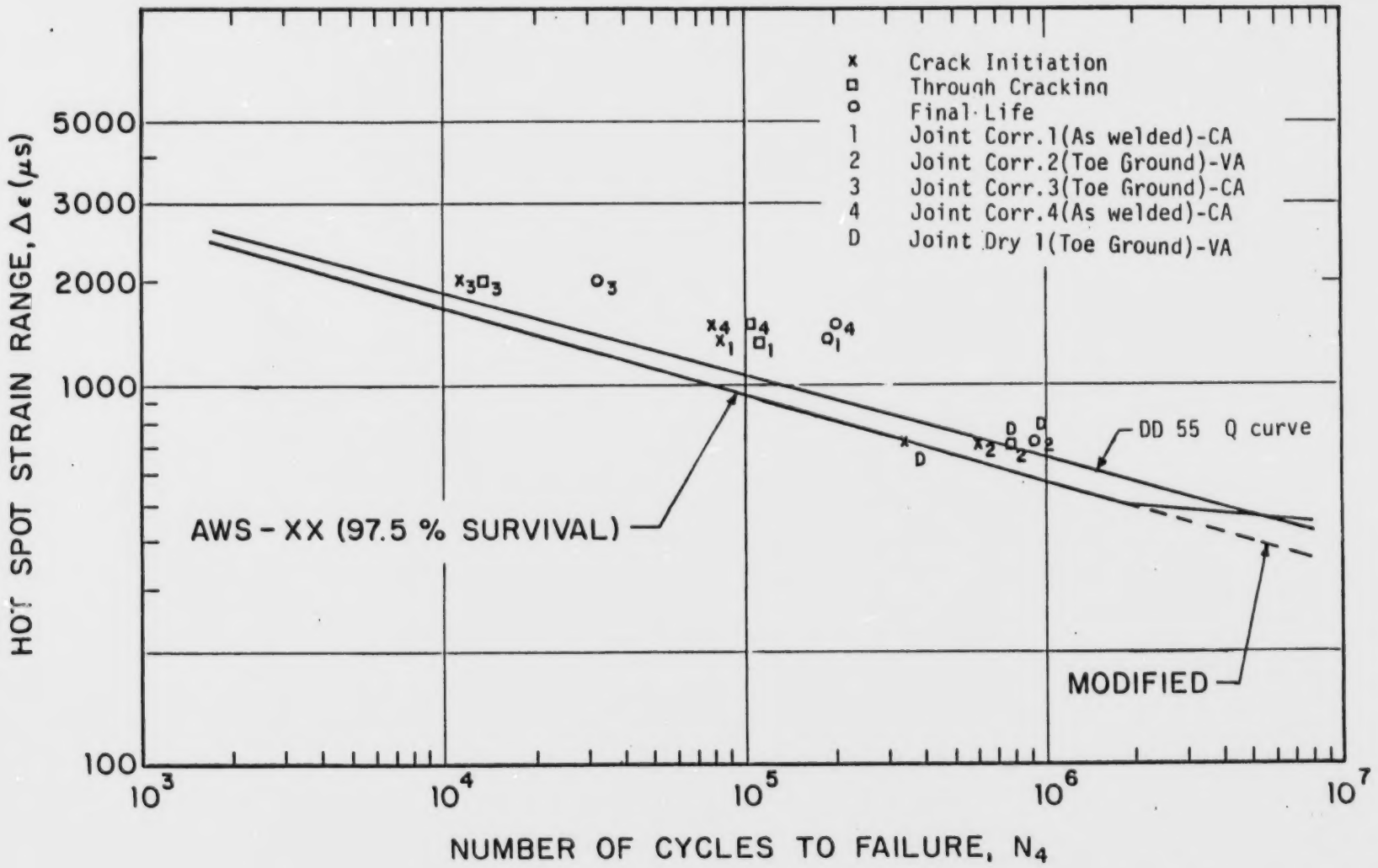

FIG. 48 COMPARISON OF FATIGUE TEST RESULTS

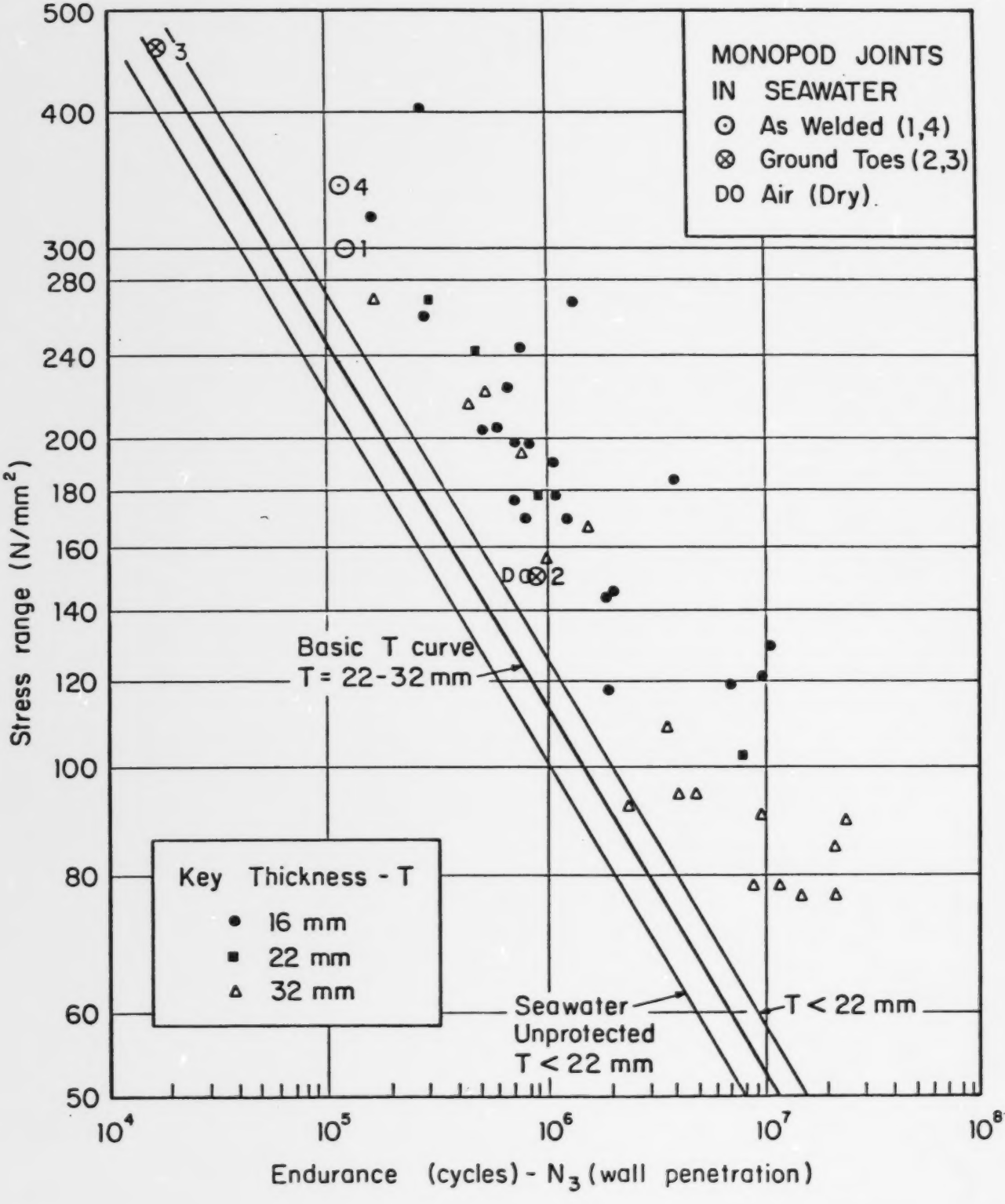

FIG. 49 BASIC S - N CURVES FOR TUBULAR JOINTS

APPENDIX-A

A. MEASUREMENT OF ENVIRONMENTAL PARAMETERS

A.1 Salinity

The resistivity of the seawater changes with the salinity, thereby changing its electrical resistance, which is one of the major factors affecting the rate of corrosion. At 0°C the salinity of seawater is 35% . Salinity is expressed as the amount of solid material in grams contained in one kilogram of seawater when all the carbonate has been converted to oxide, all the bromine and iodine replaced by chlorine, and all the organic material is oxidized [50]. The salinity is related to chlorinity as

$$S\% = 1.80655 \times \text{chlorinity} \qquad \text{(A1)}$$

In the laboratory, the salinity was measured using a Salinity Refractometer. The refractometer is a unique hermetically-sealed hollow-prism, filled with a stable liquid, changes index with temperature to compensate instantly and automatically for temperature changes of the sample. The scale provides two direct readings, one for refractive index and the other for salinity. The procedure to obtain salinity measurements is as follows [51]:

(1) Hold the instrument in a horizontal position, and swing the coverplate over the body of the instrument.

(2) Pipette, not more than 0.02 ml (one drop) of sample to the measuring prism and close the cover plate over the measuring prism immediately.

(3) Keeping the cover plate in contact with the prism, point the instrument towards illuminating light source while taking readings.

(4) Bring the scale seen in the eyepiece into best focus by rotation of the eyepiece, and note the reading at the point where the dividing line between light and dark crosses, which gives the salinity level of the sample.

A.2 pH Value

pH indicates a measure of acidity and alkalinity of the solution caused by the hydrogen ion concentration. The pH value was measured during testing using a pH meter, adapting the following procedure:

I. 1) Prepare a standard solution having 10^{-2}, 10^{-3}, 10^{-4} M, or 1000, 100 and 10 ppm.

2) Mix 50 ml of 10^{-3} M or 1000 ppm standard solution with 5 ml CO_2 buffer solution.

3) Place the electrode in standard solution and set function switch to REL MV.

4) Adjust calibration control to 0.0.

II.1) Mix 50 ml of 10^{-4} M or 10 ppm standard with 5 ml CO_2 buffer solution.

2) Rinse the electrodes and place in the standard solution and note the reading after stabilizing.

III. Repeat the procedure, II, with 10^{-2} M standard, and read pH of the solution direct from the meter.

A.3 Dissolved Oxygen Content

Variation of oxygen content in seawater gives rise to formation of concentration cells, thereby increasing the rate of corrosion. The limiting current density for the reduction of oxygen can be used to estimate the rate of corrosion given by [52]:

$$i_{cor} = \frac{4FD}{1000t} C_o \qquad (A2)$$

where

i_{cor} = rate of corrosion (A/cm^2)

F = Faraday's constant

t = thickness of diffusion layer

D = diffusion constant (cm^2/sec)

C_o = oxygen concentration in seawater (mol/l)

This limiting current value will become larger if the dissolved oxygen content increases and the electrolyte undergoes velocity changes. Under free corrosion potential, the increased oxygen level accelerates the crack growth significantly.

The Winkler titration method was used to determine the change in the level of the dissolved oxygen in seawater and the following procedure is used [53]:

1) A sample of seawater is collected in a 60-ml glass-stoppered standard bottle.
2) Add the contents of one Dissolved Oxygen I Powder Pillow and one Dissolved Oxygen II Powder Pillow (direct replacement reagents). Carefully replace the stopper so that no air is trapped in the bottle. Invert the bottle several times to ensure proper mixing. A flocculent precipitate will form which will be brownish-orange in color if oxygen is present.
3) Allow the sample to stand until the flocculent precipitate settles and leaves the top half of the solution clear. Again invert the bottle several times for mixing and let the sample stand until the upper half of the solution is clear.

4) Remove the stopper and add the contents of one Dissolved Oxygen III Powder Pillow (direct replacement reagent). Replace the stopper and invert the bottle several times to ensure mixing. The flocculent precipitate will dissolve and leave a yellow colour indicating the presence of oxygen.

5) Pipette 5.8 ml of the prepared solution into the 50 ml flask (about 10 drops).

6) While constantly swirling the flask, titrate the sample with PAO (Phenylarsine oxide) solution for dissolved oxygen until the yellow coloured solution becomes colourless.

7) The number of drops of PAO solution added for Dissolved Oxygen is equal to the mg/l Dissolved Oxygen (each drop is equal to 0.25 mg/l dissolved oxygen).

A.4 Concentration of HCO_3^-

The carbon dioxide exists as bicarbonate and carbonate, and depends on temperature and pH value. The velocity of the surrounding fluid removes the protective material thereby increasing corrosion. The procedure for determination of HCO_3^- concentration in the laboratory is as follows:

1) Prepare a standard dilute solution of HCl (0.01 M).

2) Using BROMOCRESOL GREEN as indicator, titrate a known volume (25 ml) of the seawater sample, against the standard HCl solution.

3) Note the change in the indicator color used from yellow to blue, which gives the end point.

4) Determine the amount of HCO_3^- ion in the sea water sample by volumetric measurements.

APPENDIX-B

B. GENERATION OF PSEUDO-RANDOM LOAD HISTORY [23,54]

For the pseudo-random load application, a block of unimodal variable amplitude random sequence load signal was recorded on a magnetic tape and played repeatedly via a tape loop. The history of the random load signal is as follows: The "random" sea surface $\eta_o(t)$ with a specified power spectrum and a Gaussian probability distribution is generated by convolving a time series of Gaussian "white noise", $\varepsilon(t)$, with an appropriate filter function, $h(\tau)$ and given by

$$\eta_o(t) = \int_{-\infty}^{\infty} h_o(\tau)\ \varepsilon(t-\tau)d\tau \qquad \text{(B-1)}$$

The filter function, $h(\tau)$, is computed from the specified power spectrum of the sea surface on the assumption of zero phase shift in the filter. The wave power spectrum $\phi_{\eta\eta}(\omega)$, is related to the "white noise" power spectrum $\phi_{\varepsilon\varepsilon}(\omega)$ through the frequency function $H_o(\omega)$, which is the Fourier transform of the filter, $h_o(\tau)$ and given by

$$\phi_{\eta\eta}(\omega) = |H_o(\omega)|^2\ \phi_{\varepsilon\varepsilon}(\omega) \qquad \text{(B-2)}$$

The 'band limited white noise' is obtained by generating a series of uncorrelated Gaussian random numbers with zero mean and unit variance. The power spectrum corresponding to a digital time series with uniform time spacing, Δt, is

$$\phi_{\varepsilon\varepsilon}(\omega) = \begin{cases} \frac{1}{\Delta t} & -\frac{\pi}{\Delta t} < \omega < \frac{\pi}{\Delta t} \\ 0 & |\omega| > \frac{\pi}{\Delta t} \end{cases} \qquad \text{(B-3)}$$

The frequency functions (Eqns. B-4 and B-5) corresponding to wave velocities and accelerations at any location (X_i, Z_i), maintain the amplitude and phase relationships consistent with linear wave theory for waves travelling in the positive direction.

$$H_{\bar{u},\,i}(\omega) = H_o(\omega)\,\beta_i \omega e^{k(Z_i - Z_o)}\, e^{-kX_i} \qquad \text{(B-4)}$$

$$H_{\dot{u},\,i}(\omega) = i\omega\, H_{\bar{u},i}(\omega) \qquad \text{(B-5)}$$

The corresponding filter functions (eqns. B-6 and B-7) are obtained from the Fourier transform of the frequency functions.

$$h_{\bar{u},\,i}(\tau) = \frac{1}{2\pi} \int_{-\infty}^{\infty} H_{\bar{u},\,i}(\omega)\, e^{i\omega t}\, d\omega \qquad \text{(B-6)}$$

$$h_{\dot{u},\,i}(\tau) = \frac{1}{2\pi} \int_{-\infty}^{\infty} H_{\dot{u},\,i}(\omega)\, e^{i\omega\tau}\, d\omega \qquad \text{(B-7)}$$

The time series of the wave heights are then obtained based on the velocities and accelerations determined from the convolutions of filter functions with the "white noise" time series.

The pseudo-random load proposed in the present investigation is based on the modelling of the Pierson-Moskowitz spectrum (1:100) for a wind speed of 15 m/s. The drive signal for this particular spectrum was provided by an analog tape prepared at the Rivers and Harbours Laboratory, Norwegian Institute of Technology, Trondheim, Norway. This tape was generated by bandpass filtering of white noise.

A special loop attachment device was used in a LYREC tape recorder, Fig. B1, and played continuously. The single block of the random sequence load pattern with 58 cycles is shown in Fig. B2. The power spectral density of the load signal is shown in Fig. B3.

The random signal was filtered with a cut-off frequency of 20 Hz and fed to the controller unit of the MTS machine. The controller unit consists of an electro-hydraulic testing system, with servo-control, fail safe, and readout functions. The hydraulic actuator applies the mechanical input to the specimen and to a transducer. The transducer conditioner, supplies AC excitation to its associated transducer and provides a DC output proportional to the mechanical input. A digital indicator continuously displays the voltage input representing the load levels.

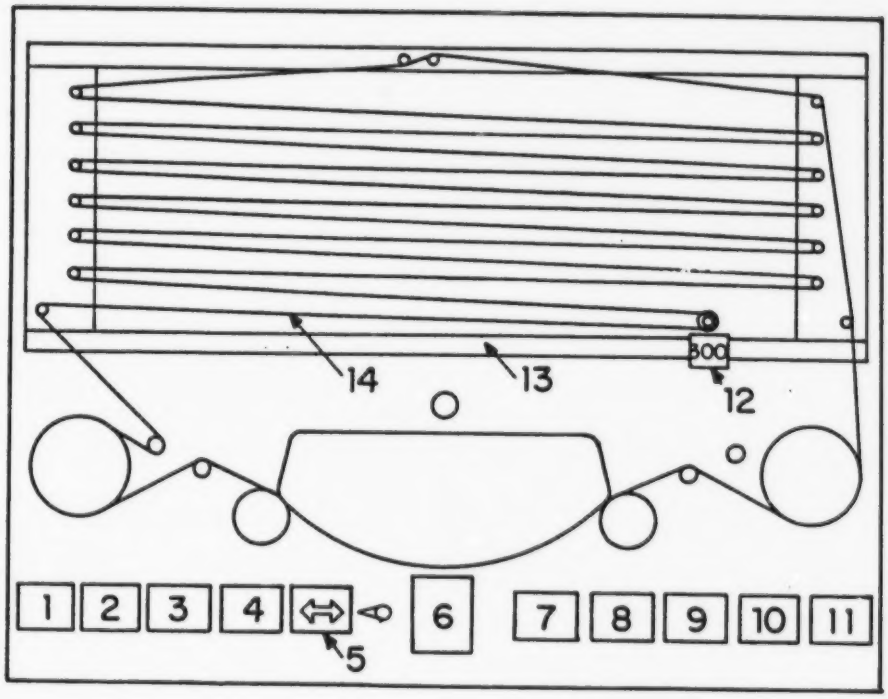

1. ERASE
2. RECORD
3. STOP
4. START
5. ⇔ WINDING CONTROL
6. ADJUSTER
7. 0.6 IPS (INCH PER SECOND)
8. 6 IPS
9. 60 IPS
10. LOOP
11. MAINS
12. LOOP IDLER
13. LOOP ATTACHMENT
14. $\frac{1}{2}$" 1 MIL INSTRUMENTATION TAPE

FIG. B-1 LYREC TAPE RECORDER

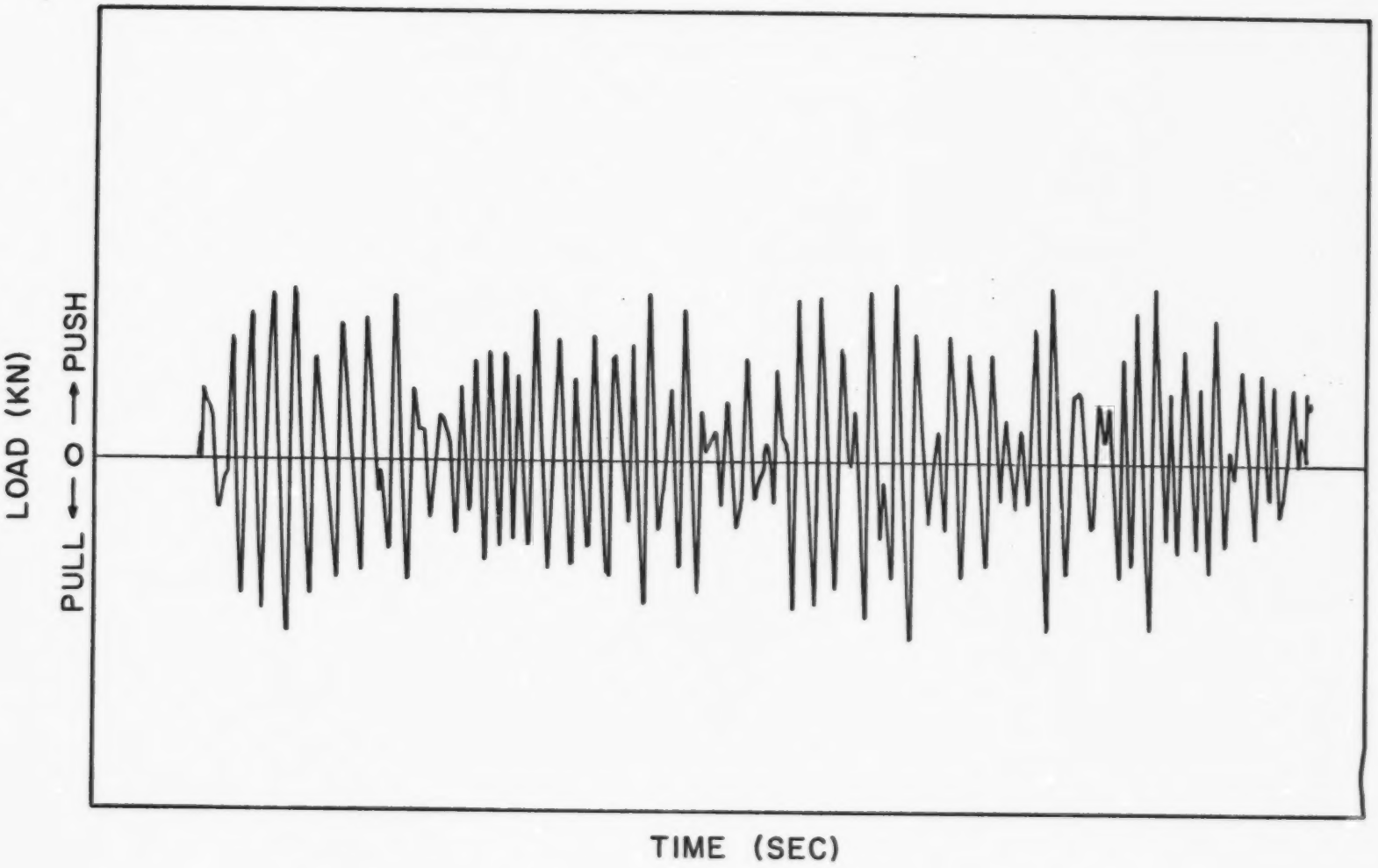

FIG. B-2 PSEUDO-RANDOM INPUT LOAD-TIME HISTORY (CORR.2)

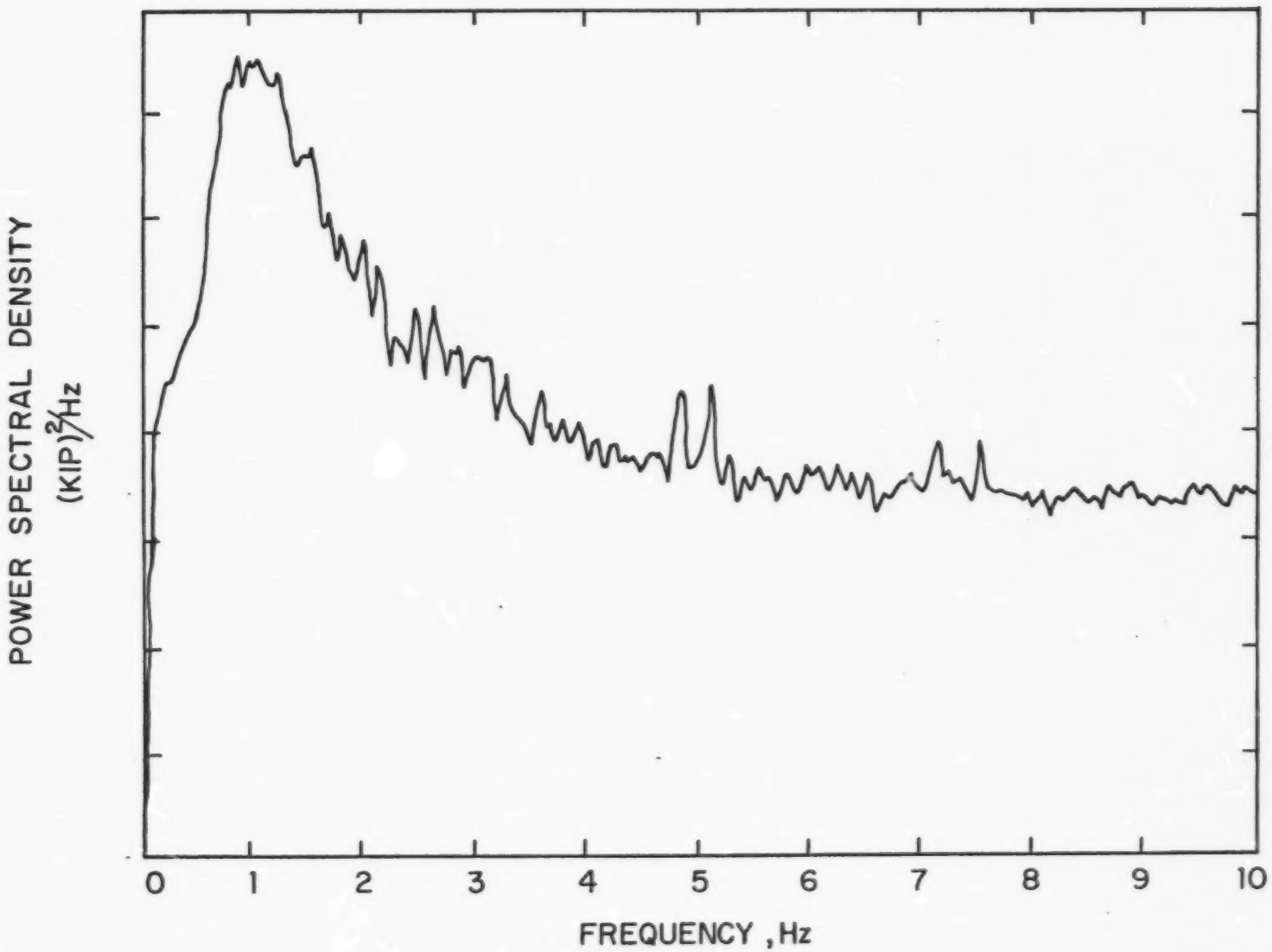

FIG. B-3 POWER SPECTRAL DENSITY OF PSEUDO-RANDOM LOAD SIGNAL

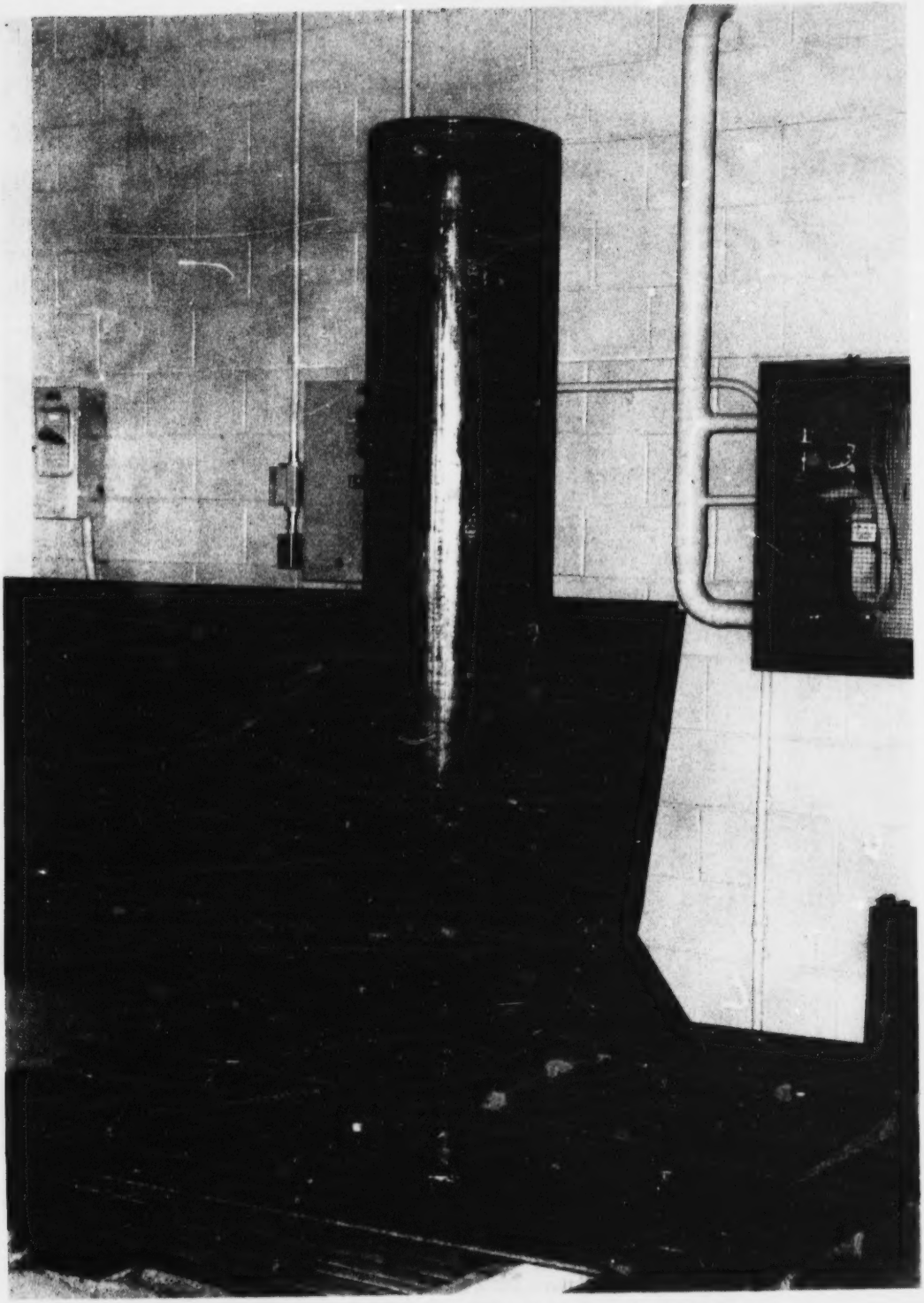

MONOPOD TUBULAR JOINT